

**GAS PRODUCTION FROM HYDRATE-BEARING SEDIMENTS:
GEO-MECHANICAL IMPLICATIONS**

A thesis

Presented to

The Academic Faculty

by

Jong Won Jung

In Partial Fulfillment

of the Requirements for the Degree

Doctor of Philosophy in the School of Civil and Environmental Engineering

Georgia Institute of Technology

December 2010

Copyright © by Jong Won Jung

**GAS PRODUCTION FROM HYDRATE-BEARING SEDIMENTS:
GEO-MECHANICAL IMPLICATIONS**

Approved by:

Dr. J. Carlos Santamarina, Advisor
School of Civil and Environmental
Engineering
Georgia Institute of Technology

Dr. Susan E. Burns
School of Civil and Environmental
Engineering
Georgia Institute of Technology

Dr. Haiying Huang
School of Civil and Environmental
Engineering
Georgia Institute of Technology

Dr. Costas Tsouris
School of Civil and Environmental
Engineering
Georgia Institute of Technology

Dr. Guillermo Goldsztein
School of Mathematics
Georgia Institute of Technology

Dr. Carolyn Ruppel
United States Geological Survey

Date Approved: October 29, 2010

To my families

ACKNOWLEDGEMENTS

First, I thank to God for His speechlessly great love that He has given to me.

I would like to thank my advisor, Dr. J. Carlos Santamarina for his guidance, support, and generosity not only as an advisor, but also as a sincere friend. It was a great pleasure to work with him at Georgia Tech. I am deeply impressed by his deep knowledge, brilliant ideas, and philosophy while I was working with him. I would also like to thank Cecilia for her generous support.

I wish to acknowledge my thesis committee for their useful comments and suggestions: Dr. Carolyn Ruppel, Dr. Susan Burns, Dr. Haiying Huang, Dr. Costas Tsouris and Dr. Guillermo Goldsztein. I also appreciate Dr. In-Mo Lee for all the opportunities during my Master degree.

I also want to thank my parents, sister and parents-in-law for their confidence in me and dedicated support. Above all, I want to thank my dear wife - Younga and son Minjoon for all their love, sacrifice and patience.

Finally, I would like to thank the past and current members of the Particulate Media Laboratory for their help and encouragement: Hyunki Kim, Tae-Sup Yun, Joo-Yong Lee, Veronica R. Landa, Hosung Shin, Douglas D. Cortes, Jaewon Jang, Changho Lee, D. Nicolas Espinoza, Eunseok Bang, Seunghee Kim, Minsu Cha, Sheng Dai, César Pastén, Songhun Chong, Harshad Phadnis, and Rafael Monroy. I also would like to thank Jongwon Choi, Jonghee Kim, Duhwan Kim, Sihyun Kim, Taeseo Ku, Seokho Jeong, Junbong Jang, Hyunwook Choo and the Korean Civil Engineering Society for their support.

TABLE OF CONTENTS

DEDICATION.....	iii
ACKNOWLEDGMENTS.....	iv
LIST OF TABLES.....	ix
LIST OF FIGURES.....	xv
SUMMARY.....	xvi
CHAPTER I INTRODUCTION.....	1
1.1 INTRODUCTION.....	1
1.2 THESIS ORGANIZATION.....	2
CHAPTER II HYDRATE FORMATION AND GROWTH IN PORES.....	4
2.1 INTRODUCTION.....	4
2.2 PRELIMINARY CONCEPTS.....	5
2.3 EXPERIMENTAL STUDY.....	7
2.4 EXPERIMENTAL RESULTS.....	10
2.5 ANALYSES AND DISCUSSION.....	12
2.5.1 Initial hydrate mass.....	12
2.5.2 Hydrate growth on different substances.....	12
2.5.3 Hydrate dissolution – Transients.....	14
2.5.4 Relative stiffness and electrical resistivity.....	14
2.5.5 Ion exclusion – Salt precipitation – Salt limited hydrate growth.....	16
2.6 CONCLUSIONS.....	16

CHAPTER III HYDRATE ADHESIVE AND TENSILE STRENGTHS.....	28
3.1 INTRODUCTION.....	28
3.2 PREVIOUS STUDIES.....	29
3.3 EXPERIMENTAL STUDY.....	31
3.3.1 Equipment and Materials.....	31
3.3.2 Test Procedure.....	32
3.4 EXPERIMENTAL RESULTS.....	33
3.5 ANALYSES AND DISCUSSION.....	34
3.6 CONCLUSIONS.....	35
CHAPTER IV STRESS-STRAIN RESPONSE OF HYDRATE-BEARING SEDIMENTS: NUMERICAL STUDY USING DEM SIMULATION.....	45
4.1 INTRODUCTION.....	45
4.2 NUMERICAL SIMULATION.....	46
4.2.1 Specimen preparation.....	46
4.2.2 Triaxial Compression Test Simulation.....	48
4.3 NUMERICAL RESULTS.....	48
4.3.1 Hydrate-free sediments.....	48
4.3.2 Distributed hydrate-bearing sediments.....	49
4.3.3 Patchy hydrate saturation.....	50
4.4 ANALYSES AND DISCUSSION.....	50
4.5 CONCLUSIONS.....	54

CHAPTER V EMERGENT PHENOMENA IN GAS PRODUCTION FROM HYDRATE-BEARING SEDIMENTS.....	69
5.1 INTRODUCTION.....	69
5.2 EXPERIMENTAL STUDY.....	70
5.2.1 Devices.....	70
5.2.2 Test Procedures.....	72
5.3 EXPERIMENTAL RESULTS.....	73
5.4 ANALYSES AND DISCUSSION.....	75
5.4.1 Hydrate Dissolution.....	75
5.4.2 Fines migration	76
5.4.3 Vuggy structure formation – Gas driven fractures.....	77
5.4.4 Shear wave velocity.	78
5.5 CONCLUSIONS.....	79
CHAPTER VI CH ₄ -CO ₂ REPLACEMENT IN HYDRATE-BEARING SEDIMENTS: A PORE-SCALE STUDY.....	89
6.1 INTRODUCTION.....	89
6.2 EXPERIMENTAL STUDY.....	90
6.2.1 Devices.....	90
6.2.2 Experimental procedures.....	91
6.3 EXPERIMENTAL RESULTS.....	93
6.4 ANALYSES AND DISCUSSION.....	95
6.5 CONCLUSIONS.....	98

CHAPTER VII PROPERTIES AND PHENOMENA RELEVANT TO CH ₄ -CO ₂ REPLACEMENT IN HYDRATE-BEARING SEDIMENTS.....	104
7.1 INTRODUCTION.....	104
7.2 PHYSICAL AND THERMODYNAMIC PROPERTIES.....	105
7.3 PREVIOUS STUDIES – RATES OF REACTION.....	112
7.4 NEW PORE SCALE EXPERIMENTAL STUDY.....	113
7.5 ANALYSES – SEDIMENT SCALE IMPLICATION.....	117
7.5.1 Molecular scale CH ₄ -CO ₂ replacement process.....	117
7.5.2 Bound for excess heat-assisted reaction within the CH ₄ stability field.....	118
7.5.3 Hydrate dissolution in liquid CO ₂	120
7.5.4 Methane gas bubble formation.....	121
7.5.5 Fluid volume expansion during CH ₄ -CO ₂ replacement.....	121
7.5.6 Sediment volume change during CH ₄ -CO ₂ replacement.....	124
7.5.7 Mixed fluid flow.	124
7.5.8 Anticipated sediment-scale emergent phenomena.....	125
7.6 CONCLUSIONS.....	127
CHAPTER VIII CONCLUSIONS.....	143
REFERENCES.....	149

LIST OF TABLES

Table 3.1	Ice and hydrate strengths – Compilation of published results.....	37
Table 3.2	Hydrate thickness.....	38
Table 4.1	Material properties.....	57
Table 5.1	Summary of test condition and procedure.....	81
Table 7.1	Physical properties of CH ₄ and CO ₂ hydrate, pure CO ₂ and water relevant to CH ₄ replacement by CO ₂ in hydrate bearing sediments.	129
Table 7.2	Phase boundaries for pure CH ₄ and CO ₂ hydrates, and liquid-vapor boundary for pure CO ₂ , calculated by fitting values predicted using the experimentally validated formulation in Duan and Sun (2003; 2005).....	131
Table 7.3	Mutual solubilities in binary mixtures. (a) Liquid medium. (b) Gaseous medium.....	132
Table 7.4	Mutual diffusivities in binary water-CO ₂ and water-CH ₄ systems...	133
Table 7.5	Previous CH ₄ -CO ₂ replacement studies. Note: cases are plotted in Fig. 7.2 using the same Test # listed here.....	134
Table 7.6	Anticipated sediment scale phenomena during CH ₄ -CO ₂ gas replacement.....	135

LIST OF FIGURES

Figure 2.1	Experimental device. Hydrate formation and growth (a) in a capillary tube, (b) between hydrophilic (glass) or hydrophobic (acrylic) plates, and (c) between two copper balls.....	18
Figure 2.2	Hydrate formation and growth in capillary tubes: The first image corresponds to the first observation of hydrate formation after a long induction time of ~14 days. The time for subsequent images is referred to the first one.....	19
Figure 2.3	Rate of hydrate formation in capillary tubes – Data are shown for two typical experiments.....	20
Figure 2.4	Hydrate formation and growth - meniscus between two surfaces. The first image in each sequence corresponds to the first observation of hydrate formation and it is assigned time $t=0$ min. The time for subsequent images is referred to the first one. (a) Hydrophilic, water-wet glass substrates. (b) Hydrophobic, oil-wet acrylic substrates.....	21
Figure 2.5	Rate of hydrate formation between plates. (a) Hydrophilic water-wet plates. (b) Hydrophobic oil-wet plates. Data for CO_2 and CH_4 hydrates.....	22
Figure 2.6	CH_4 hydrate formation in a salty solution (0.26mol/L) at the meniscus between two particles. (a) Pressure. (b) Temperature. (c) Measured voltage to be used for calculating electrical resistance. (d) Vibration detected by the receiving piezocrystal used for relative stiffness estimation.....	23
Figure 2.7	Meniscus electrical resistance and relative stiffness before and after hydrate formation for solutions with different initial ionic concentration. (a) CO_2 hydrate and (b) CH_4 hydrate. Note: Relative stiffness is defined in terms of the output voltage produced by the sensing piezocrystal.....	24
Figure 2.8	Initial, fast hydrate formation by the consumption of excess gas ($C_{bh}-C_{ah}$). (a) Before hydrate formation. (b) After hydrate formation. Note: CO_2 gas solubility in water with hydrate: $C_{ah}=0.06\text{mol/kg}$ at 3MPa, 273K. CO_2 gas solubility in water without hydrate: $C_{bh}=0.11\text{mol/kg}$ at 3MPa, 273K.....	25

Figure 2.9	Changes in gas concentration within a capillary tube: (a) before hydrate formation, (b) after gas diffusive transport, and (c) after a sudden hydrate formation. CO ₂ gas solubility in water with hydrate: $C_{ah}=0.06\text{mol/kg}$ at 3MPa, 273K. CO ₂ gas solubility in water without hydrate: $C_{bh}=0.11\text{mol/kg}$ at 3MPa, 273K.....	26
Figure 2.10	Change in salt concentration by ion exclusion as a function of hydrate thickness. Lines show the increase in salt concentration in the remaining free water during hydrate growth. The dotted line shows the salt concentration saturation at 275°K. Points represent final hydrate thickness and molar concentration estimated for the experiments reported in Fig. 2.7.....	27
Figure 3.1	Device built to measure tensile strength. The load cell consists of a cantilever beam instrumented with strain gauges. The device is placed inside P-T controlled pressure chamber.....	39
Figure 3.2	Experimental results: (a) water meniscus between mica substrates, (b) CH ₄ hydrate formation, (c) adhesive failure between CH ₄ hydrate and mica substrate, (d) water meniscus between calcite substrates, (e) CH ₄ hydrate formation, (f) tensile failure between CH ₄ hydrate and calcite substrate.....	40
Figure 3.3	Typical force-time response (Case: CH ₄ hydrate on a calcite substrate)	41
Figure 3.4	Hydrate adhesive and tensile strengths. Assumed cross section: filled symbols correspond to 100% formation while empty symbols correspond to annular hydrate formation.....	42
Figure 3.5	The reference of tensile/ adhesive hydrate strength on the shear strength of hydrate-bearing sediments. (a) Bonded hydrate mass in a simple cubic packing configuration. (b) Force diagram for a single particle.....	43
Figure 3.6	Internal pressure change during tensile loading. (a) Boundary conditions for FEM simulation. (b) Numerical results (Case: displacement=0.08%, E=8.2 GPa, $\nu=0.32$, P=8.0 MPa). (c) Internal pressure change during pull out as a function of the imposed strain.....	44
Figure 4.1	Simulation of hydrate bearing sediments. (a) Hydrate-free sediments. (b) Distributed hydrate. (c) Patchy hydrate saturation: C1 shows a 2D schematic; C2 shows grain clusters in 3D. Clusters have 100% hydrate saturation while the sediment matrix has no hydrate (transparent in Figure c2).....	58

Figure 4.2	Distributed hydrate bearing sediment with hydrate saturation S_{hyd} – Stress, strain, and volume change. (a) Stress-strain response. (b) Volume change. Note: Confining stress= 1MPa.....	59
Figure 4.3	Distributed hydrate-bearing sediments- Different hydrate saturation S_{hyd} Critical state line projected on (a) q-p' plane, and (b) e-p' plane.....	60
Figure 4.4	Sediment with patchy hydrate saturation (15 clusters). (a) Stress-strain response. (b) Volume change. Note: Confining stress= 1MPa.....	61
Figure 4.5	Sediment with patchy hydrate saturation (15 clusters): Different hydrate saturation S_{hyd} . Critical state line projected on (a) q-p' plane, and (b) e-p' plane.....	62
Figure 4.6	Sediment with patchy hydrate saturation- stress, strain, and volume change. The effect of cluster size or number of clusters at the same hydrate saturation $S_h=20\%$. (a) Stress-strain response. (b) Volume change. Note: Confining stress= 1MPa, Initial void porosity=0.393.....	63
Figure 4.7	Strength comparison between distributed hydrate-bearing sediments and patchy hydrate. The data include results for 2 values of porosity ($n=0.361$ and 0.393), 3 hydrate saturations ($S_{hyd}= 5\%$, 20% , 50%), and 3 confining stress ($\sigma'_d=0.1MPa$, $0.5MPa$, $1MPa$)	64
Figure 4.8	Normal contact force chains between soil particles (2D simulations). Images are shown (a) after consolidation to 1MPa of hydrate-free sediments, and after an additional 1.2MPa deviatoric stress is applied to (b) hydrate-free sediments, (c) distributed hydrate-bearing sediments, (d) sediments with patchy hydrate saturation.....	65
Figure 4.9	Strength of hydrate-bearing sediments - Experimental data and DEM results.....	66
Figure 4.10	Mid-strain stiffness of hydrate-bearing sediments (distributed hydrate) as a function of hydrate saturation and effective stress.....	67
Figure 4.11	Hydrate dissociation under different reservoir boundary conditions: (a) constant stress boundary CS , (b) zero strain boundary ZS , or (c) constant vertical stress but zero lateral strain K_o condition.....	68

Figure 5.1	Devices and instrumentation. (a) Seafloor Process Simulator. (b) Internal instrumented soil cell; LVDT for sediment displacement measurements, bender element BM for S-wave velocity measurements, thermocouples TC for temperature measurements, and pressure transducers for pressure measurements. (c) Complete system including peripheral electronics.....	82
Figure 5.2	Pressure and temperature histories during hydrate formation. (a) Spontaneous hydrate formation in a gas-filled sand-clay mixture with initial water saturation $S_w = 50\%$ (Test #3). (b) Hydrate formation in initially dry gas-filled sand triggered by water injection (Test #2). (c) Hydrate formation and dissolution during deaired-water injection in gas-filled sand that had some initial hydrate saturation (Test #2). (d) Hydrate formation in a water saturated sand triggered by water drainage (Test #1). (e) Hydrate dissociation by depressurization (final stage in Test #3).....	83
Figure 5.3	S-wave velocity changes during hydrate formation, dissolution, and dissociation (Test #3)	84
Figure 5.4	Fines migration during hydrate dissociation. (a) Fines migration during upwards flow (Test #3), and (b) Fines migration due to drainage through the bottom plate port (Test #4).....	85
Figure 5.5	Shear wave velocity in hydrate-bearing sediments. Trends shown for sands (Equation 3). Experimental results correspond to Test #3: (1) \diamond No hydrate – before hydrate formation or after hydrate dissociation. (2) Δ After initial hydrate formation. (3) \square drop due to hydrate dissolution after gas-free water injection. (4) \circ Hydrate re-growth after water drainage and gas invasion.....	86
Figure 5.6	Vuggy structure formation due to local clogging and particle displacement during gas bubble expansion. (a) Distributed fines in a water saturated sediment. (b) Gas bubble nucleation during depressurization. Fines move with the gas-water interface as the gas bubble grows. (c) High fines concentration clogs pore throats. (d) Further gas bubble growth can push sand particles away. The resulting vuggs are precursors to gas-driven fracture formation....	87
Figure 5.7	Total stress, effective stress and gas driven fracture. (a) Hydrates are dissociated by depressurization. i.e., decrease in the boundary total stress. (b) Rapid depressurization induces ice formation concurrent with hydrate dissociation. (c) Gas expansion creates hydraulic fracture that facilitates gas evacuation.....	88

Figure 6.1	Experimental devices and components: (a) Pore-scale device, (b) Pressure chamber and external components, (c) Peripheral electronics to measure electrical conductivity and relative stiffness.....	100
Figure 6.2	Complete P-T history during the experiment: (a0) Water, (a1) Ice forms, (a2) Ice melts, (a3) Leaving the CH ₄ hydrate phase boundary, (a4) CH ₄ hydrate nucleation and growth, (b1) CO ₂ injection; (b2) Liquid CO ₂ forms in the chamber, (c0) Beginning of depressurization, (c1) Gas-liquid CO ₂ phase boundary, (c2) CH ₄ hydrate phase boundary, (c3) CO ₂ hydrate phase boundary, and (c4) End of test.....	101
Figure 6.3	Evolutions of pressure, temperature, electrical resistance, and relative stiffness during all experiments at stages (Refer to Figure 6.2 for detailed P-T path): (a0) Water, (a1) Ice forms, (a2) Ice melts, (a3) Leaving the CH ₄ hydrate phase boundary, (a4) CH ₄ hydrate nucleation and growth, (b1) CO ₂ injection; (b2) Liquid CO ₂ forms in the chamber, (c0) Beginning of depressurization, (c1) Gas-liquid CO ₂ phase boundary, (c2) CH ₄ hydrate phase boundary, (c3) CO ₂ hydrate phase boundary, and (c4) End of test. Note: A cubic time scale is used to capture both short and long duration events.....	102
Figure 6.4	Traces of photographs obtained during the replacement: (a) Water droplet, (b) Ice formation, (c) CH ₄ hydrate formation and growth, (d) After the injection of liquid CO ₂ , (e) Depressurization out of the CH ₄ hydrate stability field, and (f) Image after hydrate dissociation.....	103
Figure 7.1	Hydrate forming molecules (N ₂ , CO ₂ and CH ₄) and two faces of the big cage in sI hydrate. All molecules are drawn using van der Waals radii to the same scale. Hexagonal and pentagonal faces are not regular polygons. Notice that the opening between water molecules is smaller than the size of N ₂ , CO ₂ and CH ₄ molecules..	136
Figure 7.2	Dissociation phase boundaries for CO ₂ and CH ₄ hydrates, liquid-vapor phase boundary for pure CO ₂ , and liquid water-ice boundary. Data points show fluid pressure and temperature conditions for CH ₄ -CO ₂ replacement studies reported in the literature (numbers correspond to references listed in Table 7.5). Notice that CO ₂ and CH ₄ hydrate phase boundaries cross at ~7.5MPa and 283.7K. Furthermore, the CO ₂ liquid-vapor boundary intersects the two dissociation lines creating four different zones inside the CO ₂ hydrate stability field, above the	

	liquid water-ice boundary.....	137
Figure 7.3	Experimental studies. (a) Pressure cell and devices. (b) Droplet experiments: i- CH ₄ pressurization, ii- cooling, iii- CH ₄ hydrate formation, iv- liquid CO ₂ injection, v- CH ₄ -CO ₂ hydrate dissociation. (c) Meniscus experiments: i- CH ₄ pressurization, ii- cooling, iii- ice formation, iv- ice melting, v- CH ₄ hydrate formation, vi- injection of liquid CO ₂ , vii- liquid CO ₂ to gas, viii- exit CH ₄ hydrate stability field, and ix- exit CO ₂ hydrate stability field. Both experiments are conducted using de-ionized water and research purity gases.....	138
Figure 7.4	Droplet experiment: time evolution of the CH ₄ hydrate shell after flooding with liquid CO ₂ . Pressure is 6MPa and the chamber temperature stays at 274±1K, after point (iv) in Fig. 7.3-b. This sequence of images suggests that liquid CO ₂ “dries” the water either in the hydrate shell and/or inside the hydrate droplet.....	139
Figure 7.5	Meniscus experiment. (a) Water droplet – Scale: 8.7mm diameter, (b) Ice formation, (c)-(e) CH ₄ hydrate formation and growth, (f) Injection of liquid CO ₂ , (g) Depressurization from liquid CO ₂ to gas CO ₂ , (h) Image for P-T conditions outside the CH ₄ hydrate stability field.....	140
Figure 7.6	Pressure-temperature upper and lower bounds for initiating excess heat CH ₄ -CO ₂ hydrate replacement by raising the local temperature to the CH ₄ hydrate dissociation boundary. The temperature increases due to the heat released after CH ₄ hydrate dissociation and CO ₂ hydrate formation. Upper bound: the reaction can begin far inside the CH ₄ hydrate stability zone for a solid hydrate mass (upper bound ~10K from the CH ₄ hydrate dissociation boundary). Lower bound: the reaction must begin closer to the CH ₄ hydrate phase boundary in hydrate bearing sediments where minerals and water absorb liberated heat. Bounds are computed using Equation 7.3 and parameters from Table 7.1, porosity $\phi=0.5, 0.25, 0.10$; $c_m=0.83$ kJ/(kg·K); $H^f_{CO_2hyd}=395$ kJ/kg; $H^d_{CH_4hyd}=440$ kJ/kg, $\rho_{CO_2hyd}=1100$ kg/m ³ , and $\rho_{CH_4hyd}=930$ kg/m ³ . Note: this analysis does not consider intermediate hydrate phase boundaries for hydrate grown from gas mixtures (Section 2e-1)	141
Figure 7.7	Volume change analysis. (a) During hydrate formation/dissociation, i.e. Eq. 7.7 (b) During CH ₄ -CO ₂ replacement, i.e. Eq. 7.8 (P=7.4MPa, T=281.4K, $\rho_{CO_2}=906$ kg/m ³ , bubble point for CH ₄ /CO ₂ mixture $R_{BP}=12\%$ mol CH ₄ / mol CO ₂).....	142

SUMMARY

Gas hydrate consists of guest gas molecules encaged in water molecules. Methane is the most common guest molecule in natural hydrates. Methane hydrate forms under high fluid pressure and low temperature and is found in marine sediments or in permafrost region. Methane hydrate can be an energy resource (world reserves are estimated in 20,000 trillion m^3 of CH_4), contribute to global warming, or cause seafloor instability. Research documented in this thesis starts with an investigation of hydrate formation and growth in the pores, and the assessment of formation rate, tensile/adhesive strength and their impact on sediment-scale properties, including volume change during hydrate formation and dissociation. Then, emphasis is placed on identifying the advantages and limitations of different gas production strategies with emphasis on a detailed study of CH_4 - CO_2 exchange as a unique alternative to recover CH_4 gas while sequestering CO_2 . The research methodology combines experimental studies, particle-scale numerical simulations, and macro-scale analyses of coupled processes.

CHAPTER I

INTRODUCTION

1.1 INTRODUCTION

Gas hydrate is a naturally occurring crystalline compound formed by water molecules and encapsulated gas molecules. Gas hydrate was first reported by H. Davy in 1811. Later, E. G. Hammerschmidt found hydrate blocking the pathways inside of oil and gas pipelines in 1934. This discovery stimulated research related to chemical additives that inhibit hydrate formation in pipes. Y. F. Makogon found natural gas hydrates in the Siberian permafrost region in 1965, and C. Bily and J.W.L. Dick reported the presence of hydrates in a core extracted from the MacKenzie Delta. Since then, the existence of gas hydrate has been identified worldwide through geophysical and deep sea drilling methods.

Methane hydrate reserves are on the order of 500-to-10,000 Gt of carbon worldwide (Collett 2002; Kvenvolden 1988; Milkov 2004; Ruppel and Pohlman 2008). These vast reserves suggest the potential of gas hydrate as an energy source. In addition, the proper understanding of hydrate formation/dissociation is important to analyze seafloor stability; for example, further sedimentation after hydrate formation does not consolidate the hydrate-bearing sediments, and the dissociation of hydrates within these less consolidated sediments would cause massive seafloor failure (Cochonat et al. 2002;

Kayen and Lee 1991; Maslin et al. 2004; Sloan 2003; Sultan et al. 2004a; Sultan et al. 2004b). Finally, significant long term global warming effects would be expected if methane were released into the atmosphere by methane hydrate dissociation (Hornbach et al. 2004; Kvenvolden 1999; Maslin et al. 2004). Therefore, a proper understanding of hydrate formation and dissociation in sediments is necessary to develop production methods, as well as to prevent unexpected seafloor failure and gas release (Sloan and Koh 2008).

1.2 THESIS ORGANIZATION

The central themes of this research are hydrate formation and growth in pores, tensile/adhesive strength, and its impact on sediment-scale properties, emergent phenomena during gas production, and CH₄-CO₂ exchange as a unique alternative to recover CH₄ gas while sequestering CO₂. The manuscript is organized as follows.

Chapter 2 documents a pore scale study of the interaction between hydrate, water and mineral surfaces during hydrate formation. The purpose of this study is to investigate hydrate formation and growth patterns on water-wet and oil-wet substrates, and to explore the effect of salts when the water volume is limited.

Chapter 3 reports an experimental determination of the adhesive and tensile strengths of CH₄ hydrate, CO₂ hydrate, tetrahydrofuran hydrate, and ice on calcite and mica substrates, and anticipates mechanical implications.

Chapter 4 focuses on the understanding of stress-strain response of hydrate-bearing sediments. The discrete element method is used to upscale the adhesive and tensile strengths of hydrates determined in chapter 3 to determine macroscale sediment properties and to gain insight into underlying particle-level process.

Chapter 5 investigates several emergent phenomena during hydrate dissociation, such as secondary ice formation, fines migration, vuggy structure formation and gas-driven fracture formation using the large-scale Seafloor Process Simulator. This is collaborative work with J. Jang and the research team at Oak Ridge National Laboratory.

Chapters 6 and 7 document a comprehensive study of CH₄-CO₂ replacement, and investigate pore-scale changes in electrical resistance and relative stiffness, replacement reaction rates, the pressure-temperature region for optimal exchange, and potential geo-mechanical implications during CH₄-CO₂ replacement in hydrate-bearing sediments. Chapter 7 was conducted in collaboration with D. N. Espinoza.

Salient conclusions and recommendations for further studies are summarized in chapter 8.

CHAPTER II

HYDRATE FORMATION AND GROWTH IN PORES

2.1. INTRODUCTION

Gas hydrate consists of guest gas molecules encaged in water molecules. In nature, methane gas hydrates are found in sediments under high pore pressure and low temperature. The low solubility of methane in water (e.g. 1CH₄ in ~800H₂O molecules) contrasts with the high concentration of methane in hydrate (1CH₄ every 6H₂O). Several laboratories have been developed to circumvent the long time required for diffusion-limited hydrate formation in sediments, such as flushing methane gas through partially water-saturated sediments (Kneafsey et al. 2005; Waite et al. 2004), advecting gas dissolved in water (Zatsepina and Buffet 2001), mixing ground ice to exploit the pre-existing ice cages (Circone et al. 2004; Ebinuma et al. 2005; Kamath et al. 1991; Masui et al. 2005b; Stern et al. 1998; Ullerich et al. 1987; Waite et al. 2002; Yoon et al. 2004), and premixing ground hydrate with the sediments (Hyodo et al. 2002).

Each of these methods produces different pore-scale hydrate patterns (Collett 2002; Ebinuma et al. 2005; Spangenberg and Kulenkampff 2005; Zhong and Rogers 2000), which eventually affect the macro-scale mechanical properties of hydrate-bearing sediments. For example, even a small amount of hydrate at interparticle contacts causes a dramatic increase in the small strain stiffness of hydrate-bearing sediments as

compound to the same hydrate mass resting within the pore space (Yun et al. 2007) .

The purpose of this study is to investigate hydrate formation and growth patterns on water-wet and oil-wet substrates, and to explore the effect of salts when the water volume is limited.

2.2. PRELIMINARY CONCEPTS

Hydrate nucleation on surfaces. Preferential hydrate nucleation on substrates, i.e., heterogeneous nucleation, can be explained in thermodynamic terms using the concept of Gibbs free energy. The change in Gibbs free energy from water to hydrate ΔG is lower when hydrate forms on substrates ΔG^* than when it forms in the bulk water ΔG . The value of ΔG^* varies according to particle characteristics such as composition, crystallography, and surface charge (Fletcher 1969) . It can be related to the bulk water ΔG through the contact angle between the liquid, gas hydrate, and the mineral (Kashchiev and Firoozabadi 2002),

$$\Delta G^* = \Delta G \cdot \left[\frac{1}{4} (2 + \cos \theta) \cdot (1 - \cos \theta)^2 \right]^{\frac{1}{3}} \quad (2.1)$$

The contact angle relates the interfacial tensions γ [$\text{J} \cdot \text{m}^{-2}$] between mineral and liquid γ_{ml} , mineral and hydrate γ_{mh} , and hydrate and liquid γ_{hl} ,

$$\cos \theta = \frac{\gamma_{ml} - \gamma_{mh}}{\gamma_{hl}} \quad (\text{Young's equation}) \quad (2.2)$$

Molecular dynamic simulations corroborate thermodynamic predictions and provide molecular-scale insight. In particular, these simulations show lower activity near substrates and early water structuring that favors hydrate nucleation (See simulation in Kvamme, et al. 2007 and in Walsh, et al. 2009).

Hydrate growth. Once hydrate nucleates, it grows forming a thin shell along the water-gas interface (Jung et al. 2010; Mochizuki and Mori 2006). Then, it starts to grow into the liquid phase as shown by water droplet tests (Jung et al. 2010; Ohmura et al. 1999; Sugaya and Mori 1996; Taylor et al. 2007b; Uchida et al. 1999; Uchida et al. 2002) and gas-water tests in tubes (Freer et al. 2001; Gayet et al. 2005; Lin et al. 2004; Link et al. 2003; Mochizuki and Mori 2006; Ohmura et al. 2000; Ohmura et al. 2004; Subramanian and Sloan 2002; Sugaya and Mori 1996; Tabe et al. 2000; Taylor et al. 2007b; Uchida et al. 1999). Hydrate may also grow into the gas phase forming a tree-branch geometry as water escapes confined liquid volumes (Zhong et al. 2008).

Hydrate growth rate is gas diffusion controlled. Gas diffusion is low in water ($D=1.37$ -to- $1.49 \times 10^{-9} \text{m}^2/\text{s}$ - Thomas and Adams, 1965; Witherspoon, 1969) and even lower through the CH_4 hydrate mass ($D=3.4 \times 10^{-13} \text{m}^2/\text{s}$ - Davies, et al., 2008).

Gas Solubility and Ostwald Ripening. Hydrate dissolution occurs inside the hydrate stability field when the water that surrounds the hydrate mass is not gas-saturated (Rehder et al. 2004; Zhang and Xu 2003). The solubility in bulk water at 6.6MPa and 274°K is 1.66mol/kg for CO₂ and 0.12mol/kg for CH₄. However, gas solubility decreases when hydrate is present (Waite et al. 2009); for example, it falls to 0.83mol/kg for CO₂, and to 0.063mol/L for CH₄ at 6.6MPa and 274°K (Jung et al. 2010).

Gas concentration increases near small hydrate nuclei. Therefore, a concentration gradient develops between the water that surrounds a small crystal and a nearby large one. Eventually, diffusion transport leads to the growth of large crystals at the expense of small ones. This process is known as Ostwald Ripening (Klapp et al. 2010; Klapp et al. 2007).

Ion Exclusion. Finally, we note that the formation of contiguous hydrate cages during slow hydrate formation displaces nearby hydrated ions which must diffuse back into the liquid water (Duan and Sun 2006; Masoudi et al. 2005; Mohammadi and Tohidi 2005; Østergaard et al. 2005).

2.3. EXPERIMENTAL STUDY

Three sets of experiments are conducted to study hydrate formation near substrates. Experimental devices, materials, and procedure are described next. All experiments are monitored using time-lapse photography (resolution: 1pixel~10µm), pressure

transducers and thermocouples. Figure 2.1 shows schematic diagrams and dimensions of the specific devices used in each set of experiments. All tests were conducted inside P-T controlled pressure chambers.

Hydrate in capillary tubes (Fig. 2.1-a). In this study, the capillary tube is its own pressure chamber (polyphenylsulfone; rated for 106MPa; outside diameter 3.15mm; inside diameter 1.57mm). The contact angle between distilled water and the capillary tube is $\sim 90^\circ$. First, we fill the tube with de-aired water until the water-air interface is centered in the field of view; then, the tube is placed in a cooler at $\sim 275^\circ\text{K}$, and is pressurized to $\sim 3.4\text{MPa}$ with CO_2 gas.

Hydrate formation between water-wet or oil-wet surfaces (Fig. 2.1-b). Transparent glass and acrylic plates are used to simulate water-wet and oil-wet surfaces. A water droplet is placed between two glasses or two acrylic plates creating a quasi-cylindrical body of water (e.g. 8.7mm diameter, 1.97mm in height, and 120mg water mass). Water droplets with various salinities between 0M and 1.28M (NaCl - sodium chloride) are tested. This parallel-plate device is placed inside a stainless steel pressure chamber (thickness $\sim 43\text{mm}$; design pressure $\sim 30\text{MPa}$) that has a large size sapphire window for visual observation (70mm diameter) and multiple feed through parts for instrumentation. The chamber is maintained at $\sim 275^\circ\text{K}$ and it is pressurized to $\sim 8\text{MPa}$ for CH_4 hydrate formation studies and to $\sim 3.4\text{MPa}$ for CO_2 hydrate formation studies. Nucleation is triggered by causing transient ice formation at low temperature ($258\text{-to-}263^\circ\text{K}$); thereafter, a constant temperature ($\sim 275^\circ\text{K}$) and pressure ($\sim 3.4\text{MPa}$ or $\sim 8\text{MPa}$)

conditions are maintained during the test.

Hydrate formation in a water meniscus between neighboring particles (Fig 2.1-c). In this third set of tests, a droplet of salt water (NaCl; 0M and 1.28M) is placed between two copper spheres, creating a geometric configuration similar to that of a naturally occurring water meniscus between two grains (copper sphere: 5.2mm diameter. water droplet: 3.4-to-4.1mm diameter, 1.3-to-1.89mm in height, and 12-to-25mg mass). The copper spheres are glued onto cylindrical piezocrystals. This configuration allows us to measure electrical resistance and relative stiffness during hydrate formation. Fig. 2.1-c shows the electrical circuit and peripheral electronics used. Electrical resistance is determined at 50 kHz to avoid electrode polarization effects. The resistance of the meniscus R is a function of the measured voltages V_1 and V_2 , and the known resistance of the series resistor $R^*=4700\Omega$,

$$R = \frac{V_2}{V_1 - V_2} R^* \quad (2.3)$$

The source piezocrystal is connected to a sinusoidal signal generator operated at ~60 kHz. The signal amplitude produced by the output piezocrystal is measured using an oscilloscope. The device is placed inside a pressure chamber and is subjected to P-T conditions similar to the preview test except that no transient ice formation is used to trigger hydrate nucleation; therefore, these tests experienced long induction times.

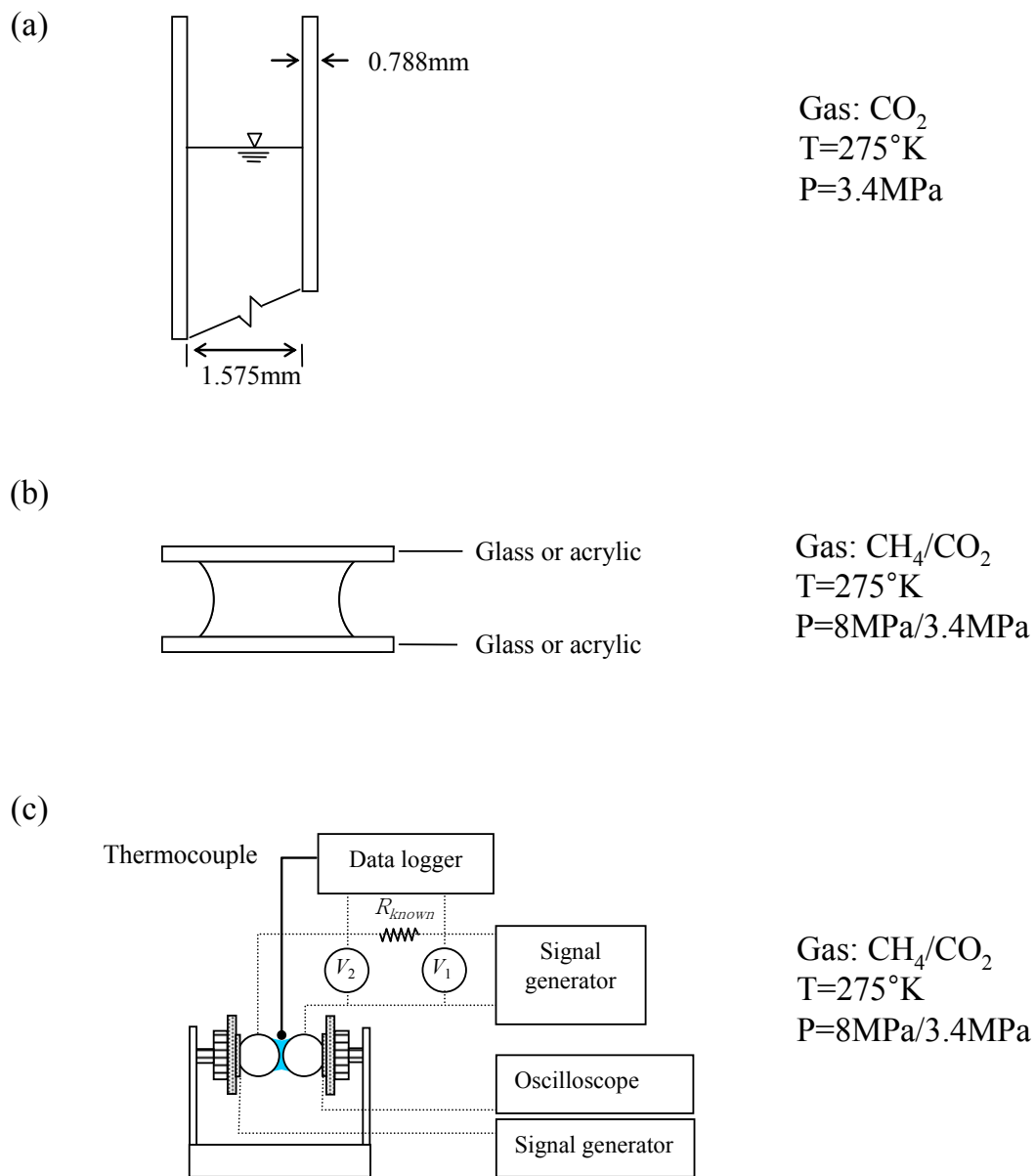


Figure 2.1. Experimental device. Hydrate formation and growth (a) in a capillary tube, (b) between hydrophilic (glass) or hydrophobic (acrylic) plates, and (c) between two copper balls.

2.4. EXPERIMENTAL RESULTS

Hydrate formation in capillary tubes. A collection of images gathered during single test is presented in Figure 2.2. Multiple similar tests allow us to make the following observations. Hydrate nucleates at the interface between the gas and water phases after long induction times (after ~14 days). Growth into the water phase is rather discrete, i.e. in steps (Fig. 2.3). Hydrate also grows into the gas phase in part due to the water volume expansion during water-hydrate transformation ($V_{hyd}/V_w=1.279$). We often see that a fraction of the hydrate mass dissolves after some growth and begins to re-grow. Hydrate dissolution-growth cycles repeat multiple times with an overall growth-trend. The hydrate mass is not cylindrical but lobular, and does not adhere to the plastic capillary tube.

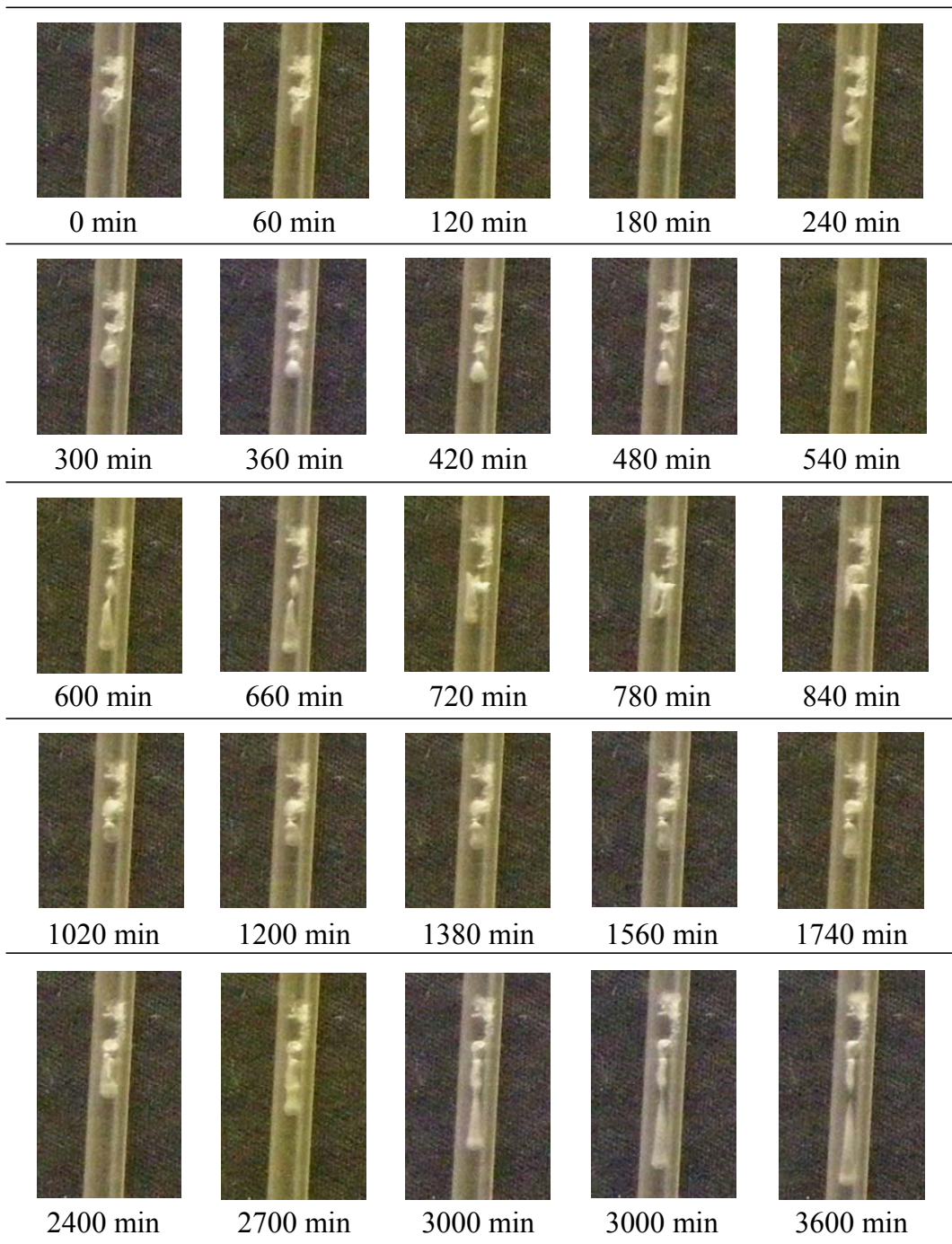


Figure 2.2. Hydrate formation and growth in capillary tubes: The first image corresponds to the first observation of hydrate formation after a long induction time of ~14 days. The time for subsequent images is referred to the first one.

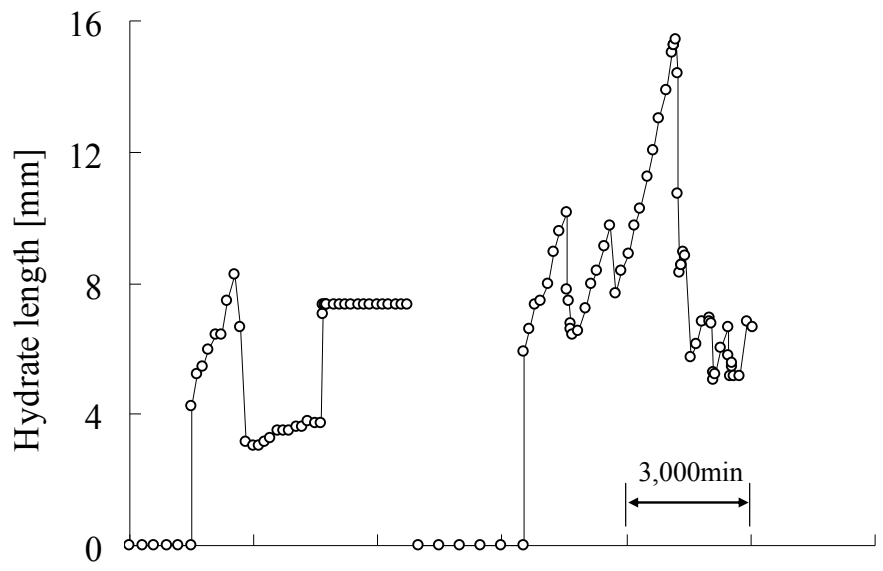


Figure 2.3. Rate of hydrate formation in capillary tubes – Data are shown for two typical experiments.

Hydrate formation between water- and oil-wet substrates. The evolution of hydrate formation in the water droplet between the two parallel plates is documented in Figure 2.4. Nucleation is triggered by causing transient ice formation to prevent long induction times; as the ice melts, hydrate nucleates at the gas-water interface. Hydrate does not grow homogeneously but advances in the form of lobes that invade the water meniscus. Volume expansion during hydrate growth causes water to flow out of the meniscus. The displaced water coats water-wet surfaces and forms a thin hydrate layer on them (Fig. 2.4-a and c). However, water does not flow away from meniscus onto hydrophobic surface. When salt solution is used, water trapped inside the meniscus may not change into hydrate (observation times as long as ~11,000min), and remains as liquid water surrounded by the hydrate shell that separates the gas phase from the liquid water (Fig. 2.4-b and d). In all cases, hydrate appears suddenly (within the time interval of two successive images $\Delta T=10\text{sec}$), but grows slowly as a shown in Fig. 2.5.

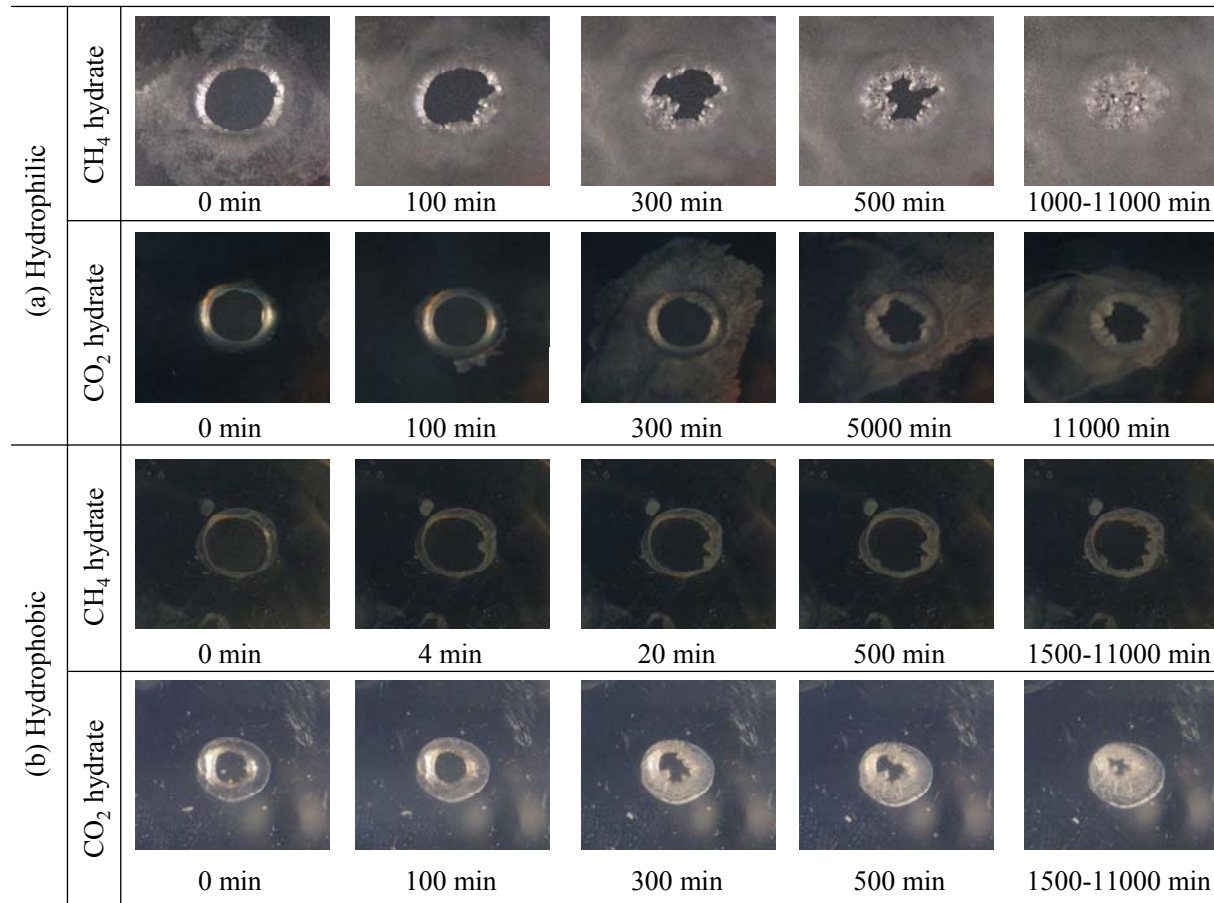


Figure 2.4. Hydrate formation and growth - meniscus between two surfaces. The first image in each sequence corresponds to the first observation of hydrate formation and it is assigned time $t=0$ min. The time for subsequent images is referred to the first one. (a) Hydrophilic, water-wet glass substrates. (b) Hydrophobic, oil-wet acrylic substrates.

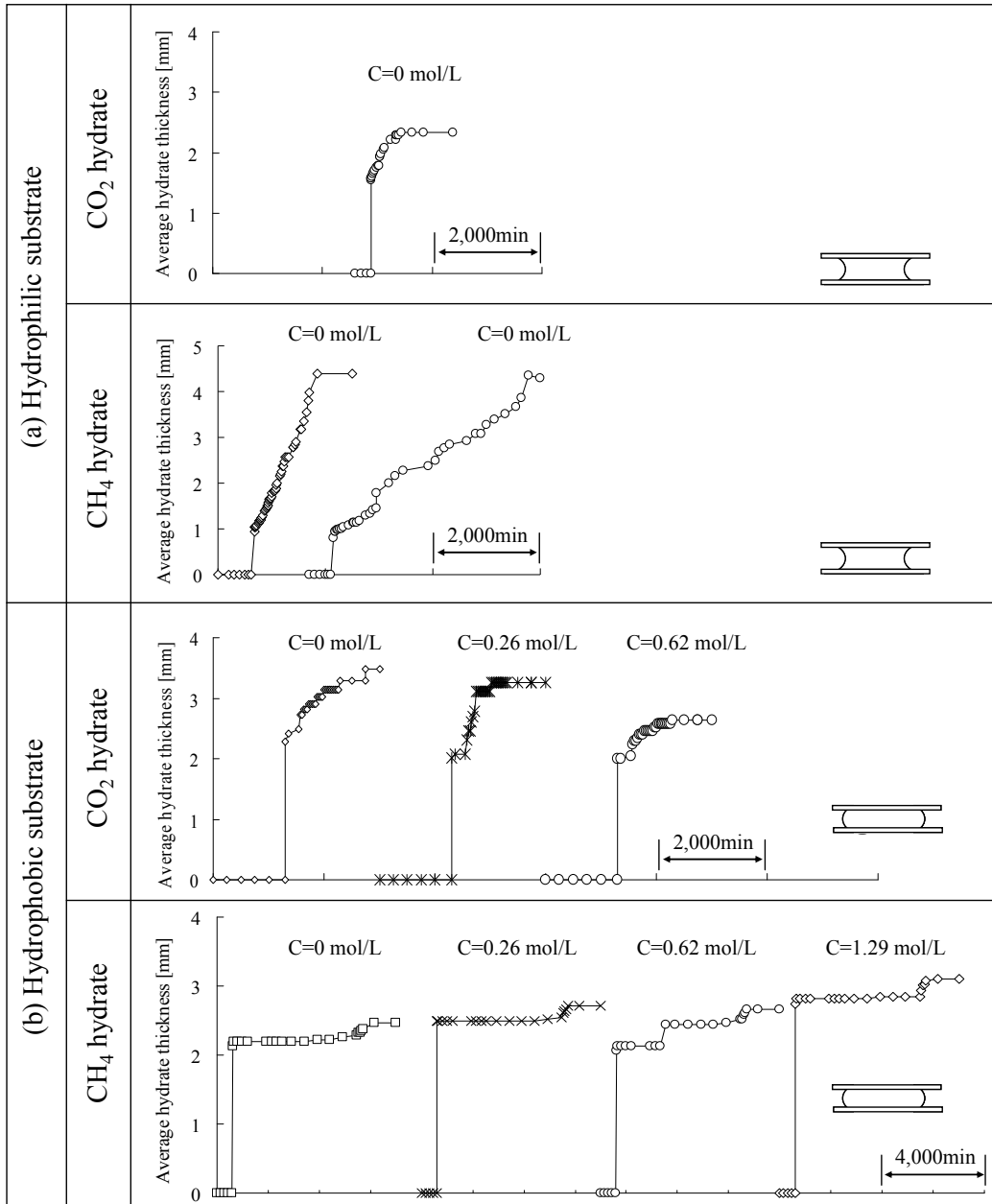


Figure 2.5. Rate of hydrate formation between plates. (a) Hydrophilic water-wet plates. (b) Hydrophobic oil-wet plates. Data for CO₂ and CH₄ hydrates.

Hydrate formation at menisci between grains. The chamber P-T conditions, the meniscus electrical resistance and changes in stiffness during hydrate formation and dissociation are monitored in this set of tests (Fig. 2.6). We do not observe a pressure drop during formation (circle on Fig. 2.6-a) because the chamber volume is much larger than the volume of water in the meniscus (approximately ~17,000 times larger). Hydrate formation causes ion exclusion and it is hindered by high salt concentration. These two processes define the evolution of electrical resistance and stiffness in these experiments. The electrical resistance is lower in drops with higher salt concentration; in all cases, electrical resistance increases after hydrate formation. The change in electrical resistance before and after hydrate formation (both CO₂ and CH₄) decreases as the salt concentration increases (Fig. 2.7).

The strength of the transmitted mechanical vibration is not sensitive to salt concentration before hydrate formation. The sensing piezocrystal output increases after hydrate formation. The increase in mechanical transmission is more pronounced when the initial salt concentration is low (both CO₂ and CH₄ hydrate) (Fig. 2.7).

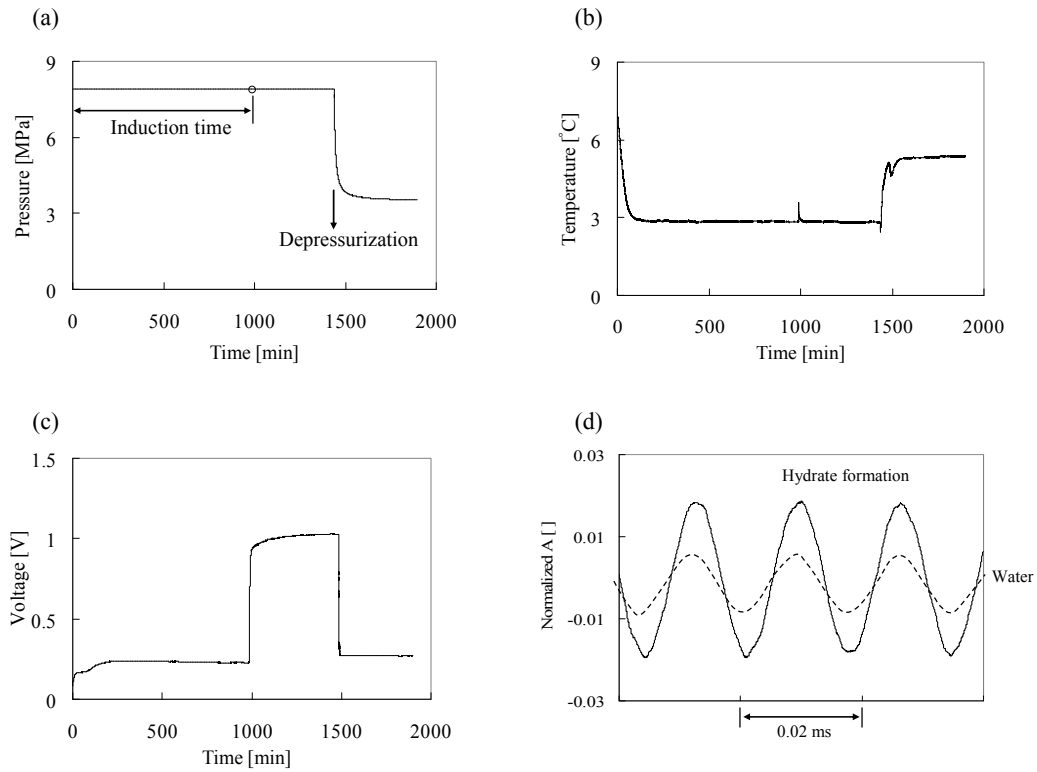


Figure 2.6. CH₄ hydrate formation in a salty solution (0.26mol/L) at the meniscus between two particles. (a) Pressure. (b) Temperature. (c) Measured voltage to be used for calculating electrical resistance. (d) Vibration detected by the receiving piezocrystal used for relative stiffness estimation.

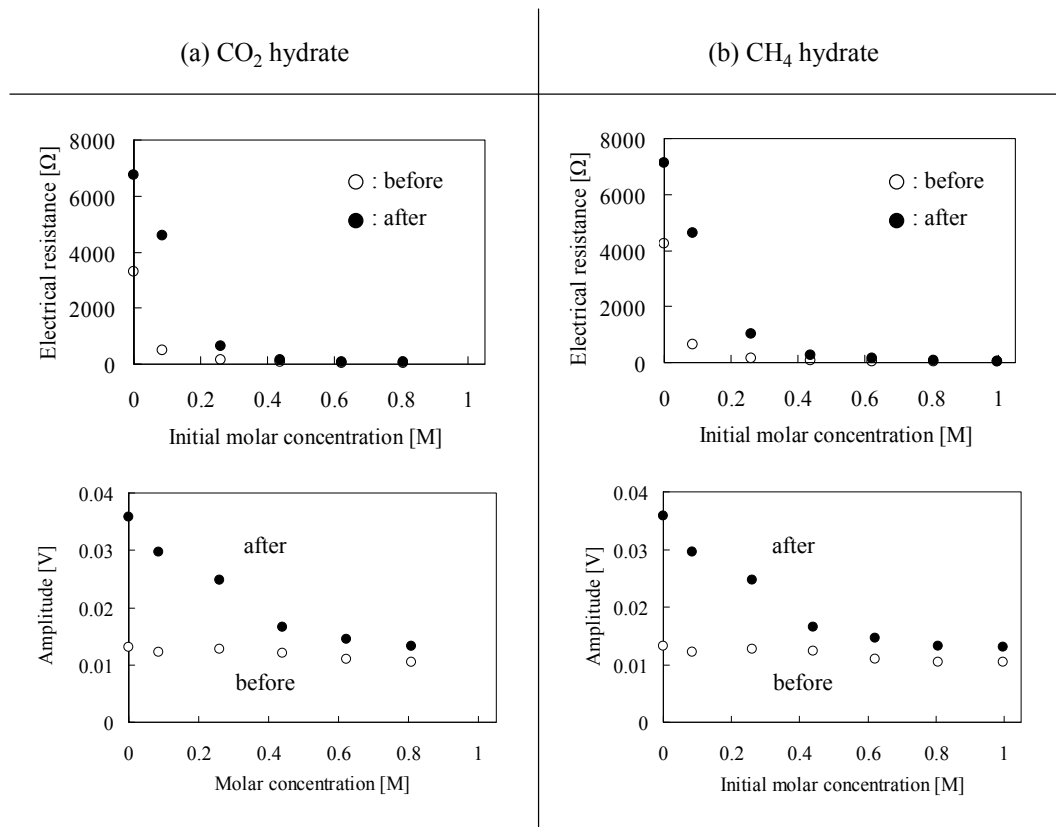


Figure 2.7. Meniscus electrical resistance and relative stiffness before and after hydrate formation for solutions with different initial ionic concentration. (a) CO₂ hydrate and (b) CH₄ hydrate. Note: Relative stiffness is defined in terms of the output voltage produced by the sensing piezocrystal.

2.5. ANALYSES AND DISCUSSION

2.5.1 Initial hydrate mass

The sudden formation of an initial hydrate mass is faster than can be justified by concurrent gas diffusion through a hydrate shell. Let's compute the hydrate thickness in terms of (1) the saturation concentration of methane in water before hydrate formation assuming that the induction time for nucleation exceeds the diffusion time ($C_{bh}=0.12\text{mol/kg}$ for CH_4 and 1.39mol/kg for CO_2), (2) the gas concentration after hydrate formation ($C_{ah}=0.063\text{mol/kg}$ for CH_4 and 0.89mol/kg for CO_2), and (3) the gas concentration in hydrate ($C_h=8.06\text{mol/kg}$ for CH_4 hydrate and 6.57mol/kg for CO_2 hydrate for a hydration number $n=6$). Then, the conservation of gas molecules requires (Fig. 2.8),

$$\pi R^2 \rho_w C_{bh} - \pi (R - h)^2 \rho_w C_{ah} = [\pi R^2 - \pi (R - h)^2] \rho_h C_h \quad (2.4)$$

The estimated initial hydrate thickness that can form by consuming the dissolved gas is $h=0.16 \mu\text{m}$ in CH_4 and $h=136\mu\text{m}$ in CO_2 hydrate (for a water droplet radius $R=4.3\text{mm}$, water density $\rho_w=1\text{g/cm}^3$ and hydrate density $\rho_{h_CO2}=1.11\text{g/cm}^3$, $\rho_{h_CH4}=0.94\text{g/cm}^3$).

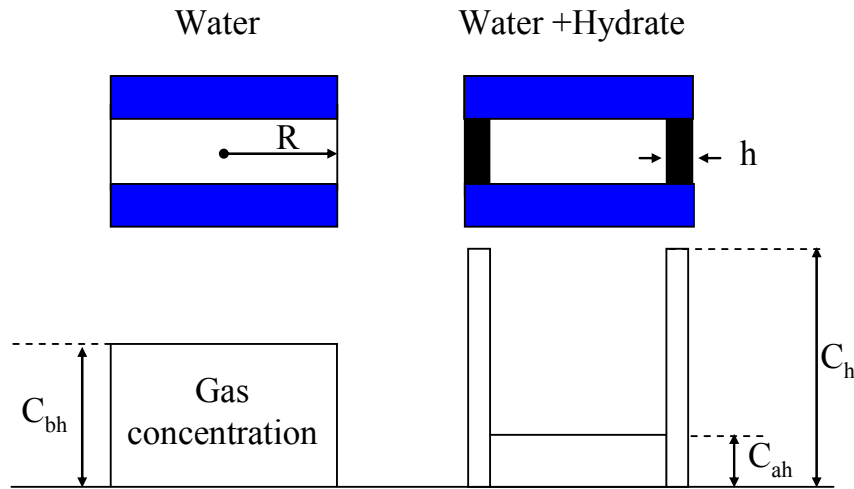


Figure 2.8. Initial, fast hydrate formation by the consumption of excess gas ($C_{bh} - C_{ah}$). (a) Before hydrate formation. (b) After hydrate formation. Note: CO₂ gas solubility in water with hydrate: $C_{ah}=0.06\text{mol/kg}$ at 3MPa, 273K. CO₂ gas solubility in water without hydrate: $C_{bh}=0.11\text{mol/kg}$ at 3MPa, 273K.

2.5.2 Hydrate growth on different substrates

Water-mineral interaction. All our data show that hydrate growth in pores takes place in discrete steps rather than gradually. The CO₂ hydrate growth rate in the context of oil-wet surfaces is between $0.38\mu\text{m}/\text{min}$ and $0.74\mu\text{m}/\text{min}$ (Figure 2.5). The hydrate growth rate in the meniscus between water-wet surfaces is higher ($0.9\text{-to-}1.9\mu\text{m}/\text{min}$) than that between oil-wet surfaces. Hence, hydrate growth is affected by sediment surface boundaries.

Shell breakage. Very slow growth rates are anticipated for diffusive gas transport through the hydrate shell. However, the fast growth rates observed in these experiments suggest that gas must reach the water inside the meniscus through discontinuities in the hydrate shell that separates the gas from the liquid water (Fig. 2.5). Complementary FEM simulations of hydrate formation around the water droplet confirm the formation of tensile fractures in the hydrate shell due to water-to-hydrate expansion ($V_{hyd}/V_w=1.23$ -to-1.28).

Hydrate growth topology. Hydrate does not grow homogeneously as a planar front but advances in the form of lobes that invade the water phase. Tensile fractures in the hydrate shell may explain lobe formation in menisci (Fig. 2.4); however, this is not the case in capillary tubes shown in Fig. 2.2. This elongated hydrate topology exhibits a higher surface area than a planar front and is consistent with hydrate formation by gas from supersaturated water: there is a shorter distance for diffusive transport to these long lobes than to a planar front. This shorter diffusive distance causes a faster initial hydrate growth (3.6-to-5.3 $\mu\text{m}/\text{min}$) than a planar front growth. Higher surface area also favors heat diffusion following phase transformation (Tabe et al. 2000).

2.5.3 Hydrate dissolution- Transients

Gas diffuses into the water mass during the induction time (Fig. 2.9-a and b). Then, rapid hydrate growth takes place and consumes the excess gas $C_{bh}-C_{ah}$ that dissolved during the induction time (Fig. 2.9-c). After this initial hydrate formation stage, gas continues diffusing into the liquid water from the gas phase supporting further hydrate

growth (path I- Fig. 2.9-c). At the same time, diffusion tends to homogenize the gas concentration at the lower tip of the hydrate mass (path II in Fig. 2.9-c); this second transport process causes dissolution at the tip. The coexistence of these two processes explains the transient formation-dissolution cycles during the first few hours, and the overall increase in hydrate mass observed in tube experiments (See Fig. 2.3).

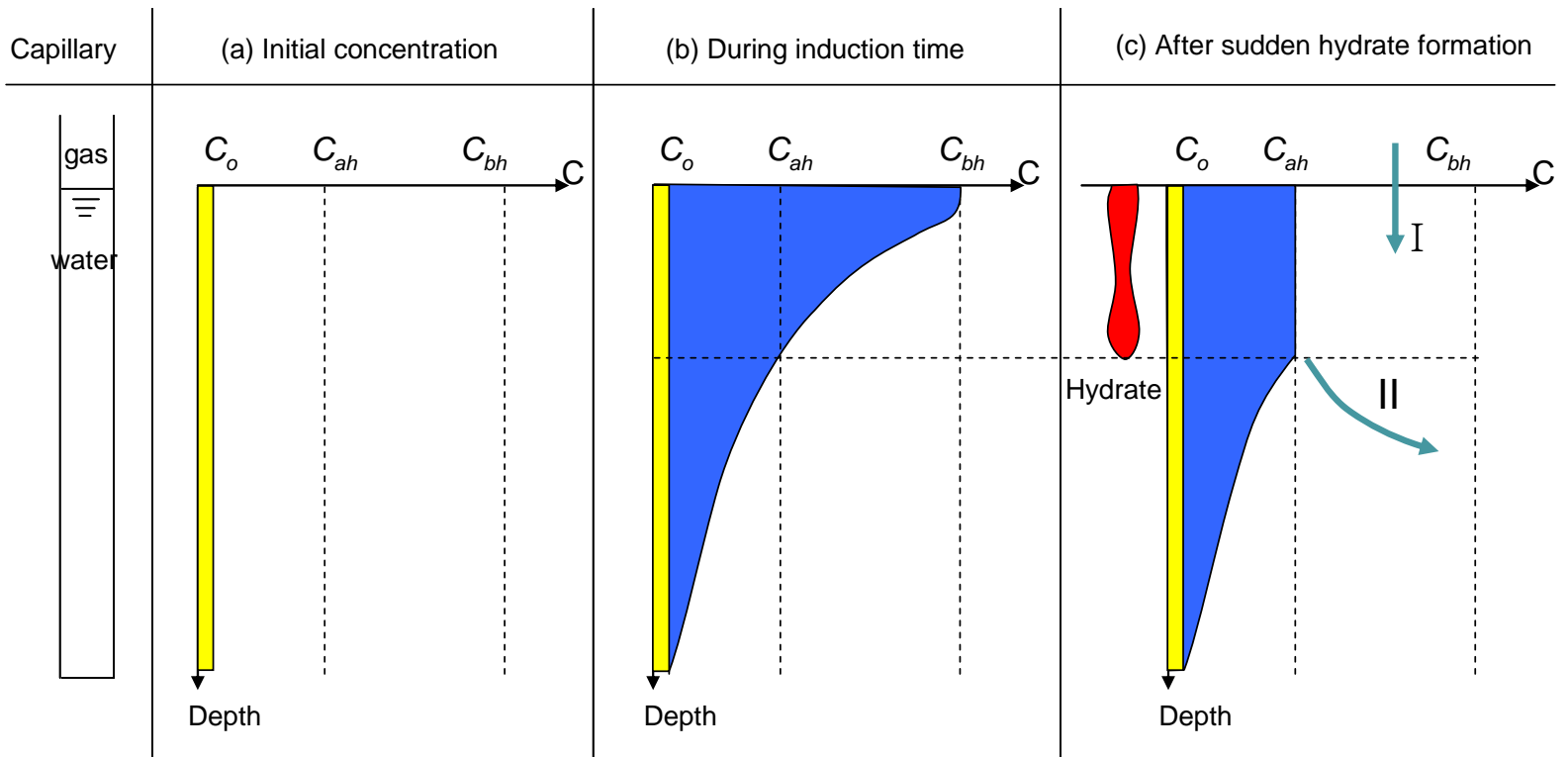


Figure 2.9. Changes in gas concentration within a capillary tube: (a) before hydrate formation, (b) after gas diffusive transport, and (c) after a sudden hydrate formation. CO_2 gas solubility in water with hydrate: $C_{ah}=0.06\text{mol/kg}$ at 3MPa, 273K. CO_2 gas solubility in water without hydrate: $C_{bh}=0.11\text{mol/kg}$ at 3MPa, 273K.

2.5.4 Relative stiffness and electrical resistivity

Relative stiffness measurements can be analyzed assuming a mechanical system made of three springs in series held between fixed boundaries to represent the source piezocrystal, the meniscus, and the receiver piezocrystal (Jung and Santamarina 2010a). The relative amplitude between the input V_i and output V_o voltages is a function of the displacement in the input piezocrystal δ_i and output piezocrystal δ_o . The latter one depends on the meniscus response $\delta_m = \delta_o - \delta_i$ through a function that combines the stiffness of piezocrystals k_{piezo} , the meniscus height L_m , the medium Young's modulus E_m , and the area of the meniscus A_m ,

$$\frac{V_o}{V_i} = \alpha \frac{\delta_o}{\delta_i} = \alpha \frac{\delta_o}{\delta_o + \delta_m} = \alpha \frac{1}{1 + \frac{k_{piezo} L}{E_m A_m}} \quad (2.5)$$

Electrical current flows through the free water that remains inside the hydrate shell. Therefore, when an annular CH₄ hydrate shell forms, the measured resistance reflects the contributions of water and hydrate (Jung and Santamarina 2010a). Electrical resistance R is a function of resistivity ρ , meniscus length L_m area A_m , and a shape factor β ,

$$\begin{aligned} \frac{1}{R_{water+hyd}} &= \frac{1}{R_{hyd}} + \frac{1}{R_{water}} \\ &= \frac{1}{\beta \cdot L} \left(\frac{A_{total} - A_{water}}{\rho_{hyd}} + \frac{A_{water}}{\rho_{water}} \right) \\ &\approx \frac{1}{\beta \cdot L} \frac{A_{water}}{\rho_{water}} \end{aligned} \quad (2.6)$$

The simplification in the last equality recognizes that the electrical conductivity of hydrate is much lower than the conductivity of salt water.

The relative amplitude V_i/V_o from the mechanical excitation (Eq. 2.4) and electrical resistance $R_{water+hyd}$ (Eq. 2.5) are proportional to the hydrate area A_m . The analysis of experimental results shown in Fig. 2.7 using these expressions leads to the conclusion that the final hydrate thickness decreases as the initial salt concentration in the meniscus increases.

2.5.5 Ion exclusion - Salt precipitation - Salt limited hydrate growth

The ionic concentration $C(h)$ in the free water that remains inside the hydrate shell increases during hydrate growth as a consequence of ion-exclusion; from mass concentration, $C(h)=C_o[1-(h/r)^2]$. The back analysis of experimental results in Fig. 2.7 shows that the molar concentration may reach salt saturation and salt may precipitate during hydrate growth.

On the other hand, ions and gas molecules compete for water, and the hydrate phase boundary shifts to lower temperature and higher pressure with increasing salt concentration (Duan and Sun 2006; Masoudi et al. 2005; Mohammadi and Tohidi 2005; Østergaard et al. 2005). Eventually, hydrate formation may stop for a given P-T condition. Our P=8MPa and T=275K conditions for CH₄ hydrate correspond to the phase boundary for a salt concentration of $c=4.0M$ (Østergaard et al. 2005). We

conclude that hydrate formation in our tests ended due to the high concentration of salt in the liquid water inside the hydrate shell. Low ionic and gas diffusive transport through the hydrate shell will render the gas-hydrate-brine system stable for relatively long periods.

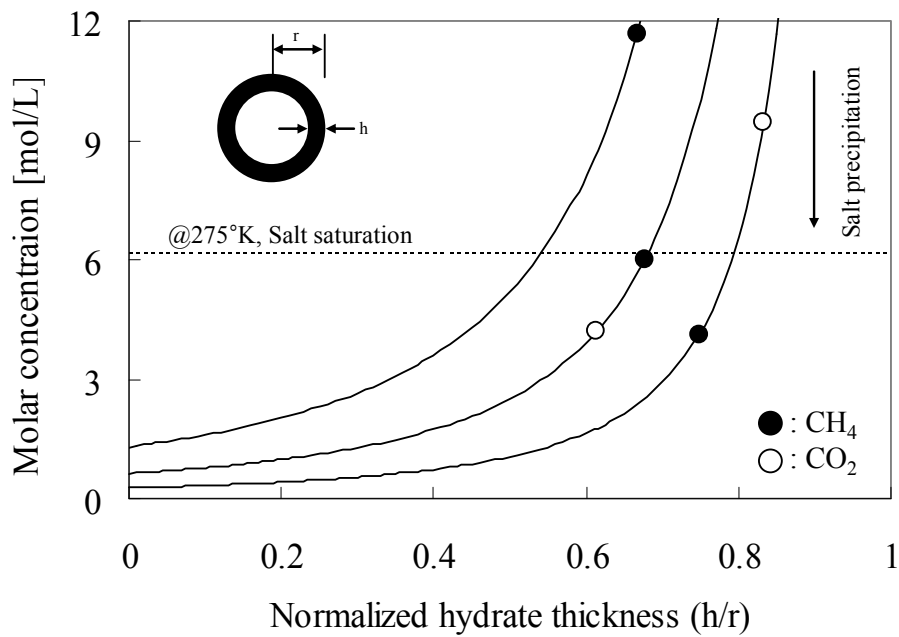


Figure 2.10. Change in salt concentration by ion exclusion as a function of hydrate thickness. Lines show the increase in salt concentration in the remaining free water during hydrate growth. The dotted line shows the salt concentration saturation at 275°K. Points represent final hydrate thickness and molar concentration estimated for the experiments reported in Fig. 2.7.

2.6. CONCLUSIONS

Hydrate formation implies a pronounced transition from a condition of low gas concentration in water to a condition of high gas concentration in hydrate. In addition, the concentration of gas in water is lower in the presence of hydrate and it is crystal size dependent. These phenomena suggest complex nucleation and growth processes and anticipate the emergence of unexpected phenomena, including transient formation/dissociation.

Initial hydrate formation is fast and consumes gas dissolved in water during induction time. The solubility of CO_2 in water is higher than that of CH_4 , therefore, a larger mass of CO_2 hydrate may form during early growth.

Fast growth rates cannot be justified by diffusive gas transport through the hydrate shell that separates the gas from the liquid water. We anticipate that successive hydrate formation and water-hydrate volume expansion create tensile discontinuities in the hydrate shell, which facilitate gas transport.

Hydrate does not grow homogeneously as a planar front but advances in the form of lobes that invade the water phase. These lobes may correspond to discontinuities in the hydrate shell. However, the early lobe topology in capillary tubes provides a higher surface and a shorter distance for diffusive gas transport from the bulk water. This shorter diffusive distance supports a faster early hydrate growth.

Rapid hydrate growth after the induction time consumes the excess gas ($C_{bh}-C_{ah}$) that dissolved by diffusive transport. Thereafter, diffusion at the tip of the hydrate mass causes dissolution. These processes explain transient formation-dissolution following early hydrate growth.

CHAPTER III

HYDRATE ADHESIVE AND TENSILE STRENGTHS

3.1. INTRODUCTION

Gas hydrates consist of guest gas molecules encaged in water molecules. The most common gas molecule is methane, an abundant potential source of energy, with worldwide reserves on the order of 500 to 10,000 Gt of carbon (Collett 2002; Kvenvolden 1988; Ruppel and Pohlman 2008). Geo-mechanical analyses of hydrate-bearing sediments are necessary to assess instabilities that may occur during or after gas production, or from natural processes that may cause dissociation in hydrate-bearing sediments (Nixon and Grozi 2007; Rutqvist and Moridis 2007; Rutqvist et al. 2009).

The strength of hydrate-bearing sediments is affected by the hydrate tensile strength and the adhesive strength between hydrates and minerals. However, most of the available strength data correspond to compressive loading. The purpose of this study is to determine the adhesive and tensile strengths of CH₄ hydrate, CO₂ hydrate, tetrahydrofuran THF hydrate, and ice on calcite and mica substrates.

3.2. PREVIOUS STUDIES

The tensile and bonding strengths result from the contribution of both short-range (covalent, ionic, and metallic bonds) and long-range (Van der Waals and hydrogen bonds). Long-range molecular interactions prevail in adhesion (Adamson 1997; Braga et al. 1999; Marshall et al. 2010; Megaw 1973; Petrie 2007; Seddon and Zaworotko 1999). Water and mineral interaction before hydrate formation are determined by surface charge. Mica (Muscovite- $K_2O \cdot Al_2O_3 \cdot SiO_2$) has a negative surface charge at its equilibrium pH, forms a strong hydrogen bond with water, and exhibits a low contact angle ($\theta < \sim 5^\circ$). On the other hand, calcite ($CaCO_3$) has a positive surface charge, forms a weak bond with water (Maslova et al. 2004; Osawa et al. 2008), and the water-vapor-calcite contact angle is high ($\theta \approx \sim 37^\circ$).

After phase transformation, ice or hydrate can mobilize additional mechanical interaction effects with the mineral. For example, an increase in surface roughness typically results in greater adhesive strength due to an increase in the total effective area available for adhesion and the development of mechanical interlocking (Adamson 1997; Petrie 2007). We note that a thin liquid-like layer remains between ice-or-hydrate and the mineral surface; suction in this layer dominates the adhesive strength between the hydrate and atomically smooth mineral surfaces (Churaev 2004; Fan et al. 2003; Jellinek 1959; Maslova et al. 2004; Nicholas et al. 2009; Tsionsky et al. 2005; Yang et al. 2004).

Previous studies on the strength of ice and hydrate emphasized compressive strength. The compressive strength of ice is inversely proportional to temperature and it can range from 5MPa at 0°C to 25MPa at -20°C (Petrovic 2003). The tensile strength of ice is less sensitive to temperature and varies from 0.7MPa at 0°C to 3.1MPa at -20°C (Petrovic 2003). The ratio between the tensile σ_t and compressive σ_c strengths for ice varies with temperature T [°C] as follows (Petrovic 2003),

$$\sigma_c / \sigma_t = -0.1789 \cdot T + 3.9653 \quad \text{between } 0^\circ\text{C and } -35^\circ\text{C} \quad (3.1)$$

Both tensile and compressive strengths are proportional to strain rate, but inversely proportional to specimen size and grain size (Petrovic 2003) . The ice-substrate adhesive strength depends on the material. Reported values include $\sigma_i=0.21$ -to- 0.34 MPa for ice-aluminum -10°C (Javan et al. 2006), $\sigma_i=0.19$ -to- 0.33 MPa for ice-polystyrene at -5°C, and $\sigma_i=0.53$ -to- 0.54 MPa for ice-stainless steel at -10°C (Jellinek 1959).

The compressive strength of methane hydrate can be 20 times higher than that of ice (Durham et al. 2003a). The compressive strength of methane hydrate is inversely proportional to temperature and directly proportional to strain rate and confining pressure (Durham et al. 2003a; Durham et al. 2003b; Hyodo et al. 2002; Nabeshima and Takai 2005; Stern et al. 1996; Stern et al. 1998; Stern et al. 2000). The range of the adhesive strength between two THF hydrate particles is affected by the contact duration t^* and the temperature (Taylor et al. 2007a; Yang et al. 2004).

Table 3.1. Ice and hydrate strengths – Compilation of published results

Material	Strength Mode	Strength [MPa]	Conditions	References
Ice	Tensile strength	0.7-to-3.1	T= 253-273K, Strain rate = 10^{-8} - 10^{-3} s ⁻¹	(Petrovic 2003)
		0.8-to-1.3	T= 263K, Strain rate= 10^{-6} s ⁻¹	(Currier and Schulson 1982)
	Compressive strength	5-to-35	T= 253-273K, Strain rate = 10^{-8} - 10^{-3} s ⁻¹	(Petrovic 2003)
Ice-substrate	Adhesive shear strength	0.21-to-0.34	Aluminum substrate, T= 263K	(Javan et al. 2006)
		0.53-to-0.54	Stainless steel substrate, T= 263K	(Jellinek 1959)
		0.19-to-3.3	Polystyrene substrate, T= 263K	(Jellinek 1959)
		0.015-to-0.084	Between ice substrates in air, T= 267-270K	(Fan et al. 2003)
		0.001-to-0.002*	Between ice substrate in air, T= 263-271K	(Yang et al. 2004)
Methane Hydrate	Compressive strength	2-to-10	T= 243-263K, Confining pressure: 2-6MPa Strain rate= 6-120 s ⁻¹	(Nabeshima and Takai 2005)
		55.7-to-101.7	T= 260-287K, P= 10-15MPa Confining pressure:50 MPa Strain rate = 10^{-8} - 10^{-5} s ⁻¹	(Durham et al. 2003a)
		62-to-102	T= 140-260K, Strain rate = 10^{-6} - 10^{-4} s ⁻¹ Confining pressure: 50-100Mpa	(Stern et al. 1996; Stern et al. 1998; Stern et al. 2000)
		2-to-10	T= 243-278K, Confining pressure:0-8 MPa Strain rate= 6-60 s ⁻¹	(Hyodo et al. 2002)
THF Hydrate + substrate	Adhesion strength	0.0006-to-0.0025*	T= 261-275, Atmospheric pressure, THF hydrate	(Taylor et al. 2007a)
		0.0007-to-0.0014*	Between THF substrates T= 263-271K	(Yang et al. 2004)

Note: * estimated from the published results

3.3. EXPERIMENTAL STUDY

3.3.1 Equipment and Materials

Device for tensile stress measurements. Two substrates of the same mineral are positioned parallel to each other to form a cylindrical ice and hydrate body between them (Fig. 3.1). One substrate rests on a rigid cantilever beam that is instrumented with a full strain gauge bridge to measure the pull-out force. The full bridge circuit has two active gauges and two dummy gauges for temperature compensation. The cantilever beam load cell is calibrated using weights. The other substrate is mounted on a deformation-controlled driver that is used to impose the horizontal pull-out motion (Fig. 3.1).

Pressure chamber. The device is placed inside a high pressure chamber that has a sapphire window to observe the evolution of the test. The chamber is surrounded by a copper pipe and an insulation layer to control temperature. Cell pressure and temperature are continuously recorded using a data logger.

Materials. Two mineral substrates are used in this study: mica (Muscovite- $\text{K}_2\text{O}\cdot\text{Al}_2\text{O}_3\cdot\text{SiO}_2$) and a calcite crystal (CaCO_3). Substrates are cemented onto two steel pedestals that are mounted on the cantilever beam and the deformation-controlled driver. The guest molecules selected for hydrate formation are CH_4 , CO_2 , and THF. The THF solution is 81% H_2O and 19% THF by mass to form 100% hydrate (i.e., stoichiometric

mixture THF·17H₂O). An additional series of tests are conducted on ice.

3.3.2 Test Procedure

Specimen preparation. The instrumented cantilever beam, the deformation controller and the chamber are assembled together. A 2.7mm gap is left between the two parallel substrates. Then, a droplet of water is placed between the substrates to form a quasi-cylindrical specimen (height=2.7mm, diameter=4.8-to-8.6mm, mass=63-to-202mg). Finally, the chamber is closed and ready for testing.

Ice and Hydrate formation. Ice forms at atmospheric pressure and tests are conducted at a temperature of -5°C. The THF solution forms clathrate hydrate structure II under an atmospheric pressure of ~4.4°C; therefore, the THF hydrate is tested at less than ~0°C. The two gas hydrates are formed by filling the chamber with gas, followed by a pressure increase (~8MPa for CH₄ hydrate and at ~3.5MPa for CO₂ hydrate) while lowering the temperature to ~2°C. Hydrate formation is confirmed by visual inspection through the sapphire window (Fig. 3.2-a and b) and by the exothermic response detected with the thermocouple.

Tensile load. The pull-out test is run about ~10 hours after hydrate or ice formation. Note that the induction time for hydrate formation ranged from 8-to-17hrs; for comparison, the diffusion time for CO₂ and CH₄ gas in water is around $t=(d/2)^2/D=1.6$ -to-5.1hrs [Note. d =radius of meniscus, D =diffusivity - data in Table 7.4]. The bridge output is recorded every 2 ms and converted to force using the calibrated response. The

pull-out force increases until failure (Fig. 3.3).

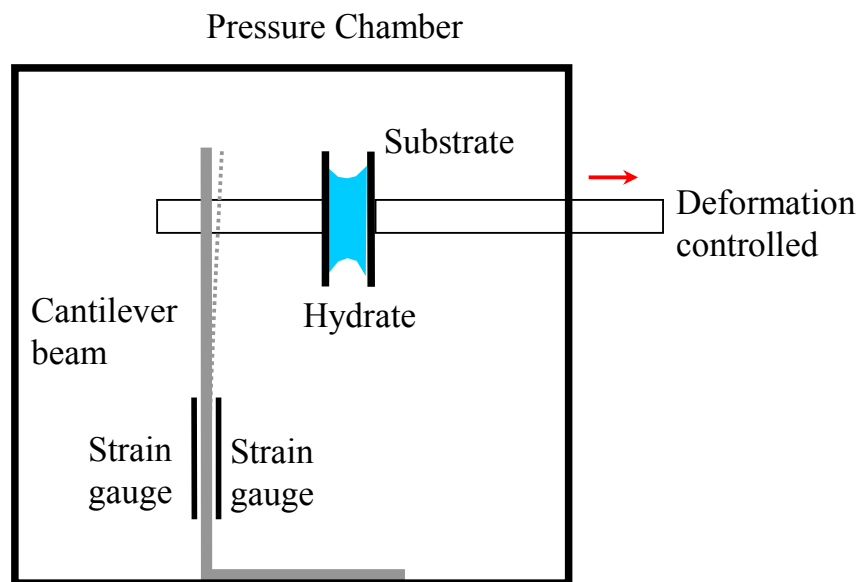


Figure 3.1. Device built to measure tensile strength. The load cell consists of a cantilever beam instrumented with strain gauges. The device is placed inside P-T controlled pressure chamber.

3.4. EXPERIMENTAL RESULTS

Tensile or debonding failure is determined from microphotographs obtained through the sapphire window immediately after the failure (examples in Fig. 3.2-c). When mica is the substrate, debonding failure occurs, in all cases, both for all hydrates (e.g., CH₄ hydrate, CO₂ hydrate, THF hydrate) and for ice. When calcite is involved, the failure mode is tensile failure for CH₄ and CO₂ hydrates and debonding failure for THF hydrate and ice (See summary in Fig. 3.4).

Both the THF solution and water convert into a 100% solid mass of THF hydrate and ice. In these two cases, the pull-out force is divided by the specimen cross-sectional area to compute strength. The computation of strength is more complex in the case of diffusion- and solubility-limited CO₂ and CH₄ hydrate formation. The hydrate thickness can be estimated as a function of the induction time before hydrate formation and the hydrate growth rate before loading. Data in Table 3.2 suggest that the hydrate thickness 10 hr after initial formation can reach 1.9-to-2.3 mm when hydrophilic substrates are used and 2.1-to-2.3 mm on hydrophobic substrates. Using these values, we compute an upper bound for the tensile strength of CH₄ and CO₂ hydrates. The lower bound strength is estimated assuming that the complete water mass converted into hydrate. Results in Fig. 3.4 show (a) that the adhesive strength is higher when calcite is involved (this applies to all case, including CO₂ and CH₄ hydrates which failed in tension before debonding), and (b) that the pull-out strength limited by either tensile or adhesive failure will rarely exceed 200kN/m². Calcite surfaces used in this study were rougher than the atomically-

smooth freshly-peeled mica surface (See also Szoszkiewicz et al. 2005). Increased surface area available and mechanical interlocking can explain the higher adhesive strengths exhibited by all hydrates and ice when calcite was involved.

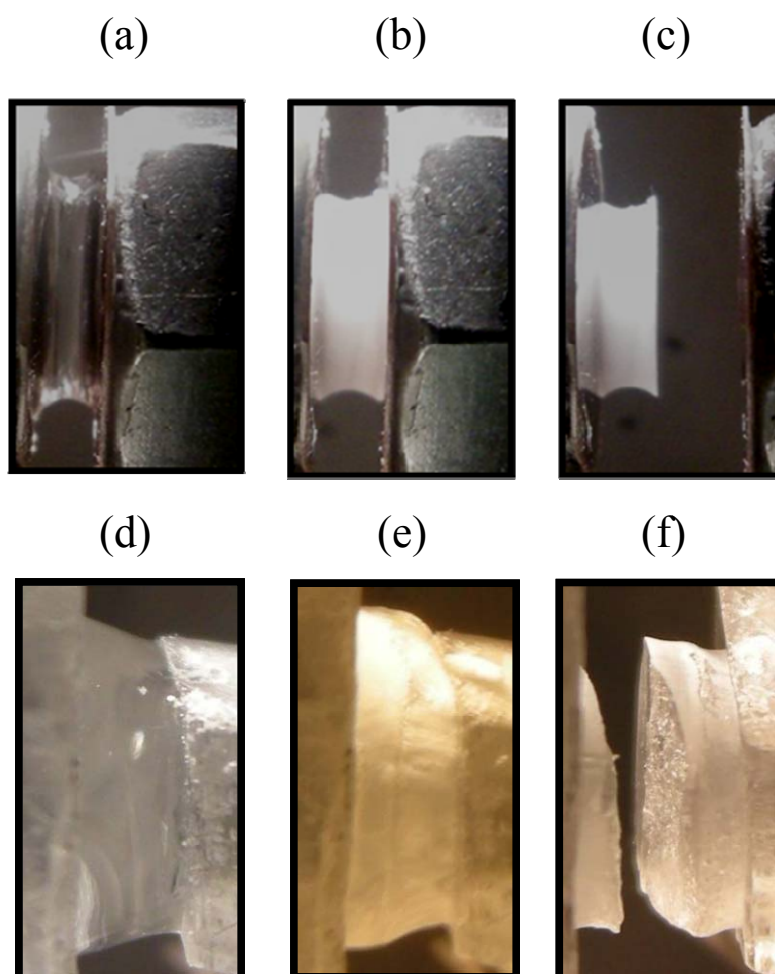


Figure 3.2. Experimental results: (a) water meniscus between mica substrates, (b) CH₄ hydrate formation, (c) adhesive failure between CH₄ hydrate and mica substrate, (d) water meniscus between calcite substrates, (e) CH₄ hydrate formation, (f) tensile failure between CH₄ hydrate and calcite substrate.

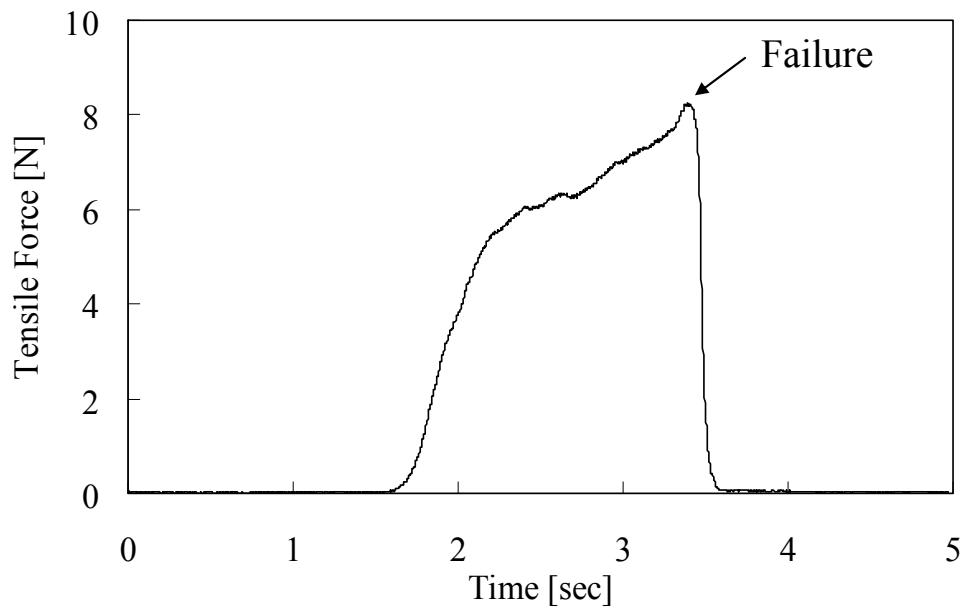


Figure 3.3. Typical force-time response (Case: CH₄ hydrate on a calcite substrate).

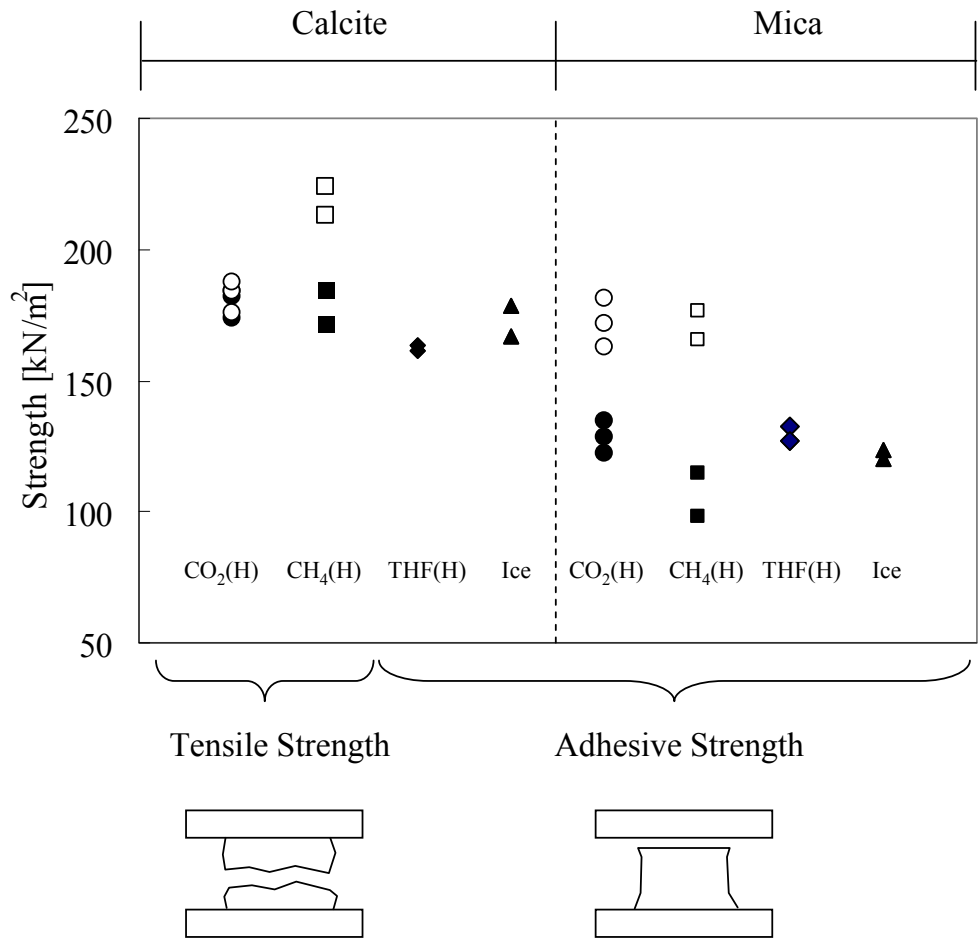
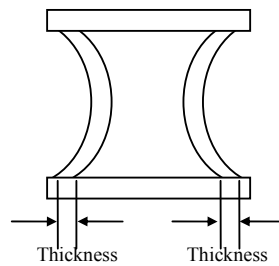


Figure 3.4. Hydrate adhesive and tensile strengths. Assumed cross section: filled symbols correspond to 100% formation while empty symbols correspond to annular hydrate formation.

Table 3.2. Hydrate thickness

Time [min]	Hydrophilic substrate		Hydrophobic substrate	
	CH ₄ hydrate thickness[mm]	CO ₂ hydrate thickness [mm]	CH ₄ hydrate thickness [mm]	CO ₂ hydrate thickness [mm]
0	0.9	1.5	2.1	2.3
200	1.2	2.0	2.2	2.7
400	1.5	2.2	2.2	2.9
600	1.9	2.3	2.2	3.0



3.5. ANALYSES AND DISCUSSION

Implication on the shear strength of hydrate-bearing sediments. Published experimental results show that the shear strength τ_f of hydrate-bearing sediments is a function of the normal stress σ_n , the friction angle ϕ , hydrate saturation S_h , and hydrate habit in pores (Ebinuma et al. 2005; Hyodo et al. 2008; Masui et al. 2005b; Yun et al. 2007). The micromechanical model sketched in Fig. 3.5 is analyzed next to assess the interplay between these parameters. From force equilibrium (Note: the compressive resistance of a transverse hydrate “truss” is not included in this analysis),

$$T = N \cdot \mu + a \cdot \sigma_t \cdot \cos 45^\circ \quad (3.2)$$

Mechanical and geometric considerations lead to (See details in Fig. 3.5),

$$\tau_f = \frac{T}{4R^2}; \quad \sigma_n = \frac{N}{4R^2}; \quad S_{hyd} = \frac{a(\sqrt{2}-1)}{4R^2 \left(2 - \frac{\pi}{3}\right)} \quad (3.3)$$

Then, equation 3.2 can be written in terms of equivalent continuum parameters,

$$\tau_f = \sigma_n \tan \phi + 1.6 S_{hyd} \sigma_t \quad (3.4)$$

This expression provides a first-order physical explanation to the effect of hydrate on

the shear strength of hydrate-bearing sediments and shows that the hydrate tensile strength determines the Mohr-Coulomb cohesive intercept. Clearly, an alternative hydrate pore habit will have a different effect on strength.

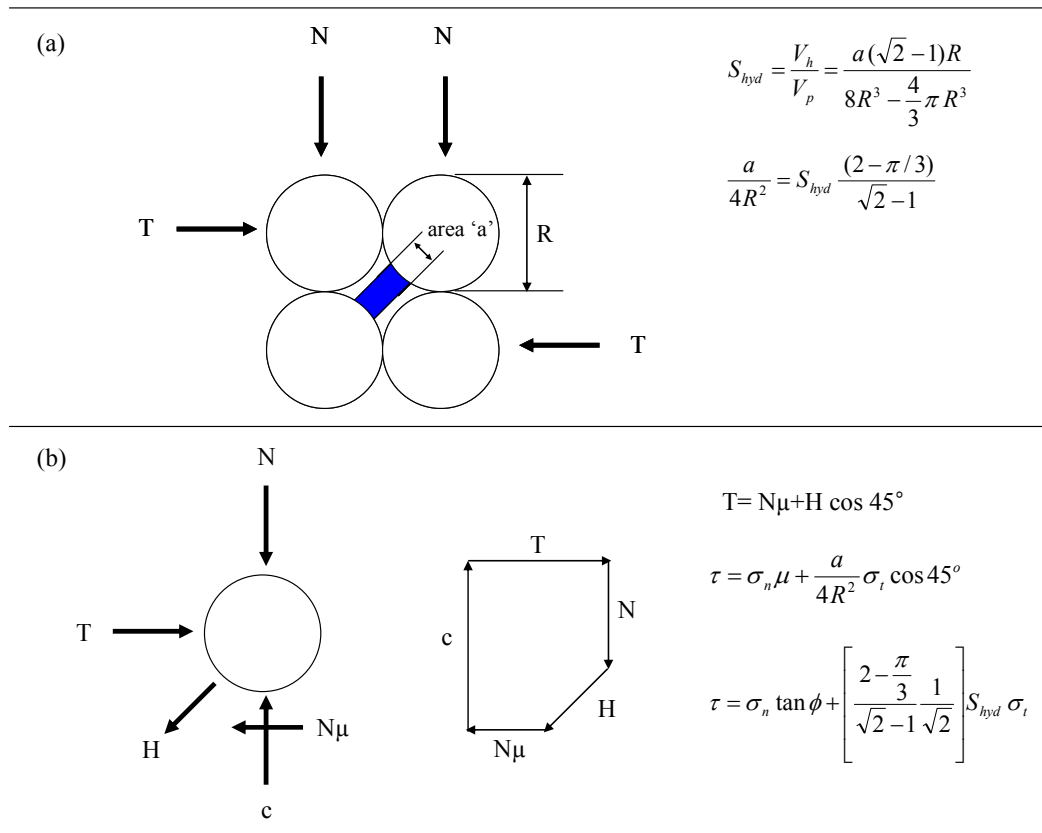


Figure 3.5. The reference of tensile/ adhesive hydrate strength on the shear strength of hydrate-bearing sediments. (a) Bonded hydrate mass in a simple cubic packing configuration. (b) Force diagram for a single particle.

Local hydrate dissociation. We conducted FEM simulations to study the change in internal pressure within the hydrate mass during tensile loading in an axisymmetric configuration (Fig. 3.6). Results show that the internal pressure at the center of the hydrate mass decreases and eventually moves outside the hydrate stability field. This suggests the possibility that the tensile failure of a hydrate mass may be the result of local stress conditions that cause hydrate dissociation.

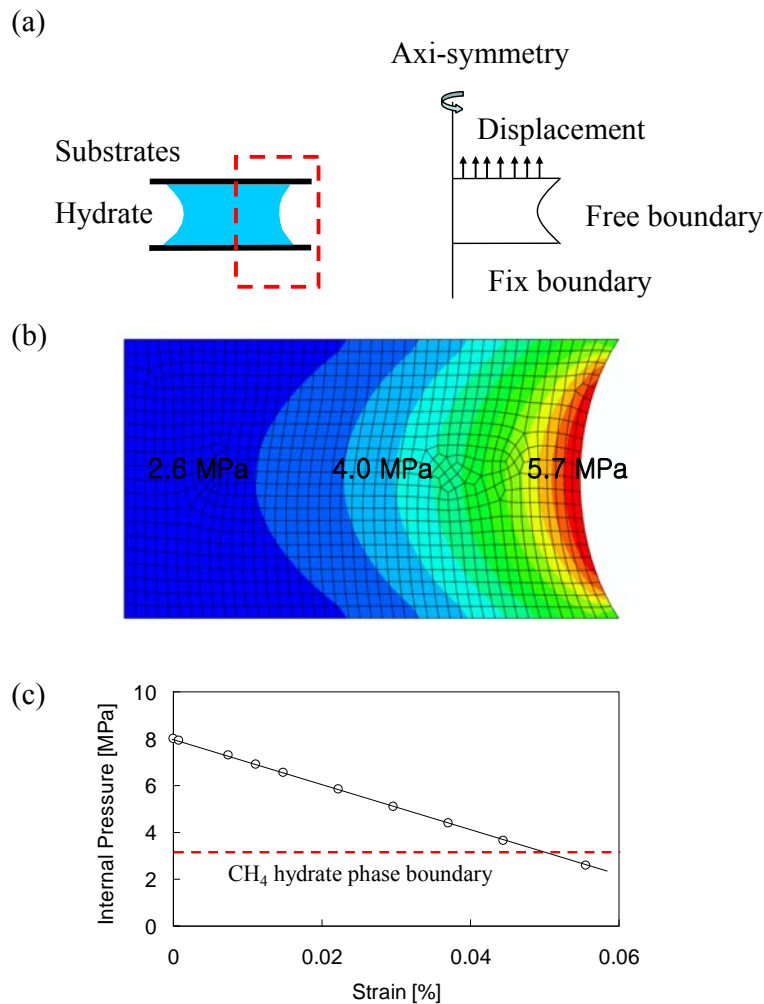


Figure 3.6. Internal pressure change during tensile loading. (a) Boundary conditions for FEM simulation. (b) Numerical results (Case: displacement=0.055%, E=8.2 GPa, $\nu=0.32$, P=8.0 MPa). (c) Internal pressure change during pull out as a function of the imposed strain.

3.6. CONCLUSIONS

The hydrate-mineral adhesive strength and the tensile strength of the hydrate mass itself affect the mechanical response of hydrate-bearing sediments.

Both tensile and debonding failures are dependent on mineral substrates. When the mica is the substrate, debonding failure occurs for all hydrates (e.g., CH₄ hydrate, CO₂ hydrate, THF hydrate) and for ice. When calcite is involved, the failure mode is tensile failure for CH₄ and CO₂ hydrates and debonding failure for THF hydrate and ice. Therefore, the adhesive strength is higher when calcite is involved in all cases, in part because calcite surfaces are rougher than atomically-smooth freshly-peeled mica surfaces.

An upper bound for the tensile strength of the hydrate mass for CH₄ and CO₂ is obtained assuming a reduced hydrate thickness to obtain a value of 200±30 kN/m². A lower bound is estimated assuming that the complete water mass converted into hydrate leading to ~180 kN/m².

Numerical FEM simulation results suggest the possibility that the tensile failure of the CO₂ and CH₄ hydrate mass may result from local hydrate dissociation during tensile loading due to an effective decrease in internal pressure.

The hydrate adhesive and/or tensile strength affects the strength of hydrate-bearing sediments. A particle-scale micromechanical model shows that the tensile strengths determine the Mohr-Coulomb cohesive intercept.

CHAPTER IV

**STRESS-STRAIN RESPONSE OF HYDRATE-BEARING
SEDIMENTS: NUMERICAL STUDY USING DEM SIMULATION**

4.1. INTRODUCTION

Gas hydrates are found in marine and permafrost sediments. The stiffness, strength and volume change behavior of hydrate-bearing sediments are important parameters for the analysis of near well conditions (Masui et al. 2005a; Rutqvist and Moridis 2007), for reservoir simulation in view of production strategies, as well as for the analysis of seafloor stability (Nixon and Grozi 2007) .

Triaxial compression, direct shear strength and bending tests have been used to study the mechanical properties of hydrate-bearing sediments (Ebinuma et al. 2005; Hyodo et al. 2008; Masui et al. 2005b; Ohmura et al. 2002; Yun et al. 2007). Published data suggest that the stiffness, strength and dilative tendency of hydrate-bearing sediments increase with hydrate saturation and are affected by hydrate formation history, initial confining stress, and temperature (Ebinuma et al. 2005; Hyodo et al. 2008; Ohmura et al. 2002; Yun et al. 2007: see reviews in Soga et al. 2006 and in Waite et al. 2009). In particular, the stress-strain response of hydrate-bearing sediments is affected by pore-habit; for example, hydrate formation at interparticle contacts causes a greater increase in strength and stiffness than pore filling hydrate. However, difficulties in controlling hydrate

formation, distribution and saturation challenge the proper interpretation of laboratory studies.

In this manuscript, we use the discrete element method (DEM) to model hydrate-bearing sediments in order to improve our understanding of their stress-strain response and to gain insight into underlying particle-level processes. We explore the effects of hydrate distribution, saturation, sediment porosity, and confining stress.

4.2. NUMERICAL SIMULATION

We use the commercially available discrete element code PFC3D (Particle flow Code in Three Dimensions v3.10). Specimen preparation and simulation details follow.

4.2.1 Specimen preparation

Specimens are formed within a stress-controlled cylindrical volume (diameter=10mm, height= 20mm). Small mineral grains, twice smaller than their target size, are randomly placed within the cylindrical volume. Gradually, the mineral grains are enlarged to their target diameter to form the initial hydrate free sediment packing (gaussian diameter distribution between 0.62 mm to 0.82 mm - Fig. 4.1-a). The hydrate-free sediment is then subjected to isotropic confinement ($\sigma'_o=0.1\text{MPa}$ to 1MPa). Two values of initial porosity before confinement are generated to simulate both loose $n= 0.532$ (3,762 particles) and dense $n= 0.402$ (4,806 particles) conditions.

We explore two different hydrate pore-habits. “Distributed hydrate” is simulated with small hydrate particles that randomly bond onto mineral grains (similar to studies of cemented soil in Wang and Leung, 2010). Hydrate particles are randomly placed within the sediment pores after consolidation to the pre-determined isotropic stress σ_o' (Fig. 4.1-b). Initially, hydrate particles are 10 times smaller than the target size; then, they are gradually enlarged to the target diameter of 0.22 mm which is about 1/3 the diameter of the mineral particles. Finally, hydrate particles are randomly displaced in one of 20 different directions until they attach onto mineral surfaces. The parallel-bond model in PFC-3D is used to impose the bonding strength between hydrate and mineral particles. Bond strength and stiffness are obtained from experimental results reported in (Jung and Santamarina 2010b). The number of hydrate particles added to the sediment is used to control the hydrate saturation S_h between 0 and 50%. The total number of hydrate particles reaches 74,940 for $S_h=50\%$ in sediments with initial porosity $n=0.532$.

The second pore-habit “Patchy saturation” consists of clusters of mineral grains with 100% hydrate saturation (bounded mineral particles) inside hydrate-free sediment mass (Fig. 4.1-c). Each cluster consists of 15-to-30 mineral grains. Cluster size and the number of clusters determine the global hydrate saturation (between $S_h=0$ and 50%). Parallel-bonding is added between mineral grains that are part of the clusters after the sediment has been consolidated to the predetermined isotropic stress σ_o' . A high bonding strength of 2 MPa is used to prevent cluster breakage during deviatoric loading.

All other simulation parameters are the same in both cases: normal contact stiffness 1×10^7 [N/m], shear stiffness 1×10^7 [N/m], interparticle friction coefficient $\mu = 0.5$, and specific gravity $G_s = 2.65$.

4.2.2 Triaxial Compression Test Simulation

The top and bottom caps are modeled as rigid frictionless plates. Axial deviatoric loading is applied while keeping a constant confining pressure σ_c on the cylindrical wall. We simulate tests for various initial sediment porosities, hydrate saturations, and confining stresses for the two different hydrate pore-habits.

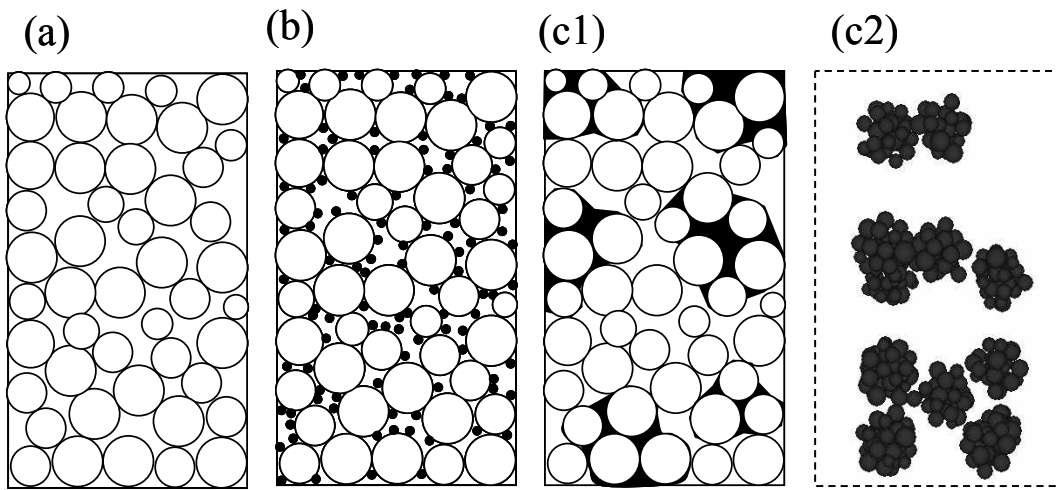


Figure 4.1. Simulation of hydrate bearing sediments. (a) Hydrate-free sediments. (b) Distributed hydrate. (c) Patchy hydrate saturation: C1 shows a 2D schematic; C2 shows grain clusters in 3D. Clusters have 100% hydrate saturation while the sediment matrix has no hydrate (transparent in Figure c2).

Table 4.1 Material properties

Soil particles

Soil particle density [kg/m ³]	2650
Initial porosity	0.402, 0.532
Particle radii ranges [m]	0.62×10^{-3} -to- 0.82×10^{-3}
Interparticle friction coefficient	0.5
Normal contact stiffness [N/m]	1×10^7
Shear contact stiffness [N/m]	1×10^7

Distributed hydrate

Soil particle density [kg/m ³]	2650
Particle radii ranges [m]	0.22×10^{-3}
Bond radius [m]	0.22×10^{-3}
Normal contact stiffness [N/m]	1.54×10^8
Shear contact stiffness [N/m]	1.54×10^8
Normal bonding strength [N/m ²]	2×10^5
Shear bonding strength [N/m ²]	2×10^5

Patchy hydrate saturation

Soil particle density [kg/m ³]	2650
Particle radii ranges [m]	0.62×10^{-3} -to- 0.82×10^{-3}
Interparticle friction coefficient	0.5
Normal bonding strength [N/m ²]	2×10^7
Shear bonding strength [N/m ²]	2×10^7

4.3. NUNERICAL RESULTS

Axial deviatoric stress, axial strain, and volumetric strain are monitored during the tests. In addition, particle-scale information is stored for post processing.

4.3.1 Hydrate-free sediments

Stress-strain curves obtained during deviatoric loading for loose and dense hydrate-free specimens ($S_{\text{hyd}}=0\%$) reveal contractive and dilative behaviors that depend on confining stress and porosity, in agreement with typical sediment behavior. The response during deviatoric loading at $\sigma_o'=1\text{MPa}$ is shown in Fig. 4.2 (refer to the trend for $S_{\text{hyd}}=0\%$).

The porosity after isotropic consolidation to 1MPa is $n=0.361$ for the dense sand and $n=0.393$ for loose sand [Note: initial porosities before consolidation are $n=0.402$ and 0.532 respectively]. The dense sand shows higher stiffness and maximum dilation near the peak strength, followed by strain-softening. The void ratio e and the deviatoric stress q reach constant values at large strains, i.e. the critical state. In contrast, the loose sand shows a monotonic contractive response. Porosity and shear strength asymptotically approach critical state conditions.

The critical state line is obtained by running simulations at different values of confining stress σ_o' and initial porosity. The projection of the critical state line on $q-p'$ and $e-p'$ planes is shown in Fig. 4.3 (refer to $S_{\text{hyd}}=0\%$ lines). The critical state parameters

$\lambda=0.103$, $\Gamma=0.959$, $\phi_{cs}=25^\circ$ fall between values for Ottawa 20-30 sand ($\lambda=0.053$, $\Gamma=0.806$, $\phi_{cs}=28^\circ$) and for Ottawa F110 sand ($\lambda=0.077$, $\Gamma=0.937$, $\phi_{cs}=31^\circ$ -data in Santamarina and Cho. 2010).

4.3.2 Distributed hydrate-bearing sediments

Results plotted in Fig. 4.2 and 4.3 (for $\sigma'_o=1\text{MPa}$) show that the presence of distributed hydrate causes higher values of: stiffness (particularly in the loose sand), dilative tendency (specially when $S_{hyd} \geq 20\%$), peak strength, mineral void ratio, and strength at critical state. The peak strength increases nonlinearly with hydrate saturation (Fig. 4.2) and the critical state line shifts to higher shear strengths with increasing hydrate saturation (Fig. 4.3-a). Due to high dilation at low confinement, the Coulomb failure envelope exhibits some cohesive intercept when results are extrapolated to $p'=0$; there is only a minor effect on critical state friction ϕ_{cs} (Fig. 4.3-a).

The critical state $e-p$ projection is markedly affected by hydrate saturation (Fig. 4.3-b). For clarity, we refer here to the “mineral void ratio” calculated as:

$$e = \frac{V_v + V_h}{V_m} \quad (4.1)$$

where V_v is the volume of void, V_h is the hydrate volume, and V_m is the mineral volume.

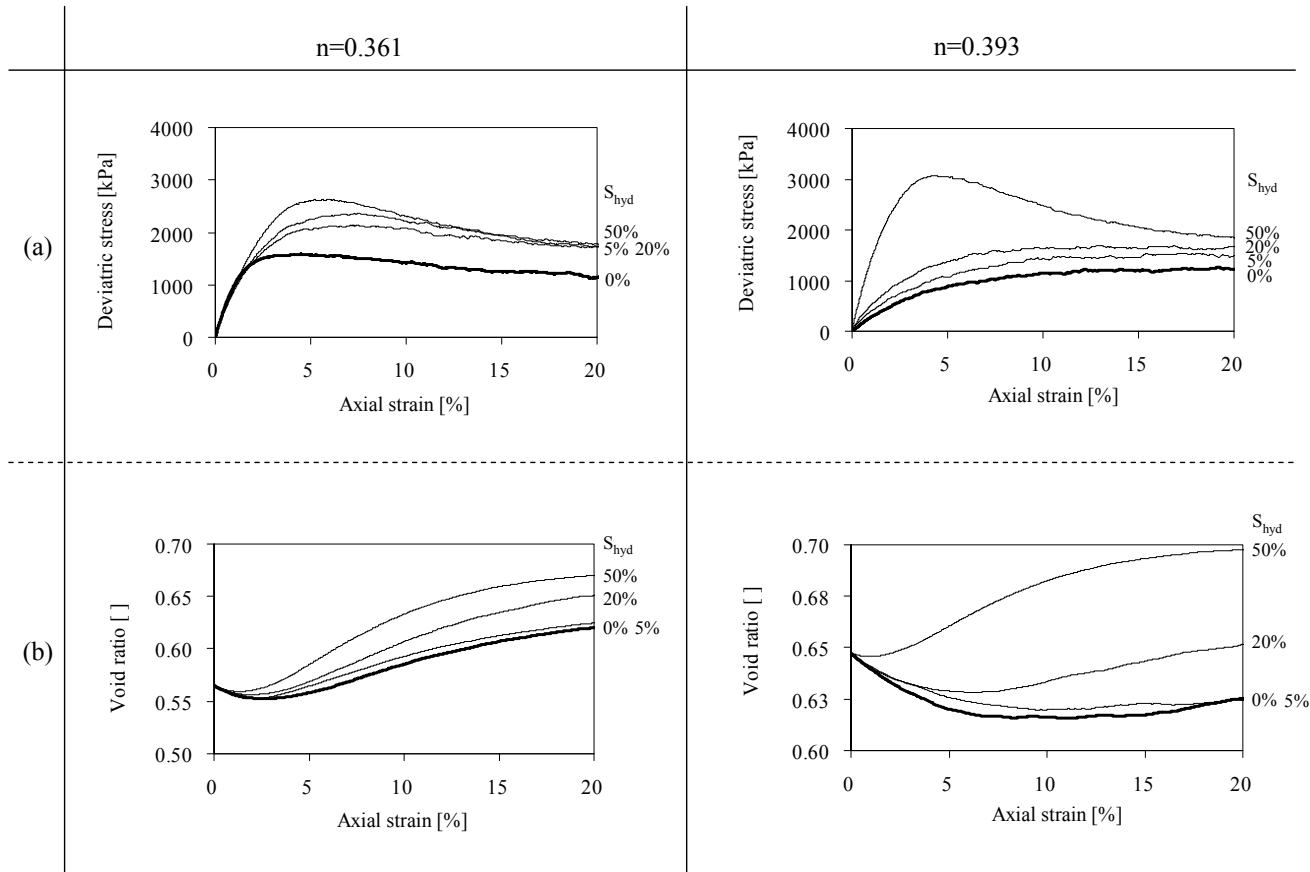


Figure 4.2. Distributed hydrate bearing sediment with hydrate saturation S_{hyd} – Stress, strain, and volume change. (a) Stress-strain response. (b) Volume change. Note: Confining stress= 1MPa.

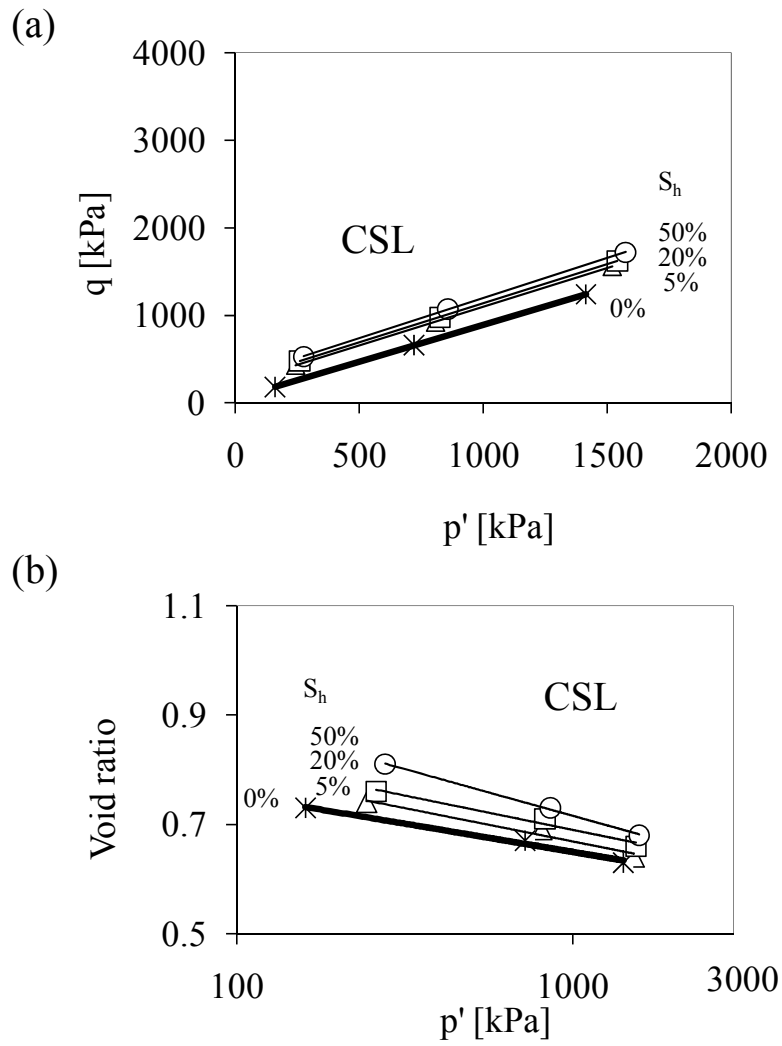


Figure 4.3. Distributed hydrate-bearing sediments - Different hydrate saturation S_{hyd}
 Critical state line projected on (a) q - p' plane, and (b) e - p' plane.

4.3.3 Patchy hydrate saturation

Sediments with patchy hydrate saturation have an apparently similar global stress-strain response to that of evenly distributed hydrate-bearing sediments. However, there are two important differences. First, there is delayed dilation until a strain-level that is comparable to strain at peak dilation in hydrate-free sediments (Fig. 4.4). Second, there is no cohesive intercept in the $p'-q$ projection, instead, there is a significant increase in critical state friction angle, from $\phi_{cs}=25^\circ$ when $S_{hyd}=0$, to $\phi_{cs}=41^\circ$ when $S_{hyd}=50\%$ (Fig. 4.5-a).

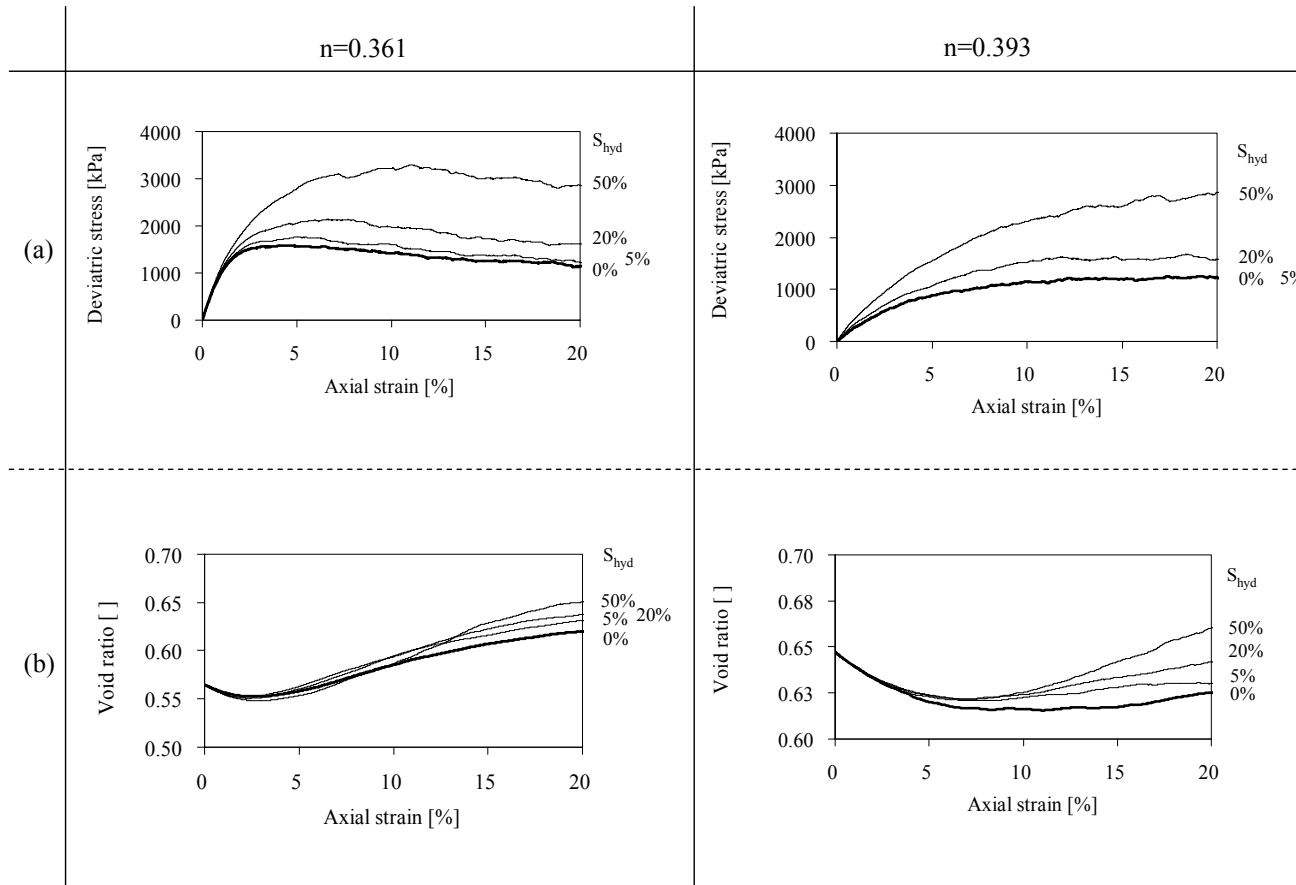


Figure 4.4. Sediment with patchy hydrate saturation (15 clusters). (a) Stress-strain response. (b) Volume change. Note: Confining stress= 1MPa.

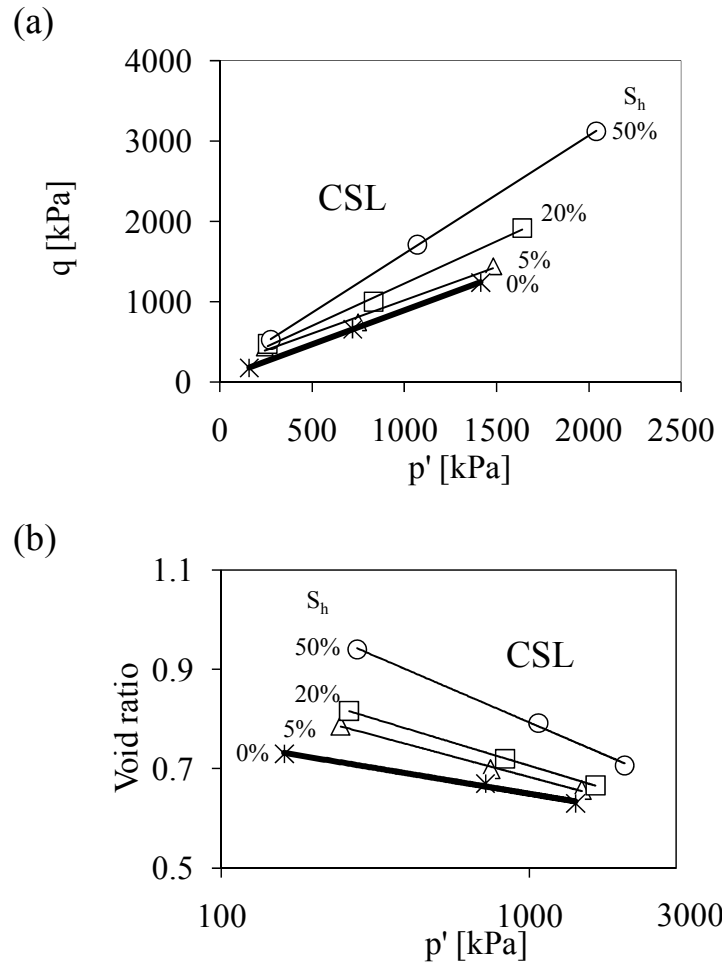


Figure 4.5. Sediment with patchy hydrate saturation (15 clusters): Different hydrate saturation S_{hyd} . Critical state line projected on (a) q - p' plane, and (b) e - p' plane.

4.4. ANALYSES AND DISCUSSIONS

Patchy saturation. The same global hydrate saturation can be obtained using a small number of large clusters or many small clusters. Implications are explored in Figure 4.6 where a medium with $S_{\text{hyd}}=20\%$ is simulated with specimens that contain from 5-to-25 clusters. Results show that, at the same hydrate saturation, a higher number of smaller clusters leads to higher strength and dilative tendency (Note: we anticipate that the position of patches in small specimens has an important effect on the macro-scale response).

Patchy saturation vs. distributed hydrate. Peak strengths obtained using the two different hydrate pore-habits are compared in Fig. 4.7. Results show that peak strengths in distributed hydrate-bearing sediments are higher than in sediments with patchy hydrate saturation. Note that distributed hydrate can be considered the asymptotic condition for the smallest cluster size possible. Therefore, there is inherent agreement between the results in Fig. 4.6 and 4.7.

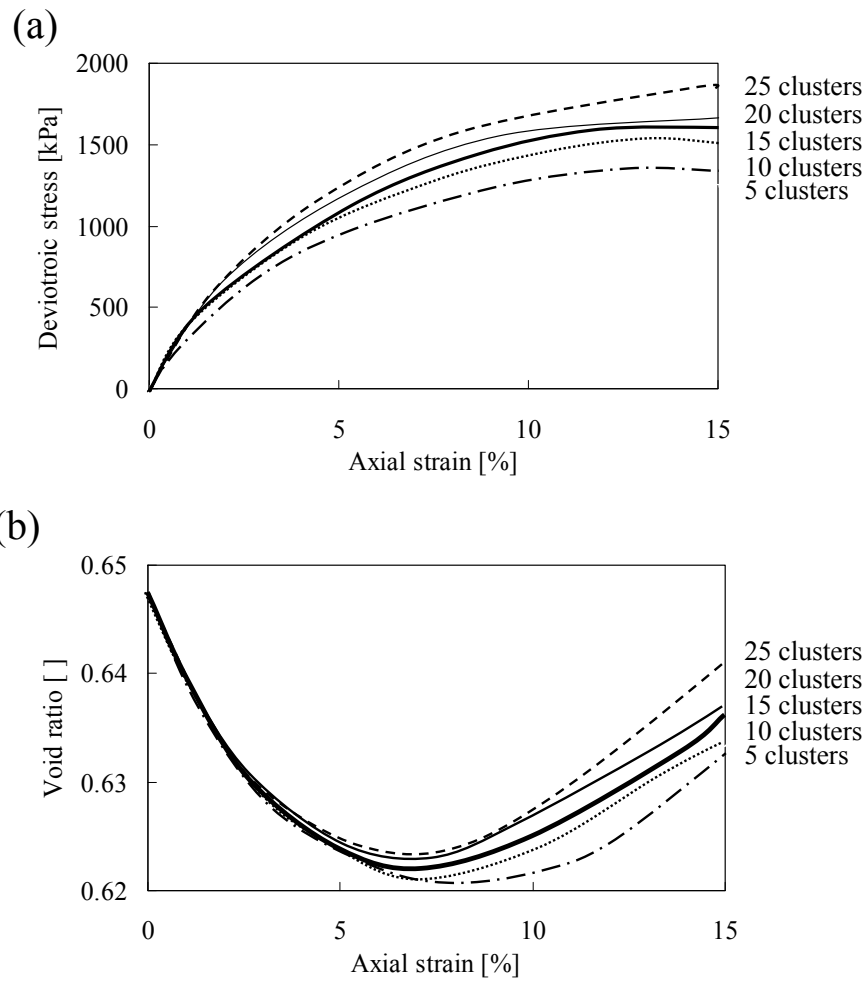


Figure 4.6. Sediment with patchy hydrate saturation- stress, strain, and volume change. The effect of cluster size or number of clusters at the same hydrate saturation $S_h=20\%$. (a) Stress-strain response. (b) Volume change. Note: Confining stress= 1MPa, Initial void porosity=0.393.

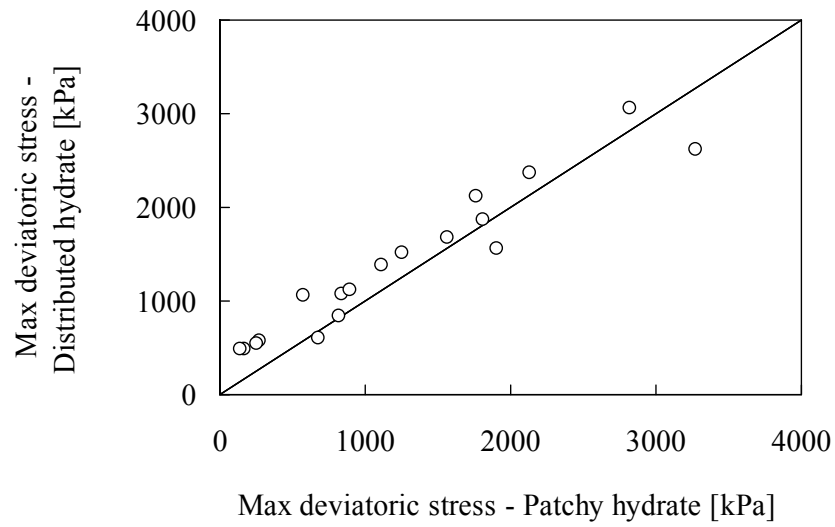


Figure 4.7. Strength comparison between distributed hydrate-bearing sediments and patchy hydrate. The data include results for 2 values of porosity ($n=0.361$ and 0.393), 3 hydrate saturations ($S_{hyd}= 5\%$, 20% , 50%), and 3 confining stress ($\sigma'_d=0.1\text{MPa}$, 0.5MPa , 1MPa).

Strength: Particle level mechanisms. Internal particle-scale information is extracted in terms of normal contact force chains. Selected results shown in Figure 4.8 indicate that load transfer concentrates along stiffer hydrate-filled zones (Fig. 4.8-c and d. Note: these are 2D simulation results to facilitate visualization). Distributed hydrate particles bonded onto mineral surfaces contribute to shear resistance by bonding contiguous particles together and by promoting rotational frustration. The analysis of particle-level forces in specimens with patchy hydrate saturation shows long-range interaction between clusters through the development of load-carrying columns (Fig. 4.8-d). These strong, hydrate saturated patches cause the development of tortuous rather than planar shear planes and higher energy is required to shear the specimen, i.e. higher friction angle.

Comparison of Experimental vs. Numerical Strength values. Numerical results obtained in this study for distributed hydrate-bearing sediments at various hydrate saturations, porosities, and confining stresses are compared against experimental results obtained using cementing and pore-filling hydrate distributions (Fig. 4.9). It can be observed (1) that cementing hydrate lead to greater strength than pore filling hydrate, and (2) that distributed hydrate simulated in this study resembles cementing hydrate formation (Fig. 4.9).

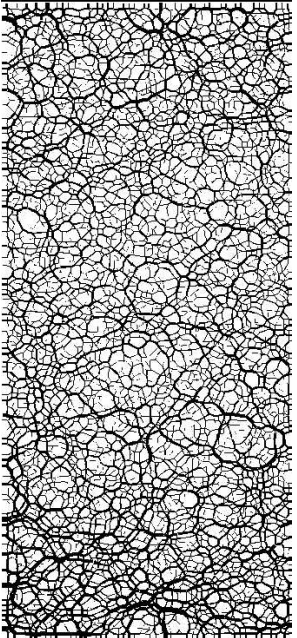
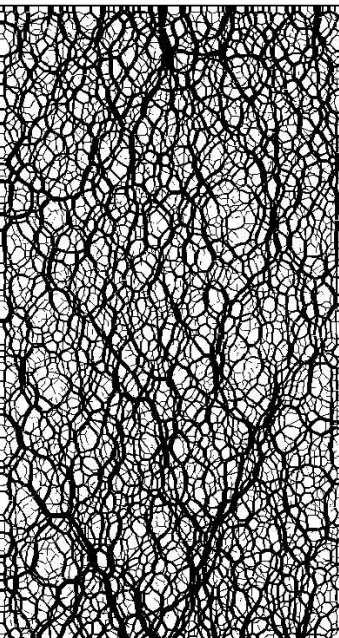
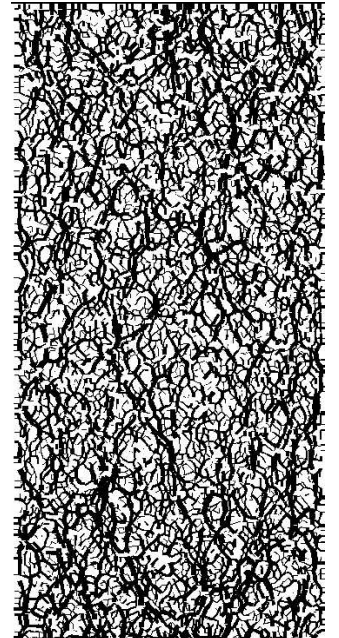
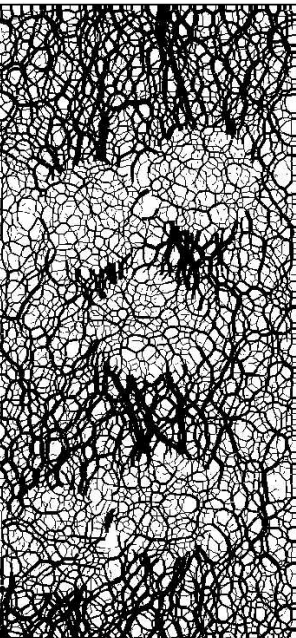
(a) Isotropic load ($\sigma_o=1\text{MPa}$, $\sigma_d=0\text{MPa}$)	Under deviatoric load ($\sigma_o=1\text{MPa}$, $\sigma_d=1.2\text{MPa}$)		
	(b) Hydrate-free sediments	(c) Distributed hydrate ($S_h=20\%$)	(d) Patchy saturated hydrate ($S_h=20\%$)
			

Figure 4.8. Normal contact force chains between soil particles (2D simulations). Images are shown (a) after consolidation to 1MPa of hydrate-free sediments, and after an additional 1.2MPa deviatoric stress is applied to (b) hydrate-free sediments. (c) distributed hydrate-bearing sediments, (d) sediments with patchy hydrate saturation.

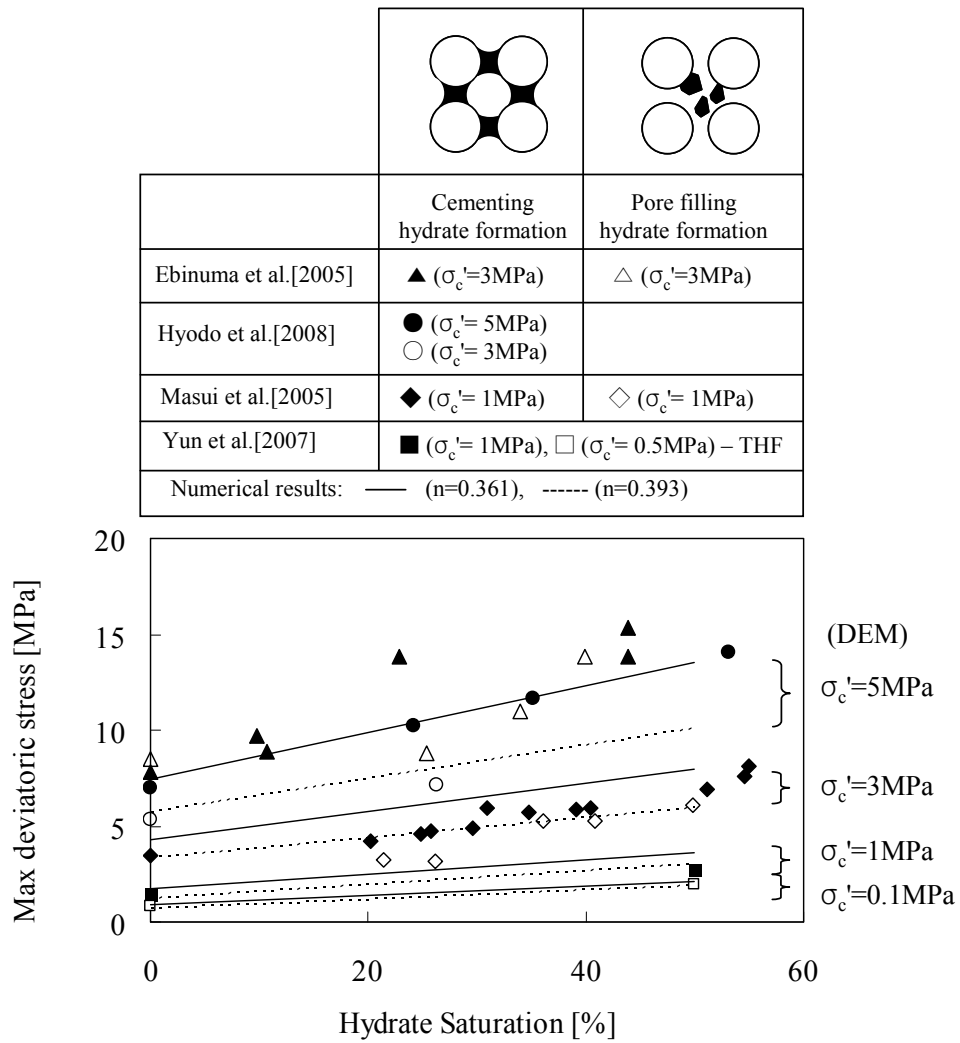


Figure 4.9. Strength of hydrate-bearing sediments - Experimental data and DEM results

Mid-strain Stiffness. The secant modulus E_{50} is determined for all simulations using the strain at half the peak deviatoric stress $\sigma_{dev}^{max}/2$ relative to the origin of the stress-strain curve. Results in Figure 4.10 show that the sediment secant stiffness E_{50} is a function of confining stress σ_o' , hydrate saturation S_h , and initial porosity n . We fitted the numerical results using a modified Hertzian expression,

$$E_{50} = a \left(\frac{\sigma_o'}{1kPa} \right)^b + c E_{hyd} (S_h)^d \quad (4.2)$$

where the fitting parameters represent: “ a ” the hydrate-free sediment stiffness at $\sigma_o'=1kPa$, “ b ” the sensitivity of hydrate-free sediment stiffness to confinement, “ c ” the contribution of the hydrate stiffness $E_{hyd}=8.4GPa$ for a given pore habit, and “ d ” the non-linear effect of hydrate saturation. Factors a and b are extracted from simulations conducted on hydrate-free sediments ($n=0.402$: $a=0.41MPa$, $b=0.69$; $n=0.532$: $a=0.72MPa$, $b=0.50$), while c and d are obtained from simulation results for the various hydrate saturations ($c=0.0001$ -to- 0.0004 , $d=1.1$ -to- 1.2).

Results summarized in Figure 4.10 show that:

- The stress exponent b is greater than the Hertzian $b=1/3$ because these are intermediate strain tests whereby the sediment experiences fabric change.
- The hydrate exponent d is greater than $d=1.0$ to highlight that low hydrate saturation exhibits a diminishing effect on the stiffness of hydrate-bearing

sediments.

- The increase in stiffness with hydrate saturation is more pronounced in sediments with high initial porosity.

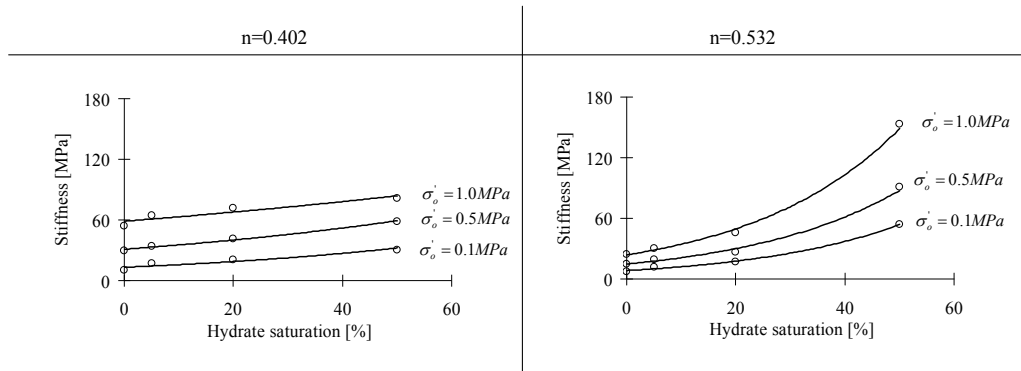


Figure 4.10. Mid-strain stiffness of hydrate-bearing sediments (distributed hydrate) as a function of hydrate saturation and effective stress.

Hydrate dissociation. The implications of hydrate dissociation are investigated under the following end-member reservoir boundary conditions: (1) constant stress boundary CS , (2) zero strain boundary ZS , and (3) constant vertical stress but zero lateral strain K_o condition. The specimen with distributed hydrate $S_{hyd}=20\%$ is subjected to a gradual decrease in hydrate particle size. We repeat the study at low and high deviatoric stresses.

Results in Figure 4.11 show that the stress-strain response in sediments during hydrate dissociation depends on reservoir boundary conditions and the level of deviatoric stress.

In particular:

(1) hydrate dissociation in a low deviatoric stress-state induces contraction without failure under constant stress boundary CS (Note that the deviatoric stress when hydrate dissociates is lower than the maximum deviatoric stress the hydrate-free sediments can withstand). Conversely, the sediment fails during dissociation when the deviatoric stress is higher than the strength of the hydrate-free sediment (See analogous experimental results in Hyodo, et al. 2008);

(2) vertical and lateral stresses dramatically decrease during hydrate dissociation under zero strain boundary conditions ZS . In this case, an overlying rigid caprock stratum could fail in bending;

(3) vertical K_o consolidation occurs during hydrate dissociation under a constant vertical

stress and zero lateral strain boundary conditions (See also Lee, et al. 2010). While the sediment does not approach failure, overlying rigid layers will experience bending effects.

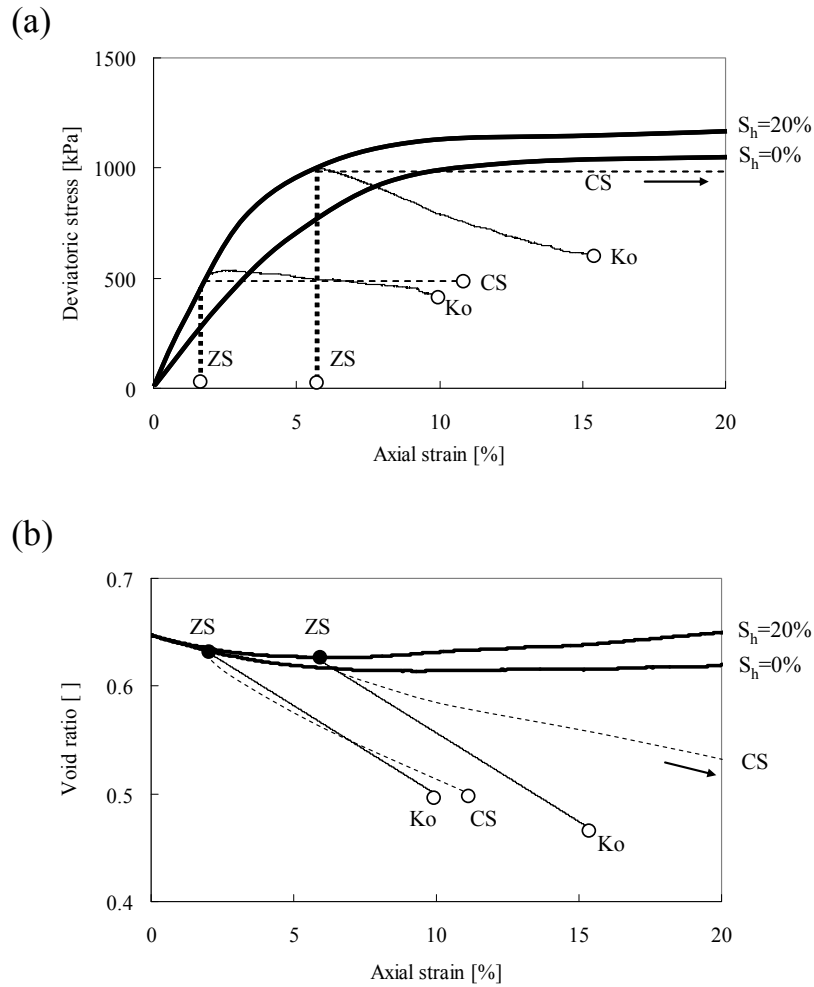


Figure 4.11. Hydrate dissociation under different reservoir boundary conditions: (a) constant stress boundary CS, (b) zero strain boundary ZS, or (c) constant vertical stress but zero lateral strain K_o condition.

4.5. CONCLUSIONS

Numerical DEM simulations provide unique insight into the mechanical response of hydrate-bearing sediments. The hydrate mass can be simulated as either small randomly “distributed hydrate” or as “patchy saturation” whereby clusters with 100% hydrate saturation are distributed within a hydrate-free sediment.

Simulation results obtained for both hydrate-bearing sediments reveal that increasing either the initial sediment density or the degree of hydrate saturation causes an increase in stiffness, strength and dilative tendency. The combined effects on strength and dilation produce a shift in the critical state line toward higher void ratios and higher $p'-q$ values.

The strength of sediments with patchy hydrate saturation is slightly lower than the strength of evenly distributed hydrate-bearing sediments.

Distributed hydrate-bearing sediments exhibit high dilation at low confinement and a cohesive intercept is obtained when the Coulomb failure envelope is extrapolated to the origin. Yet, hydrate content has almost no effect on critical state friction ϕ_{cs} .

Sediments with patchy hydrate saturation exhibit delayed dilation until a strain-level that is comparable to the strain at peak dilation in hydrate-free sediments. There is a significant increase in critical state friction angle and there is no cohesive intercept in

the p' - q projection.

Internal particle-scale analyses using normal contact force chains provide unique insight into the different stress response of both hydrate-bearing sediments. Load transfer concentrates along stiffer hydrate-filled regions. Hydrate particles bonded onto the mineral surface contribute to increased shear resistance by contiguous particles being bonded together, and by promoting rotational frustration. The strong, hydrate-saturated patches force the development of tortuous rather than planar shear planes and higher energy is required to shear the specimen, i.e. higher friction angle.

The stiffness of hydrate-bearing sediments is a function of hydrate saturation S_h , initial porosity n and the effective stress σ'_o .

Hydrate dissociation under different reservoir boundary conditions leads to volume contraction and/or stress relaxation. Pronounced shear strains develop if the hydrate-bearing sediment is subjected to deviatoric loading during dissociation.

CHAPTER V

EMERGENT PHENOMENA IN GAS PRODUCTION FROM HYDRATE-BEARING SEDIMENTS

5.1. INTRODUCTION

Gas production from hydrate-bearing sediments causes fluid volume expansion, gas and water flow, temperature decrease due to endothermic hydrate dissociation, and changes in porosity and effective stress. Other phenomena may develop as well, including fines migration and clogging (Kampel et al. 2008; Valdes and Santamarina 2008), sand production (Papamichos et al. 2001), ice and secondary hydrate formation near production wells (Moridis and Reagan 2007), grain crushing (Guimaraes et al. 2007), and gas-driven fractures in sediments (Santamarina and Jang 2009; Shin and Santamarina 2010). These phenomena may cause sediment instability and other unwanted problems such as formation clogging, bore hole failure, retardation of gas production, and low gas recovery efficiency.

Several numerical simulators can be used to analyze the gas production process during hydrate dissociation (Ahmadi et al. 2004; Garg et al. 2008; Kwon et al. 2008; Moridis and Sloan 2007; Rutqvist et al. 2009; Wilder et al. 2008). Small-scale laboratory experiments here focused on the effect of pressure, temperature and inhibitor on the hydrate dissociation rate and the cumulative amount of produced gas (Kawamura et al.

2009; Kono, H.O. et al. 2002; Linga et al. 2009a; Linga et al. 2009b; Oyama et al. 2009; Tang et al. 2005). However, large-scale laboratory experiments of gas production from hydrate-bearing sediments are needed to identify potential emergent phenomena that may hinder (or help) gas production. Yet, large scale testing is particularly challenging in the study of hydrate-bearing sediments because of the high pressure needed to attain stability conditions, the need for concurrent effective stress control and ensuing safety considerations.

In this study, we use the large-scale Seafloor Process Simulator SPS of the Oak Ridge National Laboratory (Phelps et al. 2001). The test sequence is designed to explore production related phenomena that would not be observed in smaller cells and typical experimental designs. The pressure vessel and the instrumented chamber are described next.

5.2. EXPERIMENTAL STUDY

5.2.1. Devices

Seafloor Process Simulator SPS. This 72-L vessel is constructed from corrosion resistant Hastelloy (Fig. 5.1-a). The simulator has a maximum 21-MPa working pressure, and 41 ports for instrumentation. It is housed inside of a cold room with a working temperature range from -2 to 20°C.

Instrumented soil chamber. A stainless steel soil chamber is placed inside the SPS (Fig. 5.1). The fixed bottom plate has a water injection port. The top plate has several holes for free-gas and water flow and can move up and down depending on the sediment volume change. A perforated plate and a spring ($k=306\text{N/cm}$) are located on the top plate in order to apply a pre-determined effective stress on the sediment while maintaining zero-lateral strain conditions (Note: 100 kPa is used in this study).

Instrumentation. The sediment vertical displacement during hydrate formation and gas production is measured using a linear variable differential transformer LVDT that rests on the top plate of the internal soil chamber (Fig.5.1-b). Three bender elements pairs are located at different heights in the sediment (Fig. 5.1-b). The source bender elements in each pair are connected to a signal generator which sends a step function signal every 20 ms; the receiver bender elements are connected to a pre-amplifier and a digital storage oscilloscope. Three thermocouples are buried in the sediment at the same heights as the three pairs of bender elements. A fourth thermocouple is located inside the water injection port of the internal chamber, and a fifth thermocouple is located inside the SPS to measure the gas temperature. A pressure transducer is attached to the SPS to measure gas pressure, and second one is connected to the water injection port on the bottom plate of the internal soil chamber. A data logger records all pressures and temperatures and the vertical displacement every four seconds.

Sediments. Clean Ottawa 20/30 sand is used for the first two tests (Tests #1 and #2), and it is placed in the soil chamber with an initial porosity $n=0.4$. A mixture of Ottawa

80/140 sand and kaolinite clay is used for the next two tests with initial porosity $n=0.35$ in both cases (Tests #3 and #4); the initial water saturation is $S_w=0.5$ for Test #3 and 0.65 for Test #4.

5.2.2. Test Procedure

There are four main stages: (1) specimen preparation, (2) hydrate formation, (3) water injection and drainage, and (4) hydrate dissociation. Details for each stage follow.

Specimen preparation. The instrumented soil chamber is prepared first by filling it with the selected sediment while placing the instrumentation at the corresponding elevations. Then, the vertical effective stress is applied using the spring-based loading system. Finally, the chamber is lowered into the SPS where all fluid and electrical connections are established. Table 1 summarizes sediment conditions. Clean Ottawa 20/30 sand is placed dry in Test #1 and #2. Then, a water table is imposed to ~6 cm from the bottom (see Table 1). In test #3 and #4, kaolinite is saturated with water to form a fluid paste that homogeneously mixed with Ottawa 80/140 and no initial water table is imposed. The sediment is densified by rodding in all tests ($n=0.35$ -to- 0.4).

Hydrate formation. The cold room that houses the SPS is maintained at $\sim 4^\circ\text{C}$. The SPS is pressurized with CO_2 to $\sim 3.4\text{MP}$ and the system is kept at constant pressure-temperature conditions, inside the CO_2 hydrate stability field, overnight.

Water injection and drainage. Water is injected into the gas-rich sediment at an injection rate of 8ml/min through the port in the bottom plate. The water is then quickly drained through the same port used for injection. Various injection and drainage cycles are used in the different tests (refer to Table 1 for details).

Hydrate dissociation. Hydrate is dissociated via depressurization. First, the SPS pressure is lowered to reach a value near the hydrate phase boundary. Then, depressurization continues either through the SPS pressure port so that the sediment loses pressure from the top plate (slow depressurization for Tests #1 and #2, and fast depressurization for Test #3), or through the bottom fluid port in the internal chamber (Test #4).

Table 5.1. Summary of test condition and procedure

	Measurements	Soil Type/condition	Procedure
Test 1	Pressure (1) Temperature (4) S-wave (2 pairs)	Ottawa 20/30 sand Porosity $n=0.4$ Dry soil 6 cm water table	Set-up the chamber Pressurize chamber and lower T^* First water injection and drainage Second water injection Depressurize SPS
Test 2	Pressure (2) Temperature (4) S-wave (2 pairs) Surface settlement	Ottawa 20/30 sand Porosity $n=0.4$ Dry soil 7 cm water table	Set-up the chamber Pressurize chamber and lower T^* First water injection and drainage Second water injection Depressurize SPS
Test 3	Pressure (2) Temperature (6) S-wave (3 pairs) Surface settlement	95% Ottawa 80/140 sand + 5% Kaolinite Porosity $n=0.35$ Initial water saturation $S_w=0.5$	Set-up the chamber Pressurize chamber and lower T^* First water injection and drainage Second water injection and drainage Third water injection and drainage Depressurize SPS through the top plate
Test 4	Pressure (2) Temperature (6) S-wave (3 pairs) Surface settlement	95% Ottawa 80/140 sand + 5% Kaolinite Porosity $n=0.35$ Initial water saturation $S_w=0.65$	Set-up the chamber Pressurize chamber and lower T^* First water injection and drainage Second injection using salt water-drainage Depressurize SPS through the bottom port

Note: * operating environmental conditions are $P \sim 3.4$ MPa, $T = \sim 4^\circ\text{C}$

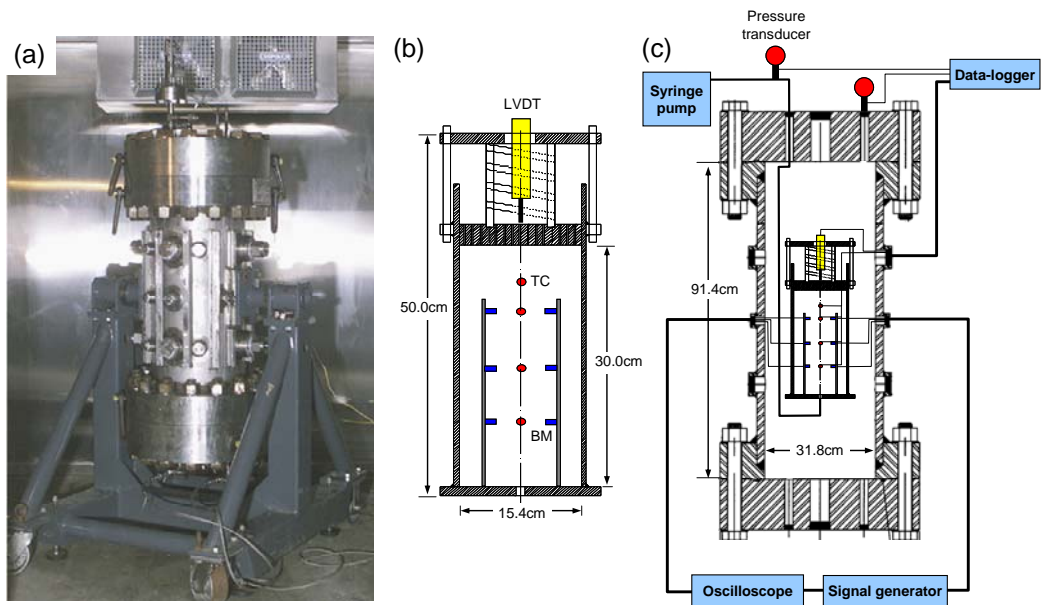


Figure 5.1. Devices and instrumentation. (a) Seafloor Process Simulator. (b) Internal instrumented soil cell; LVDT for sediment displacement measurements, bender element BM for S-wave velocity measurements, thermocouples TC for temperature measurements, and pressure transducers for pressure measurements. (c) Complete system including peripheral electronics.

5.3. EXPERIMENTAL RESULTS

Multi-stage P-T histories and corresponding changes in S-wave velocity are obtained during the tests.

Hydrate formation. There is no evidence of any hydrate formation in the dry sediment with the low water level in Tests #1 and #2 during the first ~14 hrs within stability P-T conditions. However, the partially water saturated sediments in Test #3 and #4 spontaneously started to form hydrates approximately 1 hour after the P-T conditions in the sediment moved inside the CO₂ hydrate stability field (Fig. 5.2-a). Hydrate formation caused the S-wave velocity and temperature to increase and the pressure to decrease. The internal thermocouples show that the reaction lasts for more than ~8 hrs particularly at the center of the specimen (Fig. 5.2-a).

Water injection in a gas-filled hydrate-free sediment. The first water injection caused hydrate formation in the sediment without fines as denoted by the temperature change. Injection lasted 3.5 hours and the water front moved up at a rate of 76 mm/hr in agreement with the timing of temperature peaks (Test #2 – Fig. 5.2-b). The S-wave velocity increased where hydrate formed (Fig. 5.3). A second injected gas-free water dissolved hydrate near the entry port and the temperature decreased (Fig. 5.2-c). The S-wave velocity decreased where hydrate dissolved and increased where hydrate formed (Fig. 5.3).

Water drainage. Trapped gas reacts and forms hydrate when water drainage is allowed as shown in Fig. 5.2-d. Furthermore, the invading gas phase reacts with any free water left behind after drainage. In this case, water was drained in 20 min while the reaction continued for ~3 hrs (Fig. 5.2-d). Note that cooling accompanies depressurization near the drainage port (response #4).

Hydrate dissociation. The sediment temperature decreases following the fast depressurization (from an initial pressure near the CO₂ hydrate phase boundary - Fig. 5.2-e- Test #3). Free water formed ice as indicated by the constant temperature of 0°C. The measured data show that there is vertical volume expansion caused by ice formation and concurrent gas production.

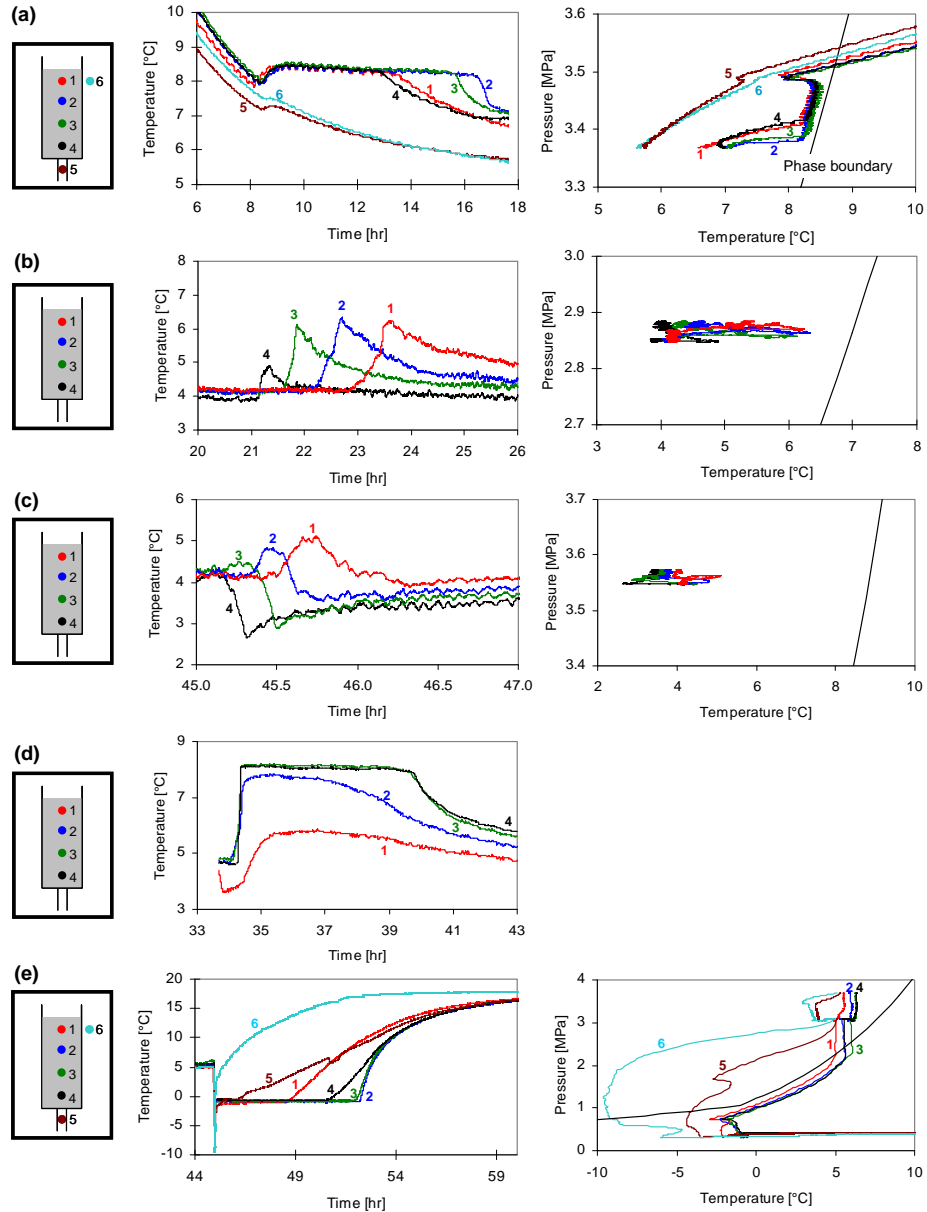


Figure 5.2. Pressure and temperature histories during hydrate formation. (a) Spontaneous hydrate formation in a gas-filled sand-clay mixture with initial water saturation $S_w = 50\%$ (Test #3). (b) Hydrate formation in initially dry gas-filled sand triggered by water injection (Test #2). (c) Hydrate formation and dissolution during deaired-water injection in gas-filled sand that had some initial hydrate saturation (Test #2). (d) Hydrate formation in a water saturated sand triggered by water drainage (Test #1). (e) Hydrate dissociation by depressurization (final stage in Test #3).

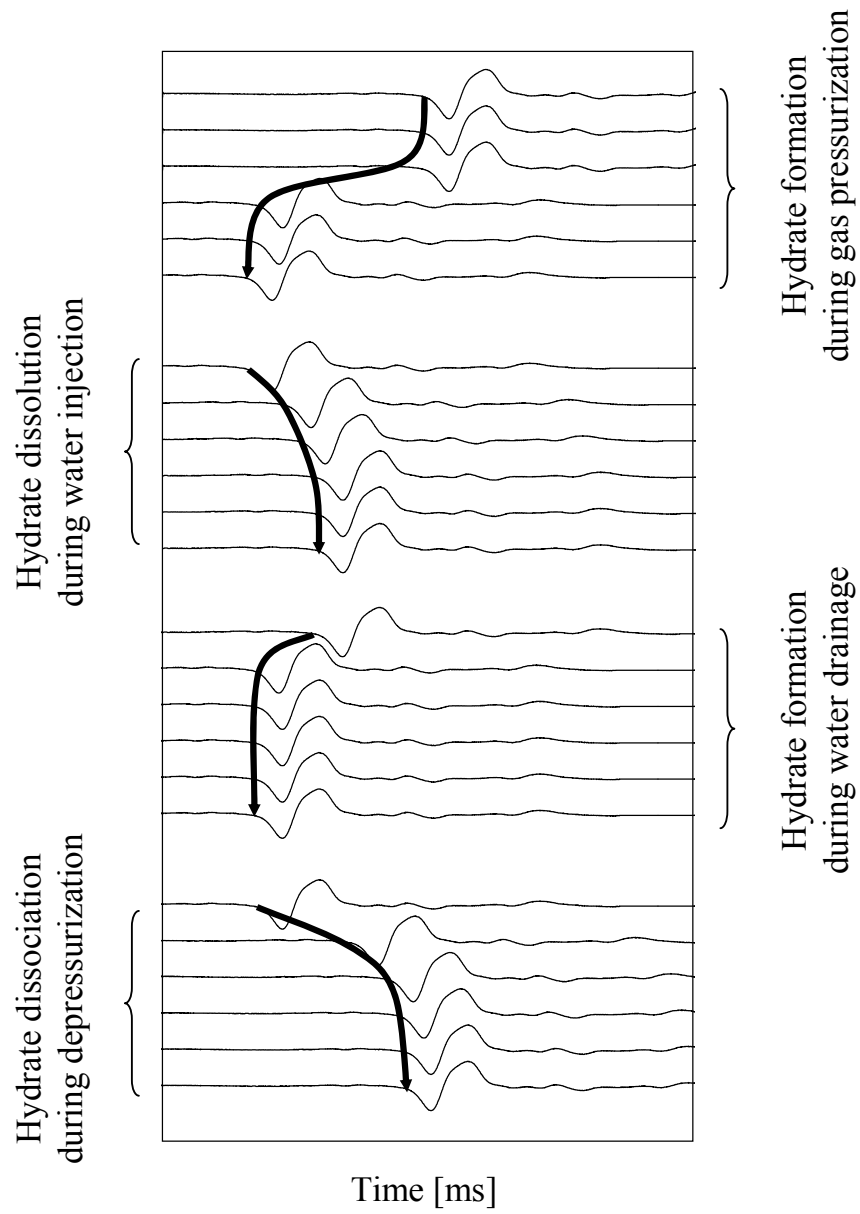


Figure 5.3. S-wave velocity changes during hydrate formation, dissolution, and dissociation (Test #3).

5.4. ANALYSES AND DISCUSSION

5.4.1 Hydrate dissolution

Water-gas mixture inside the thermodynamic hydrate-stability field may form hydrate after a long induction time in quiescent conditions, or rapidly if the sediment is subjected to a triggering mechanism such as agitation, mechanical shock, and shear (Mullin 2001).

The injection of gas-free water in hydrate-bearing sediments induces hydrate dissolution, as indicated by the temperature drop near the injection port in Fig. 5.2-d (trace 4). The amount of hydrate that will dissolve in a pore volume of gas-free water can be estimated from the mass balance of gas in the system as a function of water density $\rho_{water}=1 \text{ g/cm}^3$, hydrate density ρ_{hyd} , gas solubility in water C_{gas}^w , gas molar concentration in hydrate C_{gas}^{hyd} , and the water saturation S_w (Note: the amount of water from hydrate dissociation is assumed small compared to the pore volume),

$$\Delta S_h = \frac{C_{gas}^w}{C_{gas}^{hyd}} \frac{\rho_w}{\rho_{hyd}} S_w \quad \text{per pore volume} \quad (5.1)$$

For CO₂ hydrate $\rho_{hyd} \approx 1.11 \text{ g/cm}^3$, $C_{CO_2}^w = 0.89 \text{ mol/kg}$, $C_{CO_2}^{hyd} = 6.58 \text{ mol/kg}$ at P=3MPa and T=273K (Aya et al. 1997; West et al. 2003), equation 5.1 becomes,

$$\Delta S_h \approx 0.12 S_w \quad \text{for CO}_2 \text{ hydrate} \quad (5.2)$$

For CH₄ hydrate $\rho_{hyd} \approx 0.94 \text{ g/cm}^3$, $C_{CH_4}^w = 0.06 \text{ mol/kg}$, $C_{CH_4}^{hyd} = 8.20 \text{ mol/kg}$ at $P=3\text{MPa}$ and $T=273\text{K}$, equation 5.1 anticipates,

$$\Delta S_h \approx 0.008 S_w \quad \text{for CH}_4 \text{ hydrate} \quad (5.3)$$

In other words, this is the change in hydrate saturation for each pore volume of gas-free water that is replaced during injection (allowing for equilibration).

5.4.2 Fines migration

The specimen was dissected layer-by-layer at the end of each test and sieve analyses were obtained. Fines migrated toward the top of the sediment column when gas depressurization occurred through the top plate (e.g. Test #3, Fig. 5.4-a) However, fines migrated towards the lower part of the sediment column when gas depressurization occurred through the bottom port of the chamber (e.g. Test #4, Fig. 5.4-b).

Migrating fines can clog the sediment near the well bore. Fines migration and clogging depend on geometric constraints, such as the relative size of the migratory fines with respect to the pore throat size distribution in the host sediment skeleton. A particle with diameter d can migrate when $D/d > 2.4$ (simple cubic) to $D/d > 6.4$ (cubic tetrahedral) through a granular packing of particle size D . However, bridges of 3 to 5 migrating particles can form at pore throats and clog the sediment in high flow velocity requires when $D/d = 2.4\text{-to-}12$ for simple cubic packing and when $D/d = 6.5\text{-to-}32.5$ for a

tetrahedral packing (Valdes and Santamarina 2008). The particle diameter D of Ottawa 80/140 sand is ~ 0.105 mm and the particle diameter d of kaolinite is 4.5-to-6.0 μm . Given that $D/d \sim 20$, kaolin particles can migrate as well as clog the sediment. Data in Figure 5.4 confirms that small particles migrated during gas production.

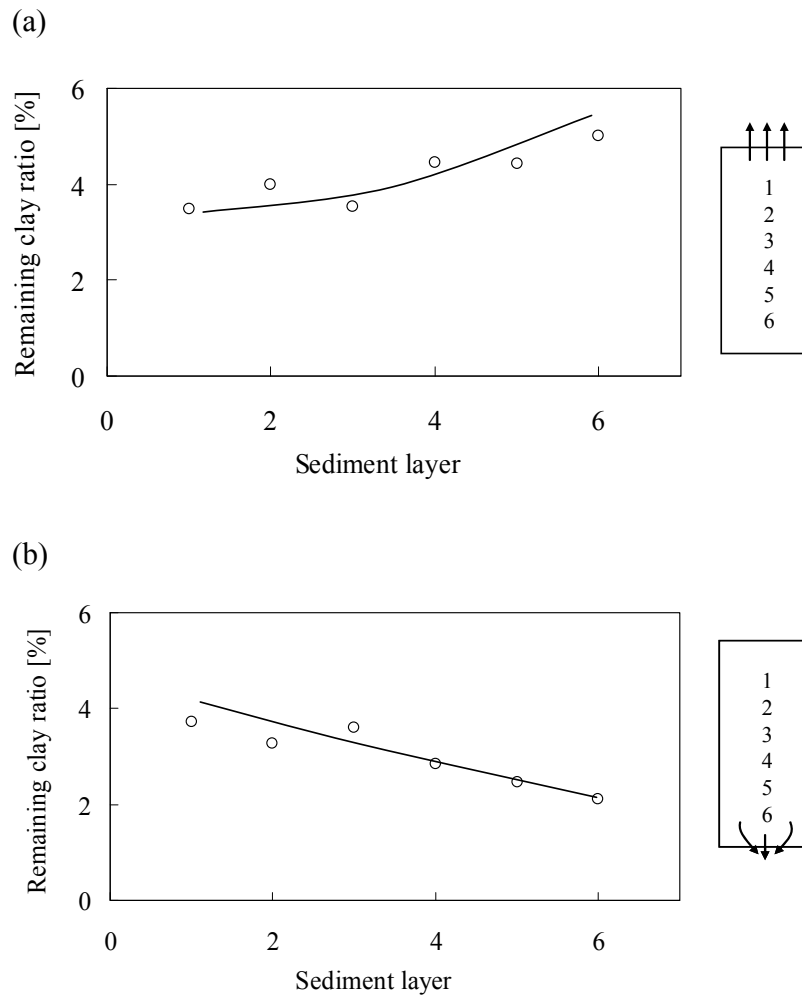


Figure 5.4. Fines migration during hydrate dissociation. (a) Fines migration during upwards flow (Test #3), and (b) Fines migration due to drainage through the bottom plate port (Test #4).

5.4.3 Vuggy structure formation – Gas driven fractures

Let's consider a growing gas bubble in saturated sandy sediment with clayey fines (Fig. 5.6). The fine particles that are not part of the load-carrying granular skeleton move along with the interface of the expanding bubble surface. The bubble can grow without displacing the skeletal sand particles when the fines content on the bubble surface is low (Fig. 5.6-b). If the mass of fines per unit surface area of the bubble is high enough to clog pore throats in the sand, then the expanding gas bubble will locally push away the skeletal sand particles as long as the pressure of the gas bubble can create a sufficiently high force against the boundary sand grains (Fig. 5.6-c). This sequence of events explains the vuggy structure observed after depressurization in Test # 3 (Fig. 5.6-d).

Continued gas expansion can lead to gas driven fractures as observed in Fig. 5.7 (Test #3). Together, these results suggest that the probability of fracture formation will increase if fines are present in otherwise sandy sediments.

5.4.4 Shear wave velocity

The shear wave velocity of hydrate-free sediment is determined by the effective stresses in the direction of wave propagation σ_{\parallel}' and particle motion σ_{\perp}' . Once hydrate grows in the sediment, the shear wave velocity of hydrate-bearing sediments V_{s-hbs} increases with hydrate saturation S_{hyd} (Santamarina and Ruppel 2008),

$$V_{s-hbs}^2 = \alpha \left(\frac{\sigma_{\parallel}' + \sigma_{\perp}'}{2kPa} \right)^{\beta} + \left(\frac{V_h S_h^2}{n} \right)^2 \theta \quad (5.4)$$

where V_h is the shear wave velocity of pure hydrate the factor θ captures the hydrate pore-habit (e.g., cementing or pore filling); parameters α and β can be extracted from tests conducted on sediments without hydrate. This expression can be used to analyze geophysical data, such as the time series presented in Fig. 5.3.

Figure 5.5 shows the variation of S-wave velocity versus hydrate saturation, for different effective stress levels. Parameters $\alpha = 80$ m/s, $\beta = 0.25$ are selected for sand (from Santamarina et al., 2001), $V_h = 1963.6$ m/s – from Sloan and Koh, 2008, and $\theta = 0.2$ is obtained using S-wave velocity $V_s = 588$ m/s measured at $S_h = 48\%$ in Test #3. Using this plot we can estimate the hydrate saturation during experiments from the measured S-wave velocities. For example, consider Test # 3: the hydrate saturation after initial hydrate formation is $S_h = 50\%$, dissolution near the entry port causes a drop in hydrate saturation to $S_h = 16\%$ and hydrate re-grows after drainage and gas invasion to reach $S_h = 27\%$ (Fig. 5.5).

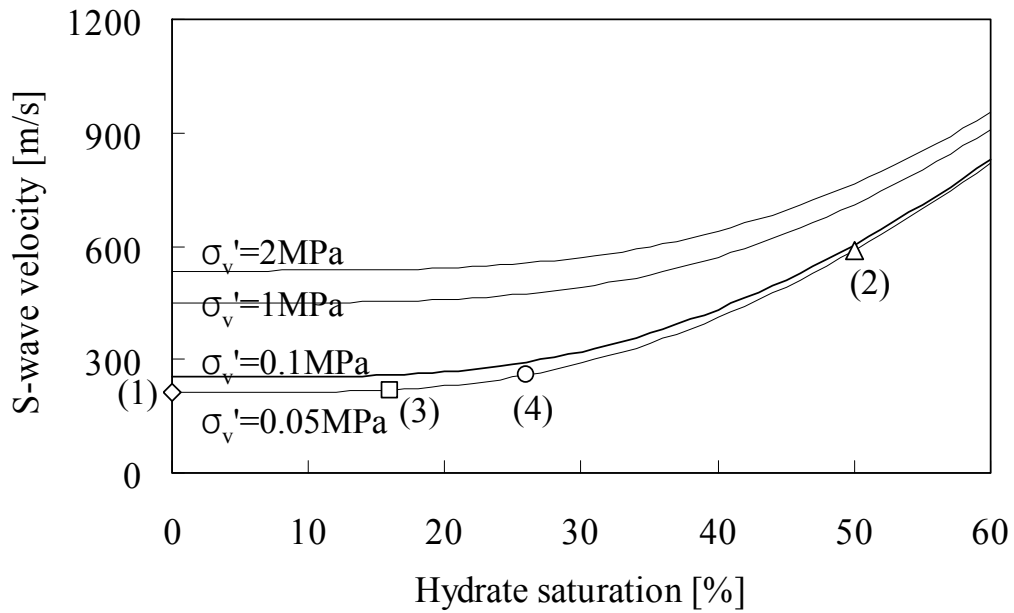


Figure 5.5. Shear wave velocity in hydrate-bearing sediments. Trends shown for sands (Eq. 3). Experimental results correspond to Test #3: (1) \diamond No hydrate – before hydrate formation or after hydrate dissociation. (2) Δ After initial hydrate formation. (3) \square Drop due to hydrate dissolution after gas-free water injection. (4) \circ Hydrate regrowth after water drainage and gas invasion.

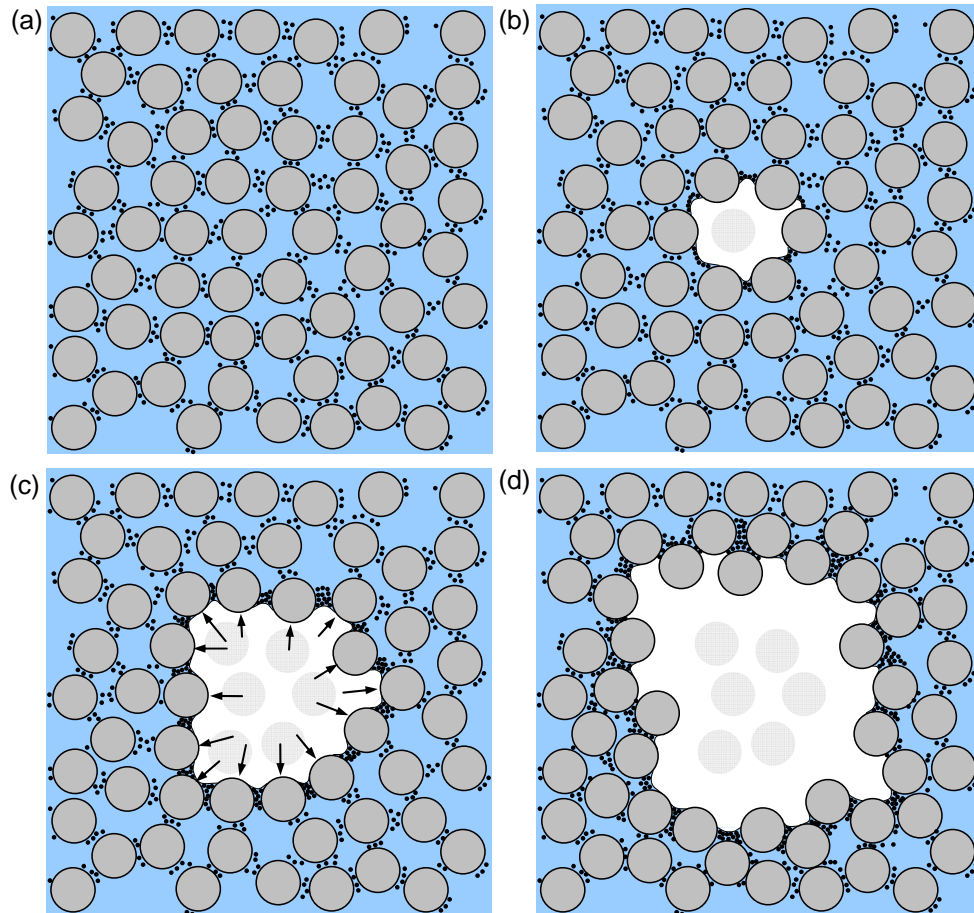


Figure 5.6. Vuggy structure formation due to local clogging and particle displacement during gas bubble expansion. (a) Distributed fines in a water saturated sediment. (b) Gas bubble nucleation during depressurization. Fines move with the gas-water interface as the gas bubble grows. (c) High fines concentration clogs pore throats. (d) Further gas bubble growth can push sand particles away. The resulting vuggs are precursors to gas-driven fracture formation.

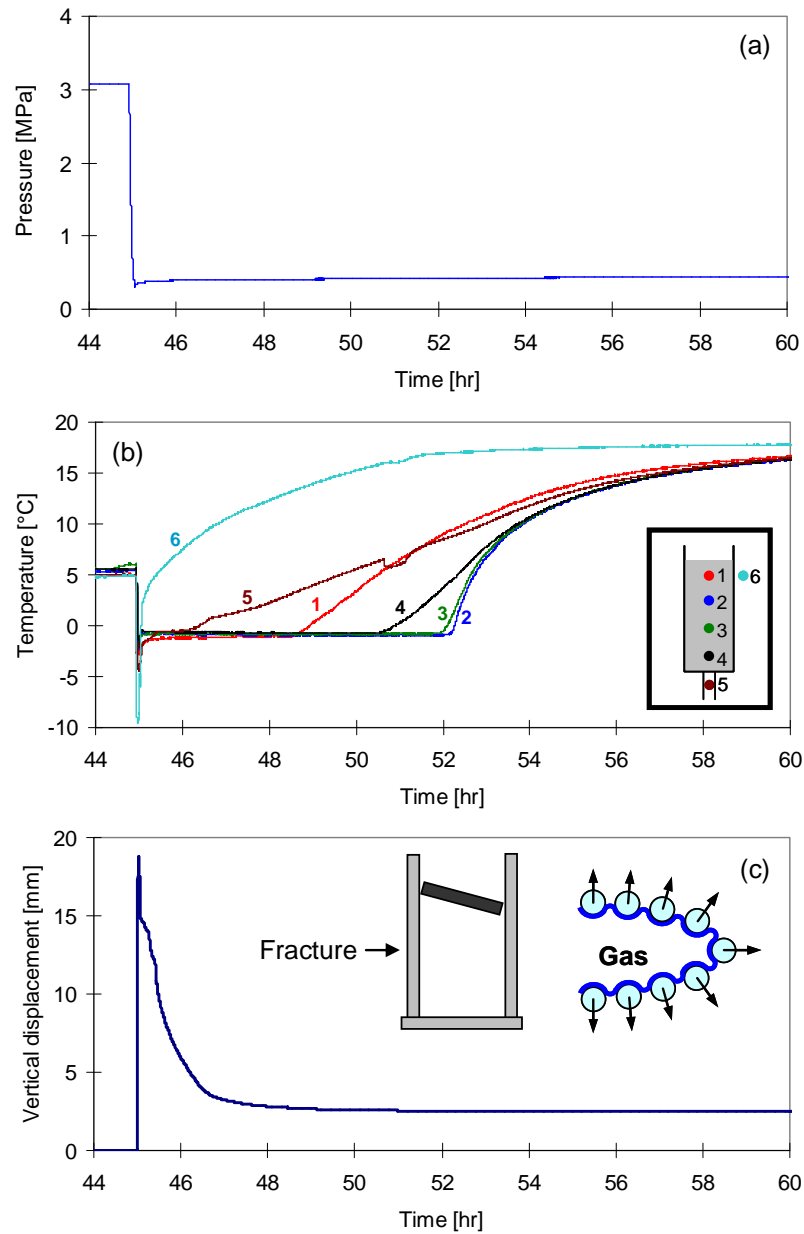


Figure 5.7. Total stress, effective stress and gas driven fracture. (a) Hydrates are dissociated by depressurization. i.e., decrease in the boundary total stress. (b) Rapid depressurization induces ice formation concurrent with hydrate dissociation. (c) Gas expansion creates hydraulic fracture that facilitates gas evacuation.

5.5. CONCLUSIONS

The induction time for hydrate formation can be long in quiescent systems. Water injection into water-limited sediments triggers hydrate nucleation.

The advection of gas-free water into hydrate-bearing sediments dissolves hydrate. The change in hydrate saturation ΔS_h for each pore volume of replace water can be estimated as a function of the water saturation S_w . It is $\Delta S_h \approx 0.12 S_w$ in CO_2 hydrate and $\Delta S_h \approx 0.008 S_w$ in CH_4 hydrate.

The evolution of the shear wave velocity provides insightful information related to the sediment stress-hydrate history. If properly calibrated, the hydrate saturation can be obtained with the measured S-wave velocities using semi-empirical relationships that account for effective stress, porosity and hydrate pore habit.

The migration of fine particles that are not part of load-carrying granular skeleton depends on geometric constraints such as the relative size of the migratory fines with respect to the size of pore throats in the sediment. When the geometric conditions are satisfied, gas production in hydrate-bearing sediments containing fines can induce fines migration and lead to clogging.

A gas bubble growing in saturated sediment experiences an increase in fines content on the bubble surface. Eventually, the fines content per unit surface area of the bubble can

be high enough to clog pore throats. Then, the expanding gas bubble may push away the skeletal particles, creating a vuggy structure. Vugs are precursors to gas-driven fracture formation. Thus, the presence of fines in otherwise clean sands hinders gas recovery and may lead to gas-driven fracture formation.

CHAPTER VI

CH₄-CO₂ REPLACEMENT IN HYDRATE-BEARING SEDIMENTS: A PORE-SCALE STUDY

6.1. INTRODUCTION

Worldwide carbon reserves in the form of CH₄ hydrate are on the order of 500-to-10,000 Gt (Collett 2002; Kvenvolden 1988; Milkov 2004; Ruppel and Pohlman 2008). The injection of CO₂ into CH₄ hydrate-bearing sediments has the advantage of liberating CH₄ while simultaneously sequestering CO₂ leading to the more sustainable use of a fossil fuel (McGrail et al. 2007; Ota et al. 2005a; Stevens et al. 2008; Svandal et al. 2006; Zhou et al. 2008a).

The extent of the CH₄-CO₂ replacement is affected by multiple factors and coexisting processes, such as pressure- and temperature-dependent relative viscosity, permeability, density and solubility among water, CH₄ and CO₂ (Jung et al. 2010). Previous studies have observed no apparent dissociation during replacement (Jung et al. 2010), and have monitored replacement ratios and rates which show that the CH₄-CO₂ replacement rate increases near the CH₄ hydrate phase boundary and with increasing CO₂ gas pressure, reaching a constant value when the CO₂ liquefies (McGrail et al. 2007; Ota et al. 2005a; Ota et al. 2007). The replacement ratio increases when a mixture of CO₂ and N₂ is used for replacement because the smaller N₂ molecule facilitates the replacement of CH₄

from the small cage in structure I hydrate (Park et al. 2006).

The stability of hydrate-bearing sediments during CH₄-CO₂ replacement is not yet well understood. In this study, we monitor pore-scale changes in electrical resistance and stiffness to gain an in-depth view of ongoing process. We choose these measurements because of the pronounced sensitivity of underlying physical parameters to phase changes. In particular, the electrical resistivity of water, hydrate, liquid CO₂ and CH₄ gas are ordered as $\rho_{H_2O} < \rho_{hyd} < \rho_{CO_2\text{-liquid}} < \rho_{CH_4\text{gas}}$ from $\rho \sim 0.2\Omega\text{m}$ for sea water to $\rho \sim \infty$ for gas. On the other hand, stiffness ranks as follows $B_{CH_4\text{gas}} < B_{CO_2\text{-liquid}} < B_{H_2O} < B_{hyd}$ (Note: the bulk modulus of liquid CO₂ is almost one order of magnitude lower than that of water). These observations guide the design of the device and test methodology used in this study.

6.2. EXPERIMENTAL STUDY

The experimental device is designed to explore hydrate formation and CH₄-CO₂ replacement at a small-scale, such as at the water meniscus that forms between particles in a partially water-saturated sediment.

6.2.1. Device

The test consists of a thin cylindrical water layer (8.8mm diameter, 0.9mm in height; and 55mg water mass) retained by surface tension between two conductive aluminum disks (Fig. 1a). These disks are bonded onto corresponding piezocrystals. The device is

housed in a high pressure chamber within a temperature controlled environment (Fig. 6.1b). The water droplet is recorded using time-lapse photography to confirm phase changes and to observe volume changes (resolution: 1pixel~10 μ m). Pressure and temperature are measured with a pressure transducer and a thermocouple respectively, and values are recorded every two seconds using a data logger.

Fig. 6.1c shows the electrical circuit and peripheral electronics used to measure electrical resistance and relative stiffness. Electrical resistance is determined at 50 *kHz* to avoid electrode polarization effects. The resistance of the medium *R* is a function of measured voltages V_1 and V_2 , and the known resistance of the series resistor $R^*=4700\Omega$,

$$R = \frac{V_2}{V_1 - V_2} R^* \quad (6.1)$$

The source piezocrystal is connected to a sinusoidal signal generator operated at ~60 *kHz*. The signal amplitude produced by the output piezocrystal is measured using an oscilloscope.

6.2.2. Experimental Procedure

Multi-stage P-T trajectories are imposed in three different experiments. For clarity, a single, complete test sequence is reported in this manuscript. Similar results were obtained in all other tests. The P-T trajectory during this experiment consists of three stages (Fig. 6.2): (1) ice formation and melting followed by CH₄ hydrate formation, (2) CH₄-CO₂ replacement, and (3) hydrate dissociation. Details for each stage follow.

Transient ice formation (Fig. 6.2-a). A droplet of de-aired water ($\rho_w=231\Omega\text{m}$) is placed between the two aluminum substrates, creating a cylindrically shaped meniscus. The chamber is briefly vacuumed, then pressurized with CH_4 gas to 8.1MPa and kept at a temperature $\sim 277^\circ\text{K}$ for 11 hours under quiescent conditions. The pressure and temperature are rapidly decreased to 3.7MPa and 250°K to form ice (some hydrate may form as well).

CH_4 Hydrate formation (Fig. 6.2-a). Within 2 minutes after partial depressurization, pressure and temperature are increased back to 7.6MPa and 277°K , to melt the ice within the CH_4 hydrate stability field. These P-T values are maintained constant for 23 hours to allow for CH_4 hydrate growth.

Injection of CO_2 (Fig. 6.2-b). CH_4 gas is allowed to leak out of the chamber, and P-T condition is maintained inside of the CH_4 hydrate stability field, while CO_2 is injected into the chamber. Eventually the hydrate mass is submerged in liquid CO_2 . Pressure and temperature are kept at $P=7\text{MPa}$ and $T=276^\circ\text{K}$ for 19 hours.

Hydrate dissociation (Fig. 6.2-c). Depressurization is conducted in three steps: from liquid CO_2 to gas CO_2 (c0 to c1), between CH_4 and CO_2 phase boundaries (c2 to c3), and out of the CO_2 hydrate stability field (c3 to c4).

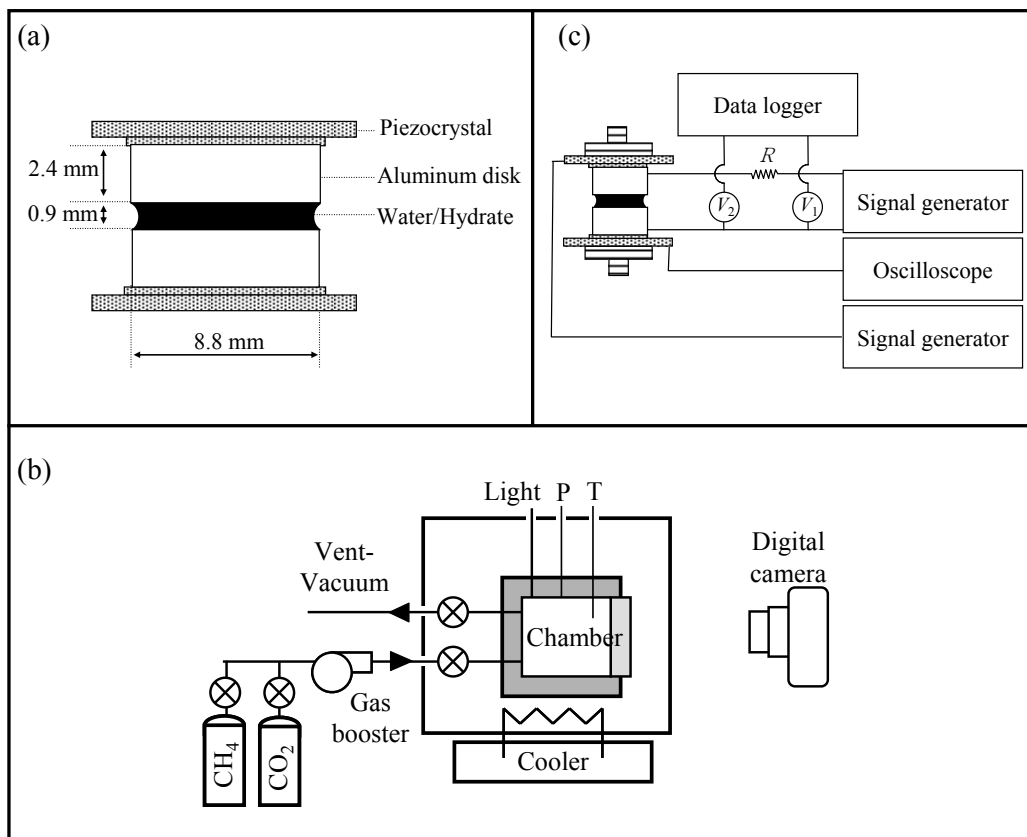


Figure 6.1. Experimental devices and components: (a) Pore-scale device, (b) Pressure chamber and external components, (c) Peripheral electronics to measure electrical conductivity and relative stiffness.

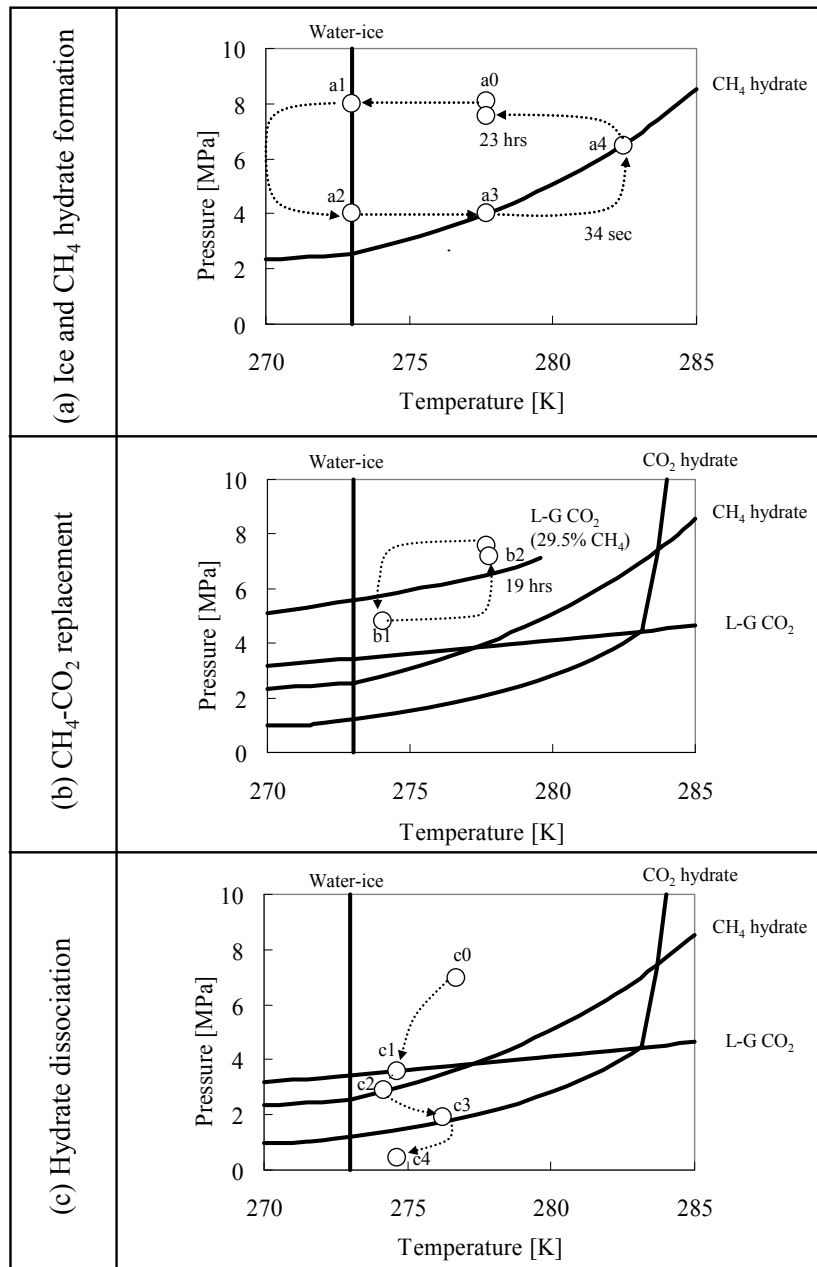


Figure 6.2. Complete P-T history during the experiment: (a0) Water, (a1) Ice forms, (a2) Ice melts, (a3) Leaving the CH₄ hydrate phase boundary, (a4) CH₄ hydrate nucleation and growth, (b1) CO₂ injection; (b2) Liquid CO₂ forms in the chamber, (c0) Beginning of depressurization, (c1) Gas-liquid CO₂ phase boundary, (c2) CH₄ hydrate phase boundary, (c3) CO₂ hydrate phase boundary, and (c4) End of test.

6.3. EXPERIMENTAL RESULTS

Similar results were obtained in all three multi-stage tests. For clarity, a dataset from a single complete test is reported here. Pressure, temperature, electrical resistance R and relative stiffness K measured during the tests are summarized in Figure 6.3. All parameters are plotted versus time. Note that time is zeroed at the center of the main process under consideration in each column, and plotted using a cubic root scale to show short-time effects in high resolution together with long-time changes. The evolution of the water droplet photographed through the sapphire window is documented in Fig. 6.4 (For clarity, we show traces of the original photographs).

Transient ice formation. A pronounced increase in resistance and stiffness accompany ice formation (Fig. 6.3 - column A). There is only a minor volume change (Fig. 6.4b).

CH₄ hydrate formation. Ice melts and CH₄ hydrate starts forming upon repressurization back inside CH₄ hydrate stability field. The electrical resistance R and relative stiffness K decrease fast as the ice melts (between points a2 and a3 - Fig. 6.3, column A). Therefore, there is virtually no hydrate formation during ice melting even though P-T conditions are within the hydrate stability field. This suggests that thermal diffusion-limited ice melting is much faster than diffusion-controlled hydrate formation.

Any hydrate that may have formed dissociates between points a3 and a4 (Fig. 6.2 and Fig. 6.3 - column A), then both resistance R and stiffness K begin to gradually increase

during CH₄ hydrate formation (after a4 - Fig. 6.3 - duration 23hours), however, neither resistance nor stiffness reach the values attained during ice formation. Volume expansion during hydrate growth causes water to flow out of the meniscus, and some hydrate forms on the aluminum surface (Fig. 6.4c).

Injection of CO₂. Minor changes in electrical resistance R and relative stiffness K are observed during the injection of CO₂ gas (Fig. 6.3 – points b1 to b2 – Note: This is confirmed in all our tests). However, resistance R and stiffness K increase fast as soon as liquid CO₂ conditions are exceeded (See also Ota, et al., 2007). Both K and R reach values higher than during CH₄ hydrate formation (point b2 – Fig. 6.3). The mixed CH₄-CO₂ gas leads to a modified G-L CO₂ boundary, and liquid CO₂ forms above the liquid-gas P-T condition for pure CO₂ (Fig. 6.2 – point b2. See related data in Donnelly and Katz 1954).

Hydrate dissociation. Depressurization from liquid CO₂ to gas CO₂, and out of the CH₄ phase-boundary, causes no observable change in the electrical resistance R and relative stiffness K . Therefore, we infer that CO₂ hydrate fills the meniscus (Fig. 6.3 – point c1 and c2). Finally, hydrate dissociates at the CO₂ hydrate phase boundary (Fig. 6.2 and 6.3 – point c3). As hydrate dissociates, resistance R and stiffness K return to the initial values measured for the water droplet at the beginning of the test. The water loss from the beginning to the end of the test is estimated to be ~15% based on the photographic record.

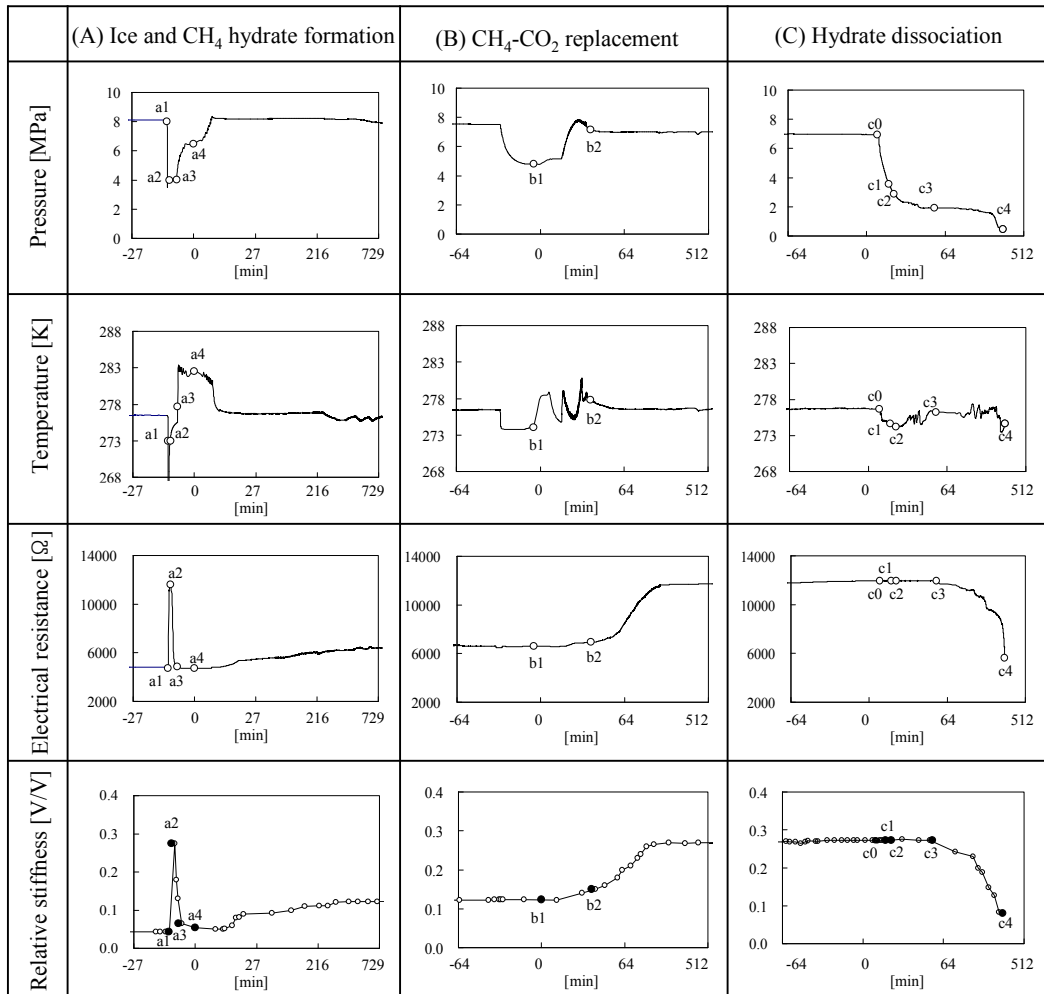


Figure 6.3. Evolutions of pressure, temperature, electrical resistance, and relative stiffness during all experiments at stages (Refer to Figure 6.2 for detailed P-T path): (a0) Water, (a1) Ice forms, (a2) Ice melts, (a3) Leaving the CH₄ hydrate phase boundary, (a4) CH₄ hydrate nucleation and growth, (b1) CO₂ injection; (b2) Liquid CO₂ forms in the chamber, (c0) Beginning of depressurization, (c1) Gas-liquid CO₂ phase boundary, (c2) CH₄ hydrate phase boundary, (c3) CO₂ hydrate phase boundary, and (c4) End of test. Note: A cubic time scale is used to capture both short and long duration events.

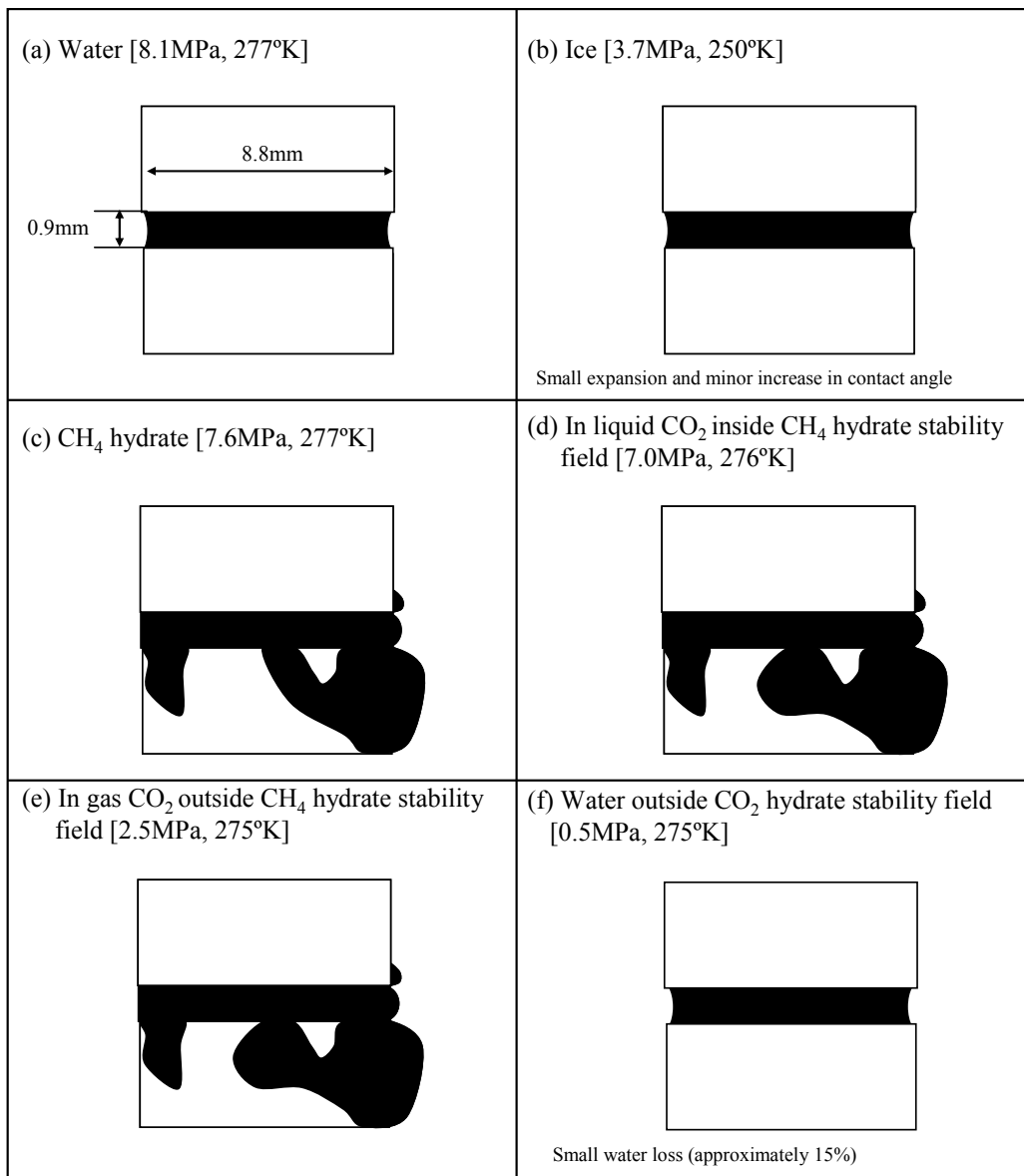


Figure 6.4. Traces of photographs obtained during the replacement: (a) Water droplet, (b) Ice formation, (c) CH₄ hydrate formation and growth, (d) After the injection of liquid CO₂, (e) Depressurization out of the CH₄ hydrate stability field, and (f) Image after hydrate dissociation.

6.4. ANALYSES AND DISCUSSION

Volume expansion. There is pronounced volume expansion during CH₄ hydrate formation; a theoretical estimate shows that $V_{\text{CH}_4\text{hyd}}/V_w=1.23$ for a hydration number $n=6$. Volume expansion causes water to flow out of the meniscus, readily forming hydrate on the sides of the aluminum block (Fig. 6.4c). CH₄-CO₂ replacement and additional CO₂ hydrate formation of any remaining free water inside the meniscus can cause additional volume expansion as seen in Figure 6.4d ($V_{\text{CO}_2\text{hyd}}/V_w=1.28$). Note that the volume of CO₂ hydrate is slightly larger than for CH₄ hydrate ($V_{\text{CO}_2\text{hyd}}/V_{\text{CH}_4\text{hyd}}=1$ -to-6% – Jung, et al. 2010).

Relative stiffness. Relative stiffness measurements can be analyzed assuming a mechanical system made of three springs in series held between fixed boundaries: the two end springs represent the two piezocrystals, and the central spring corresponds to the meniscus (either water, ice or hydrate). Infinite stiffness connectors between the springs represent the two aluminum disks. The relative amplitude between the input V_i and output V_o voltages is a function of the displacement δ_i and δ_o in both input and output piezocrystals, which depends on the meniscus response $\delta_m=-\delta_o-\delta_i$ through a function that combines the stiffness of piezocrystals k_{piezo} , the meniscus height ($L_m=0.9\text{mm}$), the medium Young's modulus E_m , and the area of the meniscus $A_m=60.8\text{mm}^2$,

$$\frac{V_o}{V_i} = \alpha \frac{\delta_o}{\delta_i} = \alpha \frac{\delta_o}{\delta_o + \delta_m} = \alpha \frac{1}{1 + \frac{k_{piezo} L}{E_m A_m}} \quad (6.2)$$

where α is the ratio between the mechano-electric and electro-mechanical piezocrystal effects. Parameters α and k_{piezo} are inferred by assuming known condition at 100% ice and 100% CO₂ hydrate ($\alpha=1.39$ and $k_{piezo}=2.62 \times 10^9 \text{N/m}$ assuming $E_{ice}=9.5 \text{GPa}$ and $E_{hyd}=8.4 \text{GPa}$). Equation 6.2 shows that the voltage ratio V_o/V_i is indeed a measure of meniscus stiffness $E_m A_m/L_m$ relative to the stiffness of piezocrystals k_{piezo} . The CH₄ hydrate mass obtained using the measured voltage ratio $(V_o/V_i)_{\text{CH}_4\text{hyd}}=0.129$ is 47% of the meniscus volume.

Electrical resistance. Electrical resistance R is a function of resistivity ρ , meniscus length L_m , area A_m , and a shape factor β ,

$$R = \beta \cdot \rho \frac{L_m}{A_m} \quad (6.3)$$

When an annular CH₄ hydrate shell forms, the measured resistance reflects the contributions of water and hydrate in parallel disregarding ion exclusion.

$$\begin{aligned}
\frac{1}{R_{water+hyd}} &= \frac{1}{R_{hyd}} + \frac{1}{R_{water}} \\
&= \frac{1}{\beta \cdot L} \left(\frac{A_{total} - A_{water}}{\rho_{hyd}} + \frac{A_{water}}{\rho_{water}} \right) \\
&\approx \frac{1}{L} \frac{A_{water}}{\rho_{water}}
\end{aligned} \tag{6.4}$$

where the final approximation applies to a shape factor $\beta=1$ for a short cylinder and a ratio of resistivity $\rho_{ice}/\rho_{water} \approx \rho_{hyd}/\rho_{water} \ll 1.0$. For an initial water resistivity $\rho_{water}=231\Omega\text{m}$ measured before CH_4 hydrate formation, a lower bound estimated (disregarding ion exclusion) of the CH_4 hydrate volume is 48% of the total meniscus volume. We conclude that (1) a significant part of the meniscus remains as free water 23 hours after the initiation of CH_4 hydrate formation, and (2) the computed CH_4 hydrate growth rate confirms that CH_4 hydrate formation is CH_4 diffusion-limited through the annular hydrate shell (CH_4 gas diffusivity through CH_4 hydrate $7.6 \times 10^{-13} \text{ m}^2/\text{s}$ – Davies, et al.,2008).

Replacement. Both, relative stiffness and electrical resistance increase at all times during replacement. Therefore, while the transformation requires the opening of the hydrate cage to release the CH_4 and entrap the CO_2 molecule (Jung et al. 2010), this solid-liquid-solid exchange takes place locally at the reaction front, while the rest of the hydrate mass remains solid. Therefore, no stiffness loss should be expected at the sediment scale.

The $\text{CH}_4\text{-CO}_2$ exchange rate is faster than the rate of CH_4 hydrate formation (data in columns B and C in Fig. 6.3), and there is additional volume expansion (compare

pictures traced in Fig. 6.4 c and d). Both observations point towards the formation of a porous and pervious CO₂ hydrate shell, probably due to the liberation and expansion of CH₄ gas.

6.5. CONCLUSIONS

Pore-scale electrical resistance and relative stiffness measurements provide unique insight into hydrate formation, CH₄-CO₂ replacement, and hydrate dissociation.

In the absence of fluid flow, CH₄ hydrate formation is diffusion-controlled initially through the water phase until hydrate forms. Thereafter, CH₄ must diffuse through the hydrate mass to reach any isolated free water that is surrounded by hydrate. Consequently, free water can remain in an excess CH₄ gas system for a relatively long time.

Hydrate formation is much slower than thermal diffusion limited ice melting (at mm-scale). Therefore, hydrate formation is not concurrent with ice melting within hydrate stability field conditions in most laboratory situations.

Both CH₄ hydrate formation and CH₄-CO₂ replacement cause pronounced volume expansion. During replacement, the newly formed CO₂ hydrate shell must be fractured or porous in order to allow for the high exchange rates observed in this study.

While CH₄-CO₂ replacement requires the opening of the hydrate cage (i.e. a solid-liquid-solid transformation), both electrical resistance and relative stiffness measurement suggest that CH₄-CO₂ replacement occurs locally and gradually so that the overall hydrate mass remains solid and no stiffness loss should be expected at the sediment scale.

CHAPTER VII
PROPERTIES AND PHENOMENA RELEVANT TO CH₄-CO₂
REPLACEMENT IN HYDRATE-BEARING SEDIMENTS

7.1 INTRODUCTION

Global sustainability, in terms of energy needs and climate stress from greenhouse gases, requires new sources of energy and the management of CO₂ emissions. Methane hydrate is a potential energy source, with worldwide reserves on the order of 500-to-10,000 Gt of carbon (Collett 2002; Kvenvolden 1988; Milkov 2004; Ruppel and Pohlman 2008). Methane can be recovered from hydrate bearing sediments by depressurization, heating or chemical injection. In particular, the injection of carbon dioxide, CO₂, into hydrate-bearing sediments can liberate methane, CH₄, and sequester CO₂ in hydrate form (McGrail et al. 2007; Ota et al. 2005a; Stevens et al. 2008; Svandal et al. 2006; Zhou et al. 2008a).

The chemical potential difference between CH₄ and CO₂ hydrate indicates that CH₄-CO₂ gas replacement is thermodynamically favorable (Seo and Lee 2001; Svandal et al. 2006). However, the extent of the reaction and its efficiency in real systems is determined by multiple factors and coexisting processes, such as (1) pressure and temperature-dependent solubilities and interfacial properties, (2) relative viscosity, permeability, and density between water and CO₂, (3) invasion patterns and specific

surface of the hydrate phase, (4) fluid expansion after replacement, and (5) changes in effective stress. These phenomena couple to determine replacement efficiency and the geomechanical response of the sediment mass.

In this manuscript, we review previous CH₄-CO₂ replacement studies, identify and analyze underlying processes, present new experimental results, and anticipate potential implications.

7.2 PHYSICAL AND THERMODYNAMIC PROPERTIES

The process of replacing CH₄ with CO₂ in hydrate must be understood at both the molecular scale and the macroscale to anticipate conditions for efficient CH₄-CO₂ replacement and its consequences on thermal, mechanical and electrical properties. In this section, we summarize physical parameters in tabular form and highlight the most relevant observations in the text.

2a- Structure: Geometry and length scales (Table 7.1-a). Both CH₄ and CO₂ form structure I hydrate. This crystallographic structure is composed of 2 small cages for every 6 large cages, so the stoichiometric formula is 6X·2Y·46H₂O, i.e., a maximum of 6 gas molecules X in large cages plus a maximum of 2 gas molecules Y in small cages, and 46 water molecules. The lattice repeats every ~12Å (Sloan and Koh 2008). Thus, gas molecules make up a significant molar fraction ~15% of the hydrate structure (compare to the gas solubility in liquid water ~0.1% molar fraction, section 2e).

The stoichiometric ratio (number of water molecules / number of gas molecules) often deviates from the theoretical value $n=46/8=5.75$ for structure I hydrate. In particular, the occupancy of CO_2 molecules in small cages increases with pressure and the stoichiometric ratio decreases from ~ 6.6 at 1.3MPa and 273.15K, to the theoretical limit 5.75 at 4.5MPa and 283.15K (Anderson 2003; Klapproth et al. 2003). The CH_4 molecule is slightly smaller than CO_2 and fits more easily in small cages, so the stoichiometric ratio for CH_4 hydrate is typically $n=6$ (Circone et al. 2005). As a result, the stoichiometric ratio of CH_4 hydrate is less sensitive to pressure than the stoichiometric ratio of CO_2 hydrate.

Fig. 7.1 shows hydrate forming molecules and related molecular structures; they are drawn using the corresponding van der Waals radii and are shown at the same scale. The size of the opening between water molecules that form the face of big cages is smaller than the size of both CO_2 and CH_4 molecules. This simple observation leads us to conclude that the hydrate cage must separate to release the CH_4 molecule before it can trap CO_2 . The molecule of nitrogen N_2 is smaller than CO_2 and fits more easily in the small cages of sI hydrate; this explains the enhanced CH_4 replacement efficiency obtained when a mixture of CO_2 and N_2 is used in a water-limited CH_4 hydrate system of structure I, or of structure II if combined with C_2H_6 (Park et al. 2006).

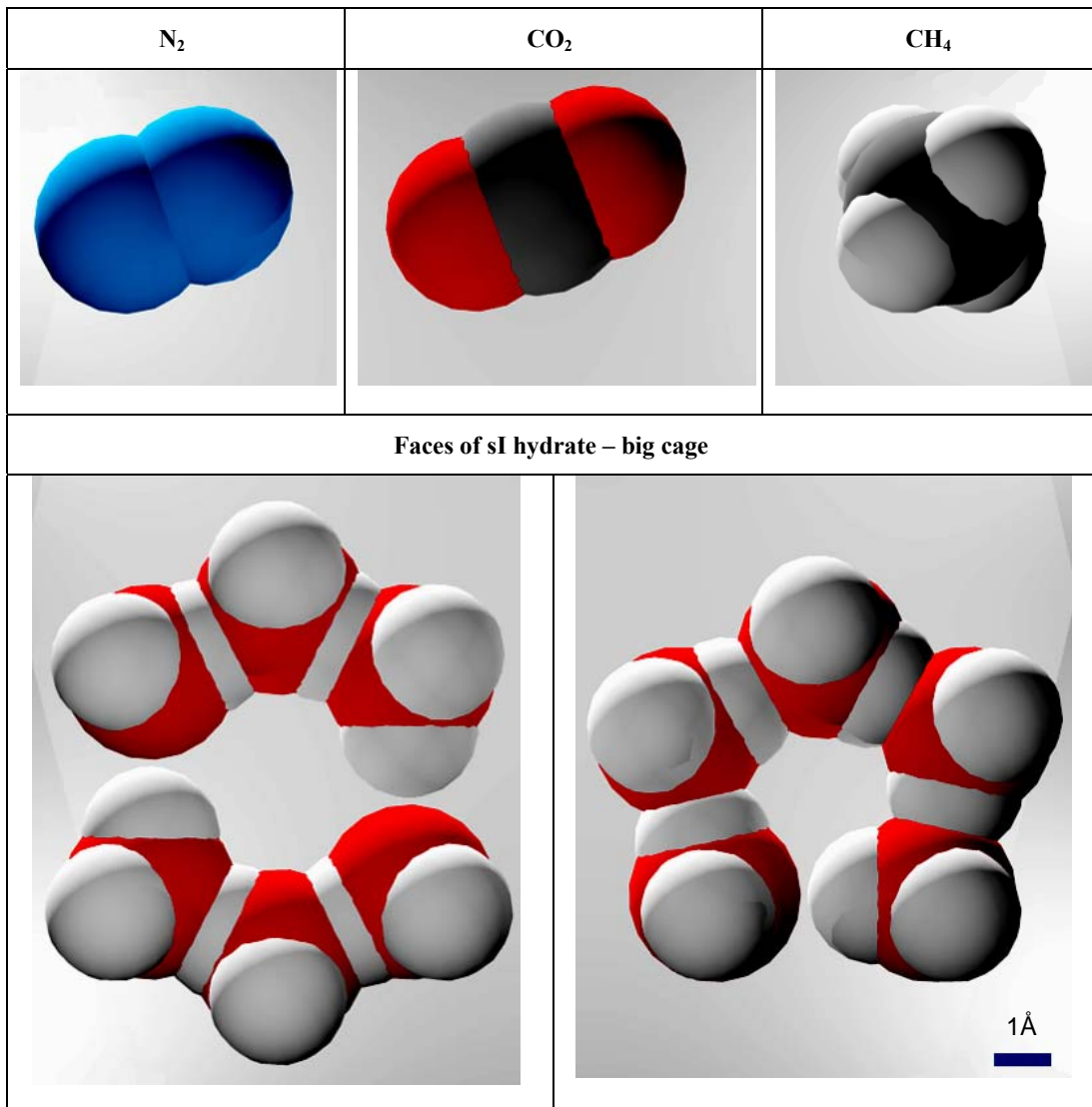


Figure 7.1. Hydrate forming molecules (N₂, CO₂ and CH₄) and two faces of the big cage in sI hydrate. All molecules are drawn using van der Waals radii to the same scale. Hexagonal and pentagonal faces are not regular polygons. Notice that the opening between water molecules is smaller than the size of N₂, CO₂ and CH₄ molecules.

2b- Thermal properties (Table 7.1-b). In agreement with Le Châtelier's principle, hydrate formation is an exothermic reaction. In particular, the heat liberated during the formation of a mol of CO₂ hydrate varies between $H_{\text{CO}_2\text{-hyd}}=57.7$ and 63.6 kJ/mol (Note: a mol of CO₂ hydrate is 44g + n 18g where $n=5.75$ -to-6.6) (Anderson 2003). Conversely, hydrate dissociation is endothermic as heat is needed to disorganize the crystal structure. The heat adsorbed during the dissociation of a mol of CH₄ hydrate is $H_{\text{CH}_4\text{-hyd}}=52.7$ -to-55.4 kJ/mol where a mol of CH₄ hydrate is 16g + n 18g and $n\sim 5.75$ (Anderson 2004). Therefore, CH₄-CO₂ replacement is exothermic. The path assumed here involves complete CH₄ hydrate dissociation before CO₂ hydrate formation. Molecular dynamic simulations for CH₄-CO₂ replacement in the first monolayer (interface between CH₄ hydrate and liquid CO₂) show only partial dissociation of the hydrate cage and lower enthalpy change for the complete replacement reaction [Bjorn Kvamme 2010, personal communication]. Experimental and numerical data are still needed to assess the evolution of the reaction when a large hydrate mass is involved, as in the pore space of sediments, where the characteristic length scale is much greater than the crystal nm-scale.

The thermal conductivity λ and diffusivity κ of liquid CO₂ are significantly lower than the corresponding values for either hydrates or water. In addition, water has the highest heat capacity c among all participating phases. This combination of thermal properties suggests reduced heat dissipation and increased local heating where liquid CO₂ displaces water and contacts CH₄ hydrate.

2c- Mechanical properties (Table 7.1-c). The viscosity of water is one-to-two orders of magnitude higher than the viscosity of liquid CO₂; this pronounced difference in viscosity will affect fluid invasion flow paths. Bulk densities are similar for hydrate and water, ordered as $\rho_{\text{CH}_4\text{hyd}} < \rho_{\text{H}_2\text{O}} < \rho_{\text{CO}_2\text{hyd}}$. The density of liquid CO₂ may exceed that of water, $\rho_{\text{CO}_2(l)} > \rho_{\text{H}_2\text{O}}$ (e.g. at 273.15K for pressures above 25MPa); differences in fluid density contribute to buoyancy effects on fluid flow. Liquid CO₂ is heavier than water in deep sea locations, but remains lighter than water near the continental shelf.

The volume of water V_w increases when hydrate forms: $V_{\text{hyd}} \sim 1.234 V_w$ for CH₄ hydrate and $V_{\text{hyd}} \sim 1.279 V_w$ for CO₂ hydrate. Such a large volumetric change within the pore space causes volumetric strains in the sediment during hydrate formation and promotes skeletal instability and contraction during dissociation (Lee et al. 2010). The shear stiffness of CH₄ hydrate is $G \approx 3.5\text{GPa}$ (a similar value is expected for CO₂ hydrate). Bulk moduli for liquid H₂O and CO₂ are lower than that of solid hydrates, and the bulk modulus of liquid CO₂ is almost one order of magnitude lower than that of water. Correspondingly, the P-wave velocity is ~ 3 times slower in liquid CO₂ than in water. The addition of CO₂ in hydrate reservoirs could increase measured seismic wave velocities by forming additional hydrate, or it could lower the measured velocity by displacing pore water. The interpretation of seismic data gathered during CO₂ injection must account for changes in both hydrate saturation and pore-fluid composition.

2d- Electrical properties (Table 7.1-d). The permittivity of liquid water is determined by the orientational polarization of water molecules. The water dipole rotation is hindered in hydrates. In addition, CH₄ and CO₂ are non-polar molecules and do not contribute to orientational polarization. Hence, gas hydrates have much lower permittivity compared to liquid water (Galashev et al. 2006). The electrical conductivity of water increases almost linearly with ionic concentration at low salt concentration and it is much higher than the electrical conductivity of hydrates. The electrical conductivity of liquid CO₂ is even lower than the electrical conductivity of hydrate. As with seismic surveys, resistivity surveys must account for pore fluid changes as well as hydrate saturation changes. In contrast to seismic results, in which added hydrate formation and CO₂ displacement of pure water have opposing effects on the measured velocity, the electrical properties are reduced both by added hydrate formation and pore water displacement. Tracking hydrate saturation and pore water chemistry is essential for correctly interpreting electrically-based monitoring techniques.

Table 7.1. Physical properties of CH₄ and CO₂ hydrate, pure CO₂ and water relevant to CH₄ replacement by CO₂ in hydrate bearing sediments.

Property	CH ₄ hydrate(sl)	CO ₂ hydrate (sl)	CO ₂ liquid	H ₂ O liquid
a - Structure				
Stoichiometric ratio or hydration number, #H ₂ O mol/ #Gas mol	5.75 (100% cage occupancy) † ^a 5.81-6.10 [1.9-to-9.7MPa, 263-to-285K] ^a	5.75 (100% cage occupancy) † ^a 6.57 [1.5MPa, 273K] ^b	Refer to Fig. 7.1	
Cage occupancy	~100% Large cage ~70% Small cage [10MPa, 273K] ^b	~100% Large cage ~50% Small cage [1.5MPa, 273K] ^b		
Cavity Size [Å]	7.9, 8.66 ^a	7.9, 8.66 ^a		
Guest Size [Å]	4.36 ^a	5.12 ^a		
Lattice constant <i>a</i> [Å]	11.95 [10MPa, 271.15K] ^b	12.07 [273.2K] ^c		
b - Thermal				
Heat capacity _c [kJ·kg ⁻¹ ·K ⁻¹]	2.031 [263K] ^d 2.080 sI ^a 2.250 sI ^e 2.077 [270K] ^f	No data found	2.280 [280K,10MPa] (highly variable) ^g	4.218 [273K] 4.192 [283K] ^d
Thermal conductivity λ [W·m ⁻¹ ·K ⁻¹]	0.68 [273K] ^d 0.49 [263K] ^a	0.49 [263K] ^a	~0.13 [12.5MPa, 270K] ^h	0.56 [273K] 0.58 [283K] ^d
Thermal Diffusivity $\kappa = \lambda \rho^{-1} c_p^{-1}$ [m ² s ⁻¹]	3.1×10 ⁻⁷ⁱ	No data found	6.07×10 ⁻⁸ †	1.33×10 ⁻⁷ [273K] 1.38×10 ⁻⁷ [283K] ^d
Heat or Enthalpy of Dissociation and Formation ΔH_d [kJ/mol]	52.7-to-56.9 [273K] ^d ~53 [independent of P-T] ^j	63.6-to-57.7 (±1.8) [at quadruple points] ^j	Does not apply	(water to ice) ~6 ^d

Property	CH ₄ hydrate(sl)	CO ₂ hydrate (sl)	CO ₂ liquid	H ₂ O liquid
c - Mechanical				
Viscosity μ [Pa·s]	Does not apply	Does not apply	(2-to-8)×10 ⁻⁵ [5-to-30MPa, 318K] ^o	~1.5×10 ⁻³ [293K] ^p
Density ρ [kg·m ⁻³]	929 [263K] ^d 940 ^a 910[273K] ^{d,q}	1110-to-1090 ^r [30MPa] 1054 ⁿ	~938-to-800 kg/m ³ [10MPa, 280-to- 300K] (highly variable) ^g	999.9 [0.1MPa, 273K] 1003±1.5 [10MPa, 280- to-300K] 1030±2 [3.5% salinity; 10MPa, 280- to-300K] ^s
Water volume expansion upon hydrate formation V_{hyd}/V_w	1.234 [†] (n=6; $\rho_{CH_4hyd}=930\text{kg/m}^3$; 100% occupancy)	1.279 [†] (n=6; $\rho_{CO_2hyd}=1100\text{kg/m}^3$; 100% occupancy)	Does not apply	$V_{ice}/V_w = 1.09$
Coefficient of thermal expansion α [K ⁻¹]	sI hydrate 7.7×10 ⁻⁵ [200K] ^a 2.64×10 ⁻⁴ ^b	sI hydrate 7.7×10 ⁻⁵ [200K] ^a	No data found	2±0.3×10 ⁻⁴ [50MPa, 273.15-to- 283.15K] ^w
Bulk Modulus [GPa]	7.2 [277K] ^f ~9 [273K] ^b 8.73 [273K] ^v	No data found	0.338-to-0.124 GPa [10MPa, 280-to-300K] [†]	2.1-to-2.3 GPa [10MPa, 280- to-300K] [†]
Shear Modulus [GPa]	3.2 [277K] ^f 3.54 [273K] ^v	No data found	0	0
Poisson ratio	0.32 [273K] ^v	No data found	~0.5	~0.5
V _P [m/s]	3775 [273K] ^v	No data found	~600-to-400 m/s [10MPa, 280-to- 300K] ^g	1450-to-1518 [10MPa, 280- to-300K] ^x
V _S [m/s]	1954 [273K] ^v	No data found	0	0
d - Electrical				
Electrical conductivity [S/m]	0.01 ^y	No data found	<10 ⁻² at less than 3000K ^z	depends on ionic concentration Sea-water: ~5
Dielectric permittivity (freq. < 1GHz)	~2.5 [273K] ^y	No data found	1.0 to 1.5 from 1 to 20MPa, 308K ^a	79-to-80 ^{ae}

† computed value; a-(Sloan and Koh 2008); â-(Circone et al. 2005); b-(Klapproth et al. 2003); c-(Uchida et al. 1999); d-(Waite et al. 2009); e-(Makogon 1997); f-(Handa 1986) (Yoon et al. 2003); g-(Span and Wagner 1996); h- (Vesovic et al. 1990); i-(Waite et al. 2007); j-(Anderson 2003; Anderson 2004); k-(Davies et al. 2008); L-(Mori and Mochizuki 2000); m- as in (Mochizuki and Mori 2006); n-(Uchida et al. 1999); o-(Thomas and Adams 1965); p-(Fenghour et al. 1998; Netherton et al. 1977); q-(Kieft et al. 1985); r-(Aya et al. 1997); s- (Millero and Poisson 1981); v-(Helgerud et al. 2009); w-(Bradshaw and Schleicher 1970); x-(Belogol'skii et al. 2002); y-(Galashev et al. 2006); z-(Tanaka et al. 2008), æ-(Goldfarb et al. 1999; Obriot et al. 1993), and œ-(Israelachvili 1991).

2e- Chemical properties: phase boundaries, solubilities and diffusivities (Tables 7.2, 7.3 and 7.4). Hydrate stability and gas solubility in water are pressure and temperature dependent.

1) *Phase boundaries*: We develop regression equations for CO₂ and CH₄ hydrate phase boundaries, and for the liquid-vapor, L-V, boundary for CO₂ by fitting values predicted using experimentally validated thermodynamic models by Duan and Sun (2003; 2005) (Table 7.2). Hydrate grown from a mixed CH₄-CO₂ gas atmosphere exhibits an intermediate phase boundary, between the boundary for pure CH₄ and CO₂ hydrates, where the relative position scales with the mixture ratio (Adisasmito et al. 1991; Seo and Lee 2001). The liquid-vapor, L-V, boundary shown in Fig. 7.2 corresponds to pure CO₂. Even small amounts of CH₄ in CO₂ cause the gas mixture L-V boundary to shift towards higher pressures, e.g. CO₂ with 10% CH₄ condenses at a pressure ~2MPa higher than the pressure needed for pure CO₂ (Donnelly and Katz 1954). It can be observed from Fig. 7.2 that: CH₄ hydrate stability requires higher pressures than CO₂ hydrate for temperatures $T \leq 283.67\text{K}$. These boundaries partition the P-T space into four regions: CH₄ hydrate may be surrounded by liquid CO₂ (Zone A) or by gaseous CO₂ (Zone B) if $T < 277.1\text{K}$; CO₂ hydrate can coexist with either liquid CO₂ (zone C) or with gaseous CO₂ (zone D).

Table 7.2. Phase boundaries for pure CH₄ and CO₂ hydrates, and liquid-vapor boundary for pure CO₂, calculated by fitting values predicted using the experimentally validated formulation in Duan and Sun (2003; 2005).

<i>CH₄ hydrate stability boundary</i>	<i>CO₂ hydrate stability boundary</i>
Ice-hydrate-CH ₄ gas $P^* = 17.126T^* - 14.584$ if $263 < T \leq 273.15\text{K}$	Ice-hydrate-CO ₂ gas $P^* = 8.082 T^* - 7.020$ if $263 < T \leq 272.15\text{K}$
Liquid water-hydrate-CH ₄ gas $T^* = 0.0396 e^{(-6.46 \times 10^{-4} P^*)} [24.348 + \text{Ln}(P^*)]$ if $273.15 < T < 290\text{K}$	Liquid water-hydrate-CO ₂ gas $T^* = 0.0358 e^{(-0.00285 P^*)} [27.829 + \text{Ln}(P^*)]$ if $272.15 < T \leq 283.17\text{K}$
	Liquid water-hydrate-CO ₂ liquid $P^* = 3.34 \times 10^{-4} (T^*)^{264.4}$ if $283.17 < T < 290\text{K}$
<i>CO₂ Liquid-vapor phase boundary</i>	
$P^* = 3.45 (T^*)^{7.00}$ if $263\text{K} < T \leq T_{\text{critical}} = 304.1\text{K}$	
(Note: boundary shifts to higher pressures in CH ₄ /CO ₂ gas mixtures) ^a	

Definitions: $P^* = P/1\text{MPa}$; $T^* = T/273.15\text{K}$.

Note: (a) (Donnelly and Katz 1954).

2) *Solubility in liquid phases*: Table 7.3-a shows a summary of solubility values for all participating species in different media; the simultaneous presence of CH₄ and CO₂ in water alters the solubilities shown for simple binary systems (Qin et al. 2008). The solubility of CH₄ and CO₂ in water affects gas transport, hydrate formation and hydrate dissolution in water that is not fully saturated with gas. The solubility of CO₂ in water is about 10 times greater than that of CH₄; both solubilities increase as pressure increases and temperature decreases. The presence of hydrate in water inverts these trends. The amount of dissolved water in liquid CO₂ is not negligible, and can be as high as 0.003-to-0.006 mol/mol, that is ~1kg of water per m³ of liquid CO₂ at $T=285\text{-to-}293\text{K}$ and $P=10\text{-to-}20\text{MPa}$ (Spycher et al. 2003). Hence, liquid CO₂ can remove water, effectively “drying” the sediment.

Similarly, CH₄ is highly soluble in liquid CO₂; for example, a molar mixture of 12% CH₄ and 88% CO₂ remains liquid above a line defined between [6.6MPa, 273.1K] and [7.2MPa, 278.1K], as can be estimated from the bubble point line (Donnelly and Katz 1954). This observation explains experimental results at 8.7MPa and 277.1K where no CH₄ bubbles were observed during CH₄-CO₂ replacement [$\sim 2/40$ moles of CH₄/moles of CO₂] (Dunk et al. 2006) as the liquid CO₂ was able to contain CH₄ molecules in solution preventing the formation of a separate phase. Finally, we observe that, the mixture CH₄-CO₂ has remarkably different bubble-point and dew-point lines as function of the molar ratio between CH₄ and CO₂ (see: Austegard et al. 2006; Donnelly and Katz 1954; Mraw et al. 1978). As a result, gaseous CO₂ and CH₄ will coexist in equilibrium with liquid CO₂ and CH₄ in a fairly large pressure interval.

Table 7.3. Mutual solubilities in binary mixtures. (a) Liquid medium. (b) Gaseous medium.

Rich phase medium		Solute	Concentration [mol/kg]		
			3MPa, 273K	6.6MPa, 274K	10MPa, 285K
(a) Liquid	H ₂ O (without hydrate)	CH ₄	0.11*	0.12*	0.13*
		CO ₂	1.39* [~0.025 mol/mol]	1.66* [~0.030 mol/mol]	1.72
	H ₂ O (with hydrate)	CH ₄	0.060	0.063	0.116
		CO ₂	0.89 [0.016 mol/mol]	0.83 [0.015 mol/mol]	Outside HSZ
	CO ₂	H ₂ O	Does not apply (Gas CO ₂)	0.050 † [2.2×10 ⁻³ mol/mol]	0.056 [2.5×10 ⁻³ mol/mol]
		CH ₄	Does not apply (Gas CO ₂)	Bubble point for 12% molar CH ₄ /CO ₂ mixture	Supercritical mixture
(b) Gas	CH ₄	H ₂ O	0.016 [~2.5×10 ⁻⁴ mol/mol]	0.008 [1.34×10 ⁻⁴ mol/mol]	0.012 [2.0×10 ⁻⁴ mol/mol]
	CO ₂	H ₂ O	0.011 [~5×10 ⁻⁴ mol/mol]	Does not apply (Liquid CO ₂)	Does not apply (Liquid CO ₂)
	CO ₂	CH ₄	Gas mixture	Does not apply (Liquid CO ₂)	Does not apply (Liquid CO ₂)

Sources: (Donelly and Katz 1954; Duan and Sun 2003; Folas et al. 2007; Hashemi et al. 2006; Spycher et al. 2003; Sun and Duan 2007).

Notes: *These values are extrapolations of solubility without hydrate to lower temperatures. †Value for 285K.

3) *Water vapor concentration in gaseous phase* (Table 7.3-b): Water evaporates into gaseous atmospheres. For example, 0.016 kg of H₂O can be found per cubic meter of CO₂ gas at 3MPa-273K (0.011 mol H₂O / kg of CO₂) (Spycher et al. 2003), and 0.005 kg of H₂O can be found per cubic meter of CH₄ gas at 3MPa-273K (0.012 mol H₂O / kg of CH₄) (Folas et al. 2007). We have consistently observed in separate experimental systems that water vapor in either CO₂ or CH₄ atmospheres can crystallize on hydrate surfaces promoting hydrate growth in relatively short time scale (days).

4) *Mutual diffusivities* (Table 7.4): Diffusion controls most long-term phenomena, including hydrate formation and CH₄-CO₂ replacement (Davies et al. 2008; Svandal et al. 2006). The diffusivities of CO₂ and CH₄ in water are about the same, however, the diffusivity of H₂O in liquid CO₂ is up to two orders of magnitude higher (Espinoza and Santamarina 2010). High water diffusivity and solubility in liquid CO₂ make liquid and supercritical CO₂ an effective water-drying fluid agent.

The diffusivity of CO₂, CH₄ or H₂O molecules through the solid hydrate mass is much slower than through liquids (Note: preferential diffusive transport is expected along crystal imperfections and along the adsorbed water layer between hydrate and minerals). Therefore, CO₂ or CH₄ transport through solid hydrate will be much slower than through water. If the CH₄-CO₂ replacement is limited by diffusive transport, laboratory experiments and field implementations must seek to increase the surface contact area.

Table 7.4. Mutual diffusivities in binary water-CO₂ and water-CH₄ systems.

Rich phase medium	Diffusing substance	Diffusivity [m ² /s]	Pressure [MPa]	Temperature [K]	Method	Reference	
Liquid	H ₂ O	CO ₂	1.37×10 ⁻⁹ -to- 1.64×10 ⁻⁹	0.1	291.5-to-298	Experimental	(Thomas and Adams 1965)
		CH ₄	0.85×10 ⁻⁹ -to- 1.49×10 ⁻⁹	0.1	277-to-293	Experimental	(Witherspoon 1969)
	CO ₂	H ₂ O	6×10 ⁻⁸ -to- 18×10 ⁻⁸	7-15	298	Experimental	(Espinoza and Santamarina 2010)
Solid	H ₂ O (I)	CO ₂	0.9×10 ⁻¹⁰	No Data	270	Molecular Dynamics	(Ikeda-Fukazawa et al. 2004)
		CH ₄	1.0×10 ⁻¹⁰	No Data	270		
	CH ₄ (H)	CH ₄	3.4×10 ⁻¹³ -to- 7.6×10 ⁻¹³	3-15	263-to-268	Experimental	(Davies et al. 2008)
	CO ₂ (H)	CO ₂	1.0×10 ⁻¹²	No Data	273	Molecular dynamics	(Demurov et al. 2002)
H ₂ O		1.0×10 ⁻²³	No Data	200			

Note: (I) ice and (H) hydrate.

7.3 PREVIOUS STUDIES – RATES OF REACTION

Previous CH₄-CO₂ replacement studies documented in the literature are summarized in Table 7.5 and P-T conditions are plotted on Fig. 7.2. As noted in Table 7.5, we describe the time dependent replacement of CH₄ by CO₂ using the replacement ratio in the hydrate: $\text{CO}_2 / (\text{CH}_4 + \text{CO}_2) = A (1 - e^{-t/\alpha})$, with A being the maximum replacement ratio at long times, t . We obtain both A and the characteristic time, α , by fitting the published reaction-time data. The following preliminary observations can be made from these studies: (1) hydrate replacement rates increase near the CH₄ hydrate phase boundary (data in (Ota et al. 2005a), also mentioned in (McGrail et al. 2007)), (2) the reaction rate increases with increasing CO₂ gas pressure, eventually becoming constant when CO₂ liquefies (Ota et al. 2007). We can also anticipate that high specific surface CH₄ hydrate experiences relatively fast replacement rates (refer to Kim et al. 1987). There is some supportive evidence in the listed studies, but they are not conclusive due to lack of experimental details.

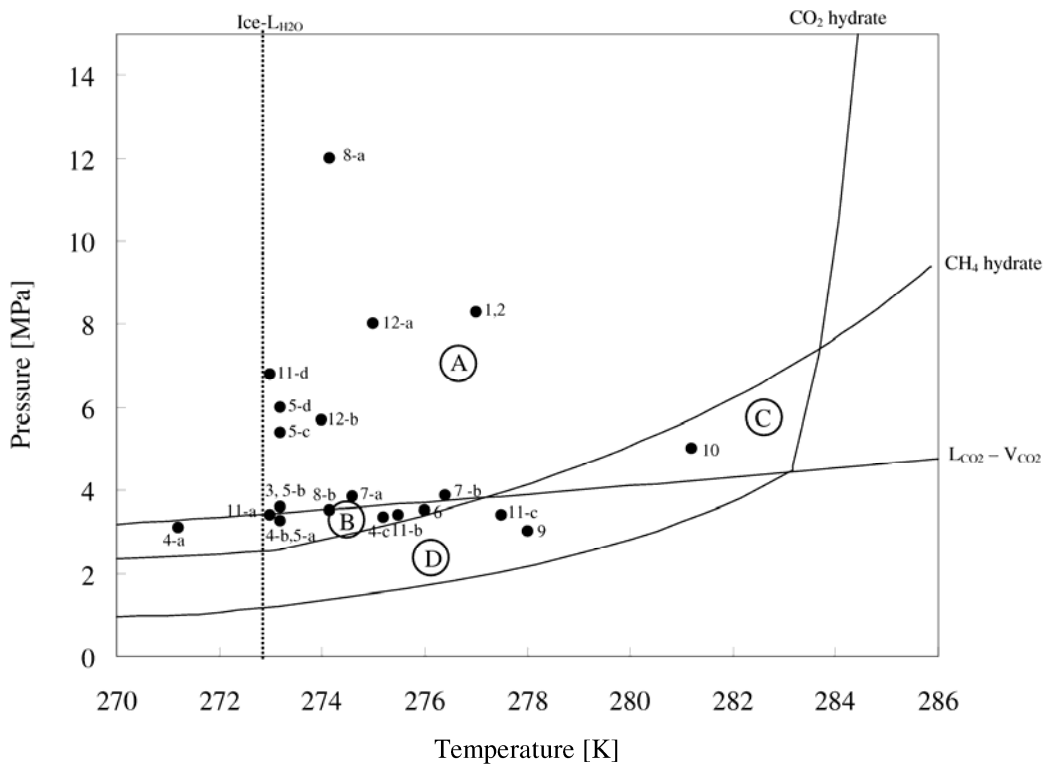


Figure 7.2. Dissociation phase boundaries for CO₂ and CH₄ hydrates, liquid-vapor phase boundary for pure CO₂, and liquid water-ice boundary. Data points show fluid pressure and temperature conditions for CH₄-CO₂ replacement studies reported in the literature (numbers correspond to references listed in Table 7.5). Notice that CO₂ and CH₄ hydrate phase boundaries cross at ~7.5MPa and 283.7K. Furthermore, the CO₂ liquid-vapor boundary intersects the two dissociation lines creating four different zones inside the CO₂ hydrate stability field, above the liquid water-ice boundary.

Table 7.5. Previous CH₄-CO₂ replacement studies. Note: cases are plotted in Fig. 7.2 using the same Test # listed here.

Test #	P [MPa]	T [K]	CH ₄ hydrate formation method	Medium	Duration [hour]	Replacement ratio* [A]	Characteristic time* α [hour]	Monitoring	Reference
1	8.3	277	-	Sandstone	300	0.64	128	MRI	(Husebo et al. 2008)
2	8.3	277		Sandstone	350	-	-	MRI	(Stevens et al. 2008)
3	3.6	273.2	Stirring	No sediment	300	0.34	85	Raman spectroscopy	(Ota et al. 2005b)
4-a	3.10	271.2	Stirring	No sediment	150	0.16	48	Raman spectroscopy	(Ota et al. 2005a)
4-b	3.26	273.2			150	0.16	42		
4-c	3.34	275.2			150	0.21	39		
5-a	3.26	273.2	Stirring	No sediment	300	0.26	98	Raman spectroscopy	(Ota et al. 2007)
5-b	3.6	273.2			300	0.34	94		
5-c	5.4	273.2			300	0.17	94 (1)		
5-d	6.0	273.2			300	0.31	94 (1)		
6	3.5	276	Powder ice: 100 μ m	No sediment	12	0.92	1.0	Raman spectroscopy	(Komai et al. 2000)
7-a	3.85	274.6	Stirring	No sediment	800	0.55	222	Water and gas produced	(Hirohama et al. 1996)
7-b	3.88	276.4			800	0.64	329		
8-a	12.0	274.15	Powder ice: 5-50 μ m	No sediment	30	0.92	4.2	NMR	(Park et al. 2006)
8-b	3.5	274.15			30	0.85	5.2	NMR	
9	3.0	278	Powder ice: 100-250 μ m	No sediment	150	1.00	22	Raman spectroscopy	(Yoon et al. 2004)
10	5.0	281.2	-	Quartz sand	100	0.19	33 (L-CO ₂)	Gas produced	(Zhou et al. 2008b) (2)
						0.27	31 (90% emulsion)		
						0.26	29 (70% emulsion)		
						0.24	26 (30% emulsion)		
11-a	3.4	273	Stirring	No sediment	11	No data	No data	Raman spectroscopy	(McGrail et al. 2007)
11-b	3.4	275.5			11				
11-c	3.4	277.5			11				
11-d	6.8	300-273	-	Sand	1.7				
12-a	8.0	275.0	-	No sediment	-	No data	No data	Time-lapse photography	This study
12-b	5.7	274.0			-	No data	No data		

*Note: replacement ratio= $A(1-e^{-\alpha t})$, A = final replacement ratio, α = replacement rate. (1) Limited data available. (2) Ill-defined test.

7.4 NEW PORE SCALE EXPERIMENTAL STUDIES

Multiple coexisting processes take place during CH₄-CO₂ replacement, including heat release, dissolution of participating species into different phases, volume change and mass transport. The following two experimental studies document these pore-scale processes. Fig. 7.3 shows the experimental devices and P-T trajectories. Both experiments are monitored using time-lapse photography. We use digital image processing to estimate length and volume information (resolution: 1pixel~10μm), and we infer mass changes from measured volumes and the known density of the phases.

Water droplet. A water droplet (initial mass 36.1mg) rests on a hydrophobic PTFE substrate and forms a quasi-spherical body (~2.5mm radius). Air is evacuated from the chamber by imposing a partial vacuum, followed by CH₄ pressurization (P=5.9MPa, T=293K, Fig 7.3-b) and subsequent cooling. Some water evaporates into the methane atmosphere; we predict a ~1.2mg water mass loss from the droplet (based on solubility information in Table 7.3-b). Given a water density of ~1000 kg/m³ (Table 7.1-c), this agrees with the volume reduction we measured after 5 days (±0.1mg precision). The first hydrate formation event follows transient ice formation. Later, we dissociate this CH₄ hydrate by heating (not shown in Fig. 7.3-b), and we cool the sample back into the CH₄ hydrate stability field. CH₄ hydrate nucleates again in the form of a hydrate film that grows at the water-gas interface and propagates along the interface at a velocity of ~0.02mm/s, forming a complete hydrate shell in less than 5 minutes. For this growth velocity, heat transfer models predict a hydrate film thickness greater than 40μm

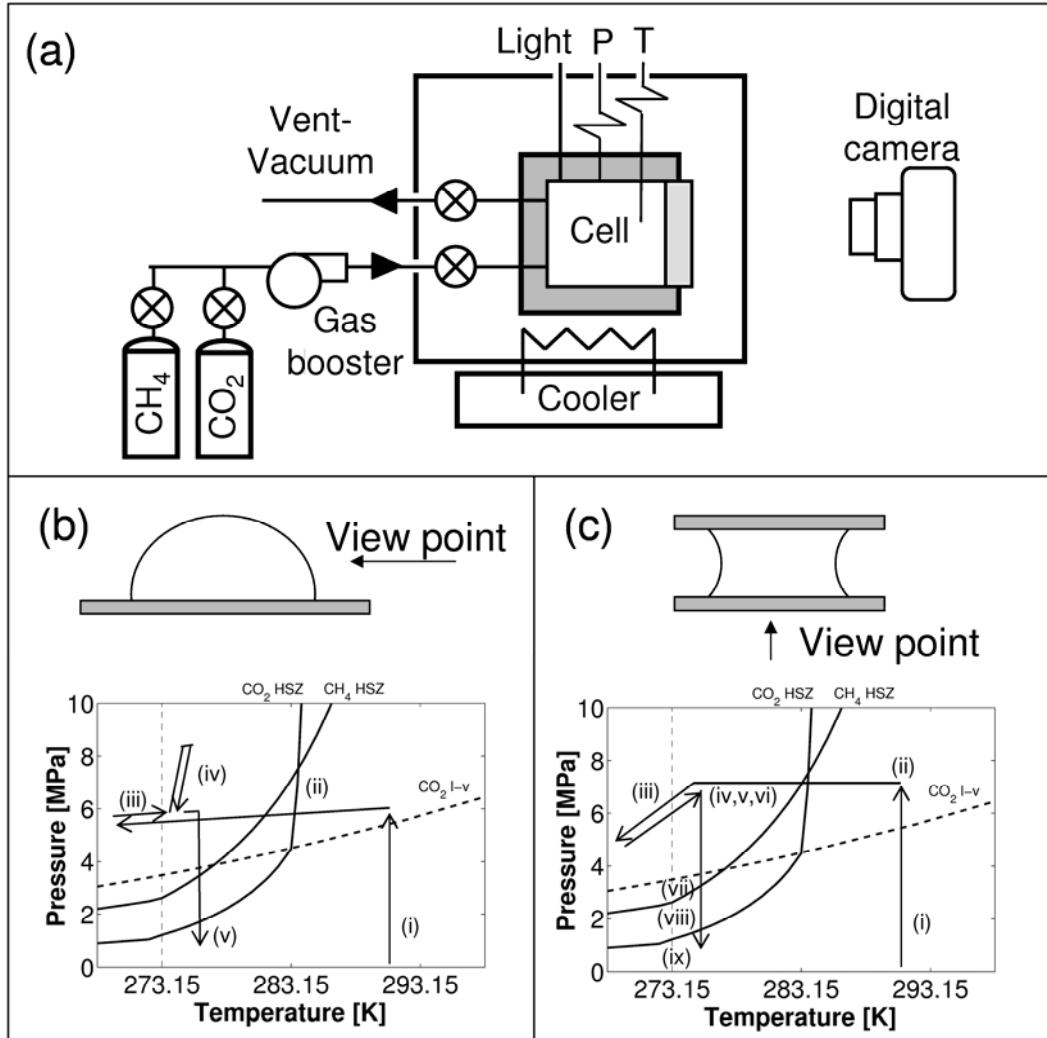


Figure 7.3. Experimental studies. (a) Pressure cell and devices. (b) Droplet experiments: i- CH_4 pressurization, ii- cooling, iii- CH_4 hydrate formation, iv- liquid CO_2 injection, v- CH_4 - CO_2 hydrate dissociation. (c) Meniscus experiments: i- CH_4 pressurization, ii- cooling, iii- ice formation, iv- ice melting, v- CH_4 hydrate formation, vi- injection of liquid CO_2 , vii- liquid CO_2 to gas, viii- exit CH_4 hydrate stability field, and ix- exit CO_2 hydrate stability field. Both experiments are conducted using de-ionized water and research purity gases.

(Mochizuki and Mori 2006). We estimate the initial film thickness is equal to $\sim 60 \mu\text{m}$ based on the droplet volume expansion $V_{\text{final}}/V_{\text{initial}}=1.016$ and the theoretical volume change from water to hydrate $V_{\text{hyd}}/V_{\text{w}}=1.234$ (Table 7.1). Stable P-T conditions are maintained for ~ 2 days; during this period, further hydrate growth is controlled by CH_4 diffusion through the hydrate layer (Fig. 7.4-a). The shell remains stable (Note: shell depressions were observed in hydrate-coated droplet experiments by Servio and Englezos 2003).

We flood the chamber with liquid CO_2 , displacing CH_4 gas through a vent (Fig. 7.4-b); the pressure and temperature conditions are inside the CH_4 hydrate stability field ($P=7\pm 1\text{MPa}$, $T=275\pm 1.5\text{K}$ during the short injection period). The amount of water needed to saturate the liquid CO_2 in the absence of any hydrate in the chamber is $\sim 45\text{mg}$ (based on solubility data in Table 7.3-a). We measure $\sim 15\text{mg}$ of water migration from the droplet to the surrounding liquid CO_2 in a period of 2 days; this is a form of “drying” in a CO_2 atmosphere (Fig. 7.4). Thereafter, the droplet size remains constant for ~ 4 days under stable P-T conditions ($P=6\text{MPa}$, $T=274\pm 1\text{K}$; Fig. 7.4-i). These measurements suggest a lower solubility of water in CO_2 in the presence of hydrate than the value reported in the absence of hydrate (similarly to gas solubility in water, Table 7.3-a). While we assume replacement is taking place, no CH_4 gas bubbles form in the liquid CO_2 due to the high solubility of CH_4 in CO_2 (Table 7.3-a). We depressurize the chamber gradually. The hydrate shell remains stable after CO_2 vaporizes and also across the CH_4 hydrate phase boundary. We hold stable P-T conditions above the CO_2 hydrate boundary for $\sim 30\text{min}$. Finally, we depressurize the chamber further and hydrate dissociates across the CO_2

hydrate phase boundary at $\sim 1.8\text{MPa}$ and 276.5K .

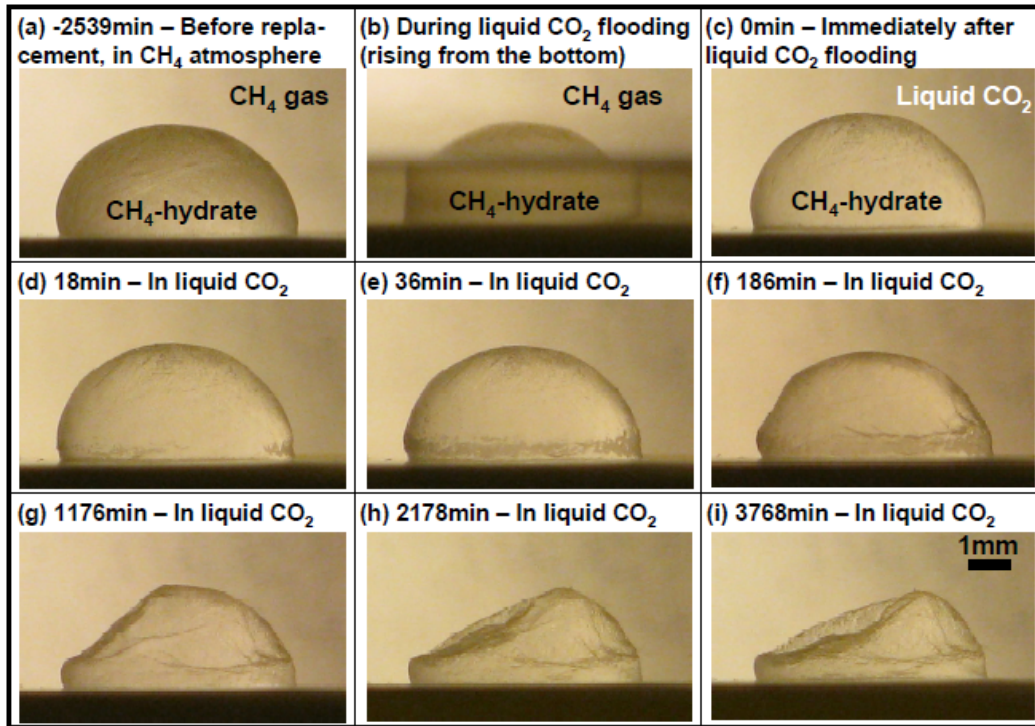


Figure 7.4. Droplet experiment: time evolution of the CH₄ hydrate shell after flooding with liquid CO₂. Pressure is 6MPa and the chamber temperature stays at $274\pm 1\text{K}$, after point (iv) in Fig. 7.3-b. This sequence of images suggests that liquid CO₂ “dries” the water either in the hydrate shell and/or inside the hydrate droplet.

Water meniscus. In this second study, the water droplet rests between two water-wet hydrophilic transparent glass surfaces, creating a cylindrically-shaped body of water similar to a water meniscus between two grains (8.7mm diameter, 1.97mm in height; and 120mg water mass). Fig. 7.3-c shows the P-T trajectory imposed during the test. The evolution of the droplet is observed through the lower plate (Fig. 7.5-a). We trigger nucleation by causing transient ice formation (Fig. 7.5-b). Methane hydrate starts forming at the interface (similar observation in Stern et al. 1998). Hydrate does not grow homogeneously but advances in the form of lobes that invade the water meniscus (Fig. 7.5-c,d – Note: needle-type growth is observed in the results reported by (Subramanian and Sloan 2002). Volume expansion during hydrate growth ($V_{\text{hyd}}/V_{\text{w}}=1.234$ - Table 7.1) causes water to flow out of the meniscus along the hydrophilic glass surfaces, readily forming a thin hydrate layer on the glass plates (Fig. 7.5-c,d,e). The hydrate growth rate inside the meniscus is between 0.05mm/hour and 0.11mm/hour. This fast growth rate suggests that gas reaches the water through cracks in the hydrate shell rather than by diffusion through the hydrate layer.

The injection of liquid CO₂ is expected to trigger CH₄-CO₂ replacement and water dissolution into the liquid CO₂ (the amount of water needed to saturate the liquid CO₂ in this chamber is 171mg, Table 7.3-a). Hence, the CO₂ hydrate film observed coating the glass plates in Fig. 7.5-f appears to be thinner (i.e., more transparent) than the CH₄ hydrate film in Fig.7.5-d-e. Once again, CH₄ gas bubbles are not observed. The lobular hydrate structure remains inside the meniscus, that is, the overall geometry of the solid hydrate mass is preserved. Depressurization from liquid CO₂ to gaseous CO₂ causes the

water dissolved in liquid CO₂ to precipitate as CO₂ hydrate on the glass plate (Fig. 7.5-g). Depressurization out of the CH₄ phase-boundary has no “observable” effect on the hydrate phase within the meniscus or coating the glass surfaces (Fig. 7.5-h). Finally, hydrate dissociates during depressurization below the CO₂ hydrate phase boundary.

Summary. These two experiments reveal marked differences in CH₄ hydrate formation behavior on hydrophilic and hydrophobic substrates, and show the significance of mutual solubilities during CH₄-CO₂ replacement. There is no visual evidence of CH₄-CO₂ replacement when the CH₄ atmosphere is changed for CO₂ gas or liquid, i.e., there is no bubbling, volume change or alterations in the solid phase. The final depressurization stage confirms the presence of CO₂ hydrate at the CO₂ hydrate dissociation boundary.

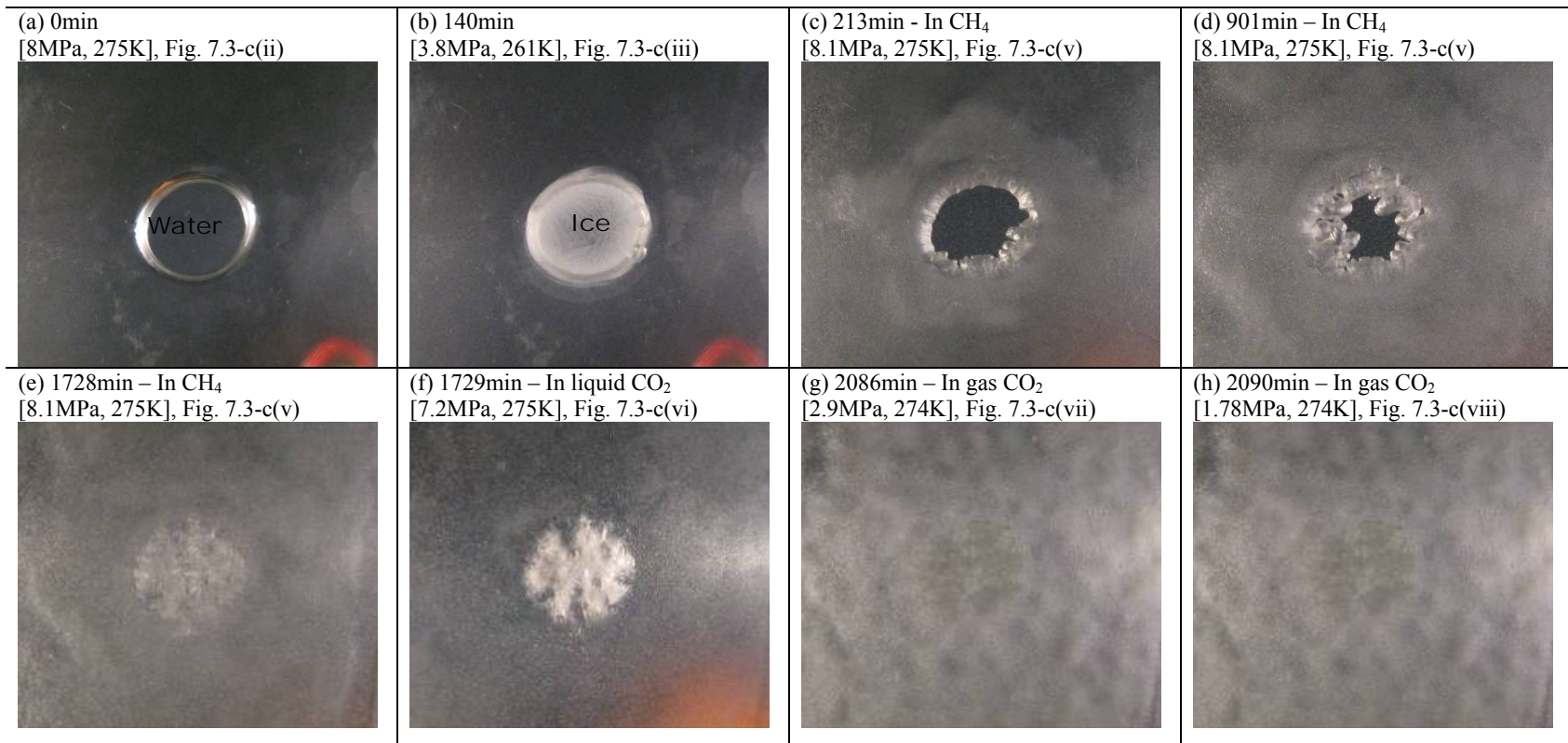


Figure 7.5. Meniscus experiment. (a) Water droplet – Scale: 8.7mm diameter, (b) Ice formation, (c)-(e) CH₄ hydrate formation and growth, (f) Injection of liquid CO₂, (g) Depressurization from liquid CO₂ to gas CO₂, (h) Image for P-T conditions outside the CH₄ hydrate stability field.

7.5 ANALYSIS – SEDIMENT SCALE IMPLICATIONS

Analyses and experimental results presented in previous sections allow us to anticipate potential thermo-hydro-mechanical coupled processes during CH₄-CO₂ replacement in hydrate bearing sediments.

7.5.1 Molecular scale CH₄-CO₂ replacement process

Molecular scale observations (Section 2), diffusion rates (Table 7.1 and 7.4), and experimental results (Table 7.5) point to a “local” solid-liquid-solid transition during CH₄-CO₂ replacement. Inside the stability field, CH₄ hydrate in equilibrium is constantly forming and breaking down at the interface, releasing and capturing CH₄ molecules (See molecular dynamics insight in Baez and Clancy 1994; Baez and Clancy 1995; Walsh et al. 2009). In a CO₂-rich medium, freed CH₄ molecules may be replaced by CO₂ molecules, forming CO₂ hydrate and releasing excess heat. This released heat causes a positive feedback by locally raising the temperature of neighboring hydrate cages towards the CH₄ hydrate phase boundary to facilitate the atomic-scale solid-liquid-solid CH₄-CO₂ replacement in a form of “chain-reaction”.

This hypothetical replacement process allows us to identify two end-member replacement scenarios. First, constant hydrate breaks down and formation makes CH₄-CO₂ replacement possible within the CH₄ hydrate stability field (zone A in Fig. 7.2); in this case, reaction rates will be strongly dependent on the contact area between CO₂ and CH₄

hydrate. Second, excess heat liberated in the CH₄-CO₂ replacement transformation may sustain a high solid-liquid-solid reaction rate; in this case we anticipate a lower reaction rate as P-T conditions are further inside the CH₄ hydrate stability field.

7.5.2 Bound for excess heat-assisted reaction within the CH₄ stability field

The second end-member is analyzed next, taking into consideration all the phases involved. We assume that local P-T conditions reach the CH₄ hydrate dissociation boundary driven by the excess heat liberated in the total reaction (Section 2, Table 7.1). How far inside the stability field can the hydrate bearing sediment be to experience this excess heat-assisted reaction?

Consider CH₄ hydrate at initial pressure P₀, temperature T₀ and surrounded by CO₂ (liquid in zones A and C; and gas in zone B, Fig. 7.2), water and the mineral structure of the host sediment. Let's also assume that all hydrate cages undergo gas replacement so that the liberated heat is proportional to the difference between the heat of dissociation of CH₄ hydrate, H^d_{CH₄hyd}[kJ/kg], and the heat of formation of CO₂ hydrate, H^f_{CO₂hyd} [kJ/kg]. We consider isobaric conditions and 100% replacement to calculate the increase in temperature ΔT from the in situ condition T₀ to the temperature T_b on the CH₄ hydrate stability boundary corresponding to pressure P₀,

$$\begin{aligned} & \left(M_{CO_2} c_{CO_2} + M_{CH_4,hyd} c_{CH_4,hyd} + M_w c_w + M_m c_m \right) T_o = \\ & \left(M_{CH_4} c_{CH_4} + M_{CO_2,hyd} c_{CO_2,hyd} + M_w c_w + M_m c_m \right) T_b - \left(H_{CO_2,hyd}^f M_{CO_2,hyd} - H_{CH_4,hyd}^d M_{CH_4,hyd} \right) \end{aligned} \quad (7.1)$$

where subscripts for specific heat c and mass M , are m for mineral and w for water. In this analysis, we do not consider changes in P-T phase boundary conditions for gas mixtures (refer to Section 2e-1). All masses M convert to volume V through the corresponding bulk densities ρ , and partial volumes are related to the total sediment volume V_T through the sediment porosity ϕ , and the volumetric fractions of hydrate S_{hyd} , water S_w , and gas S_g (CH₄ gas or CO₂ gas/liquid) in the pore space,

$$V_{hyd} = S_{hyd}\phi V_T, \quad V_w = S_w\phi V_T, \quad V_g = S_g\phi V_T, \quad V_m = (1-\phi)V_T \quad (7.2)$$

where $S_{hyd}+S_w+S_g=1$. A simple closed-form analytical expression is obtained assuming that the heat stored in CO₂ and CH₄, and hydrates is similar before and after replacement $\rho_{CO_2}S_{CO_2}\phi c_{CO_2} + \rho_{CH_4hyd}S_{hyd}\phi c_{CH_4hyd} \approx \rho_{CH_4}S_{CH_4}\phi c_{CH_4} + \rho_{CO_2hyd}S_{hyd}\phi c_{CO_2hyd}$. Then, the CH₄-CO₂ replacement rate within the sediment will be maximized if the initial temperature of the reservoir is equal or greater than,

$$T_o = T_b(P_0) - \frac{(H_{CO_2hyd}^f \rho_{CO_2hyd} - H_{CH_4hyd}^d \rho_{CH_4hyd}) S_{hyd}\phi}{\rho_{CO_2}S_{CO_2}\phi c_{CO_2} + \rho_w S_w\phi c_w + \rho_{CH_4hyd}S_{hyd}\phi c_{CH_4hyd} + (1-\phi)\rho_m c_m} \quad (7.3)$$

Numerical results are presented in Fig. 7.6 for a CH₄ hydrate volume fraction $S_{hyd}=0.5$. This equation is a lower bound for the excess heat-assisted CH₄-CO₂ replacement, since we assume that the liberated heat warms up the whole sediment mixture. The upper bound corresponds to the CH₄-CO₂ replacement for pure hydrate (line on the upper left corner in Fig. 7.6). Local heating during replacement is between these two bounds.

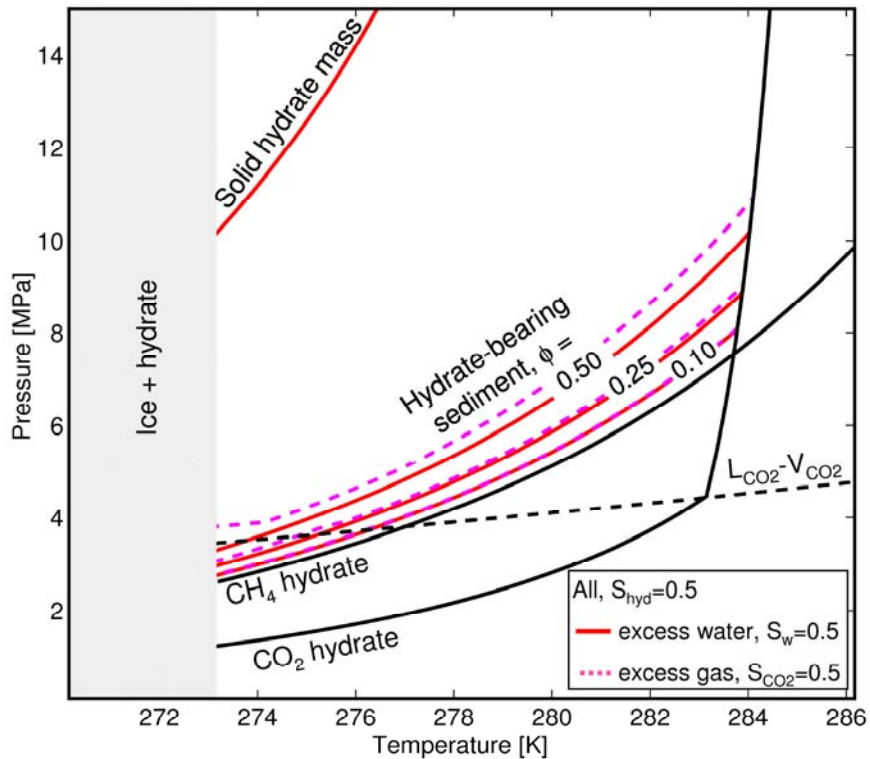


Figure 7.6. Pressure-temperature upper and lower bounds for initiating excess heat CH_4 - CO_2 hydrate replacement by raising the local temperature to the CH_4 hydrate dissociation boundary. The temperature increases due to the heat released after CH_4 hydrate dissociation and CO_2 hydrate formation. Upper bound: the reaction can begin far inside the CH_4 hydrate stability zone for a solid hydrate mass (upper bound $\sim 10\text{K}$ from the CH_4 hydrate dissociation boundary). Lower bound: the reaction must begin closer to the CH_4 hydrate phase boundary in hydrate bearing sediments where minerals and water absorb liberated heat. Bounds are computed using Equation 7.3 and parameters from Table 7.1, porosity $\phi=0.5, 0.25, 0.10$; $c_m=0.83 \text{ kJ}/(\text{kg}\cdot\text{K})$; $H_{\text{CO}_2\text{hyd}}^f=395\text{kJ}/\text{kg}$; $H_{\text{CH}_4\text{hyd}}^d=440\text{kJ}/\text{kg}$, $\rho_{\text{CO}_2\text{hyd}}=1100 \text{ kg}/\text{m}^3$, and $\rho_{\text{CH}_4\text{hyd}}=930 \text{ kg}/\text{m}^3$. Note: this analysis does not consider intermediate hydrate phase boundaries for hydrate grown from gas mixtures (Section 2e-1).

7.5.3 Hydrate dissolution in liquid CO₂

Liquid CO₂ will draw water and methane from the CH₄ hydrate until it reaches the solubility limit of water in CO₂ $y_{CO_2}^{H_2O}$ (Section 2e-2). The change in hydrate saturation in the sediment ΔS_{hyd} due to hydrate dissolution in liquid CO₂ is,

$$\Delta S_{hyd} = \left(1 - S_{hyd}\right) \left(\frac{1}{y_{CO_2}^{H_2O}} \frac{\rho_{CH_4hyd}}{\rho_{CO_2}} \frac{n \cdot m_{H_2O}}{m_{CH_4} + n \cdot m_{H_2O}} \frac{m_{CO_2}}{m_{H_2O}} + 1 \right)^{-1} \quad (7.4)$$

where the m represents molar mass, n the stoichiometric ratio, and ρ_{CH_4hyd} and ρ_{CO_2} are the mass densities of CH₄ hydrate and liquid CO₂ at the prevailing P-T conditions. A change in hydrate saturation of $\Delta S_{hyd} \sim 0.001$ is estimated for reservoir conditions $S_{hyd} < 0.3$, $P = 5$ -to- 8 MPa, and $T = 273$ -to- 278 K. While this is a small number, continuous flow of pure liquid CO₂, can cause significant hydrate dissolution, for instance near the CO₂ injection well.

7.5.4 Methane gas bubble formation

CH₄-CO₂ replacement releases CH₄ into the pore space. The critical CH₄ hydrate saturation S_{hyd}^* required to cause CH₄ bubble formation depends on the bubble point molar ratio R_{BP} for the CH₄-CO₂ fluid mixture at the specific P-T conditions. The value of S_{hyd}^* can be estimated as

$$S_{hyd}^* = \left(1 - S_w\right) \left(\frac{1}{R_{BP}} \frac{\rho_{CH_4hyd}}{\rho_{CO_2}} \frac{m_{CH_4}}{m_{CH_4} + n \cdot m_{H_2O}} \frac{m_{CO_2}}{m_{CH_4}} + \frac{\rho_{CO_2hyd}}{\rho_{CO_2}} \frac{m_{CO_2}}{m_{CO_2} + n \cdot m_{H_2O}} + 1 \right)^{-1} \quad (7.5)$$

For reservoir conditions $P=7.25\text{MPa}$ and $T=278.15\text{K}$, the bubble point is $R_{BP}=0.12$ (Donnelly and Katz 1954), and the critical hydrate saturation for gas bubble formation is $S_{hyd}^* \sim 0.21$ (See Fig. 7.7-b).

7.5.5 Fluid volume expansion during $\text{CH}_4\text{-CO}_2$ replacement

Above bubbling conditions, $\text{CH}_4\text{-CO}_2$ replacement involves either volume change at constant fluid pressure, or pressure change under isochoric conditions. Let's compute first the change in volume during hydrate formation as a function of the hydration number n , mass densities ρ , and molar masses m

$$\frac{V_{hyd}}{V_w} = \frac{m_{hyd} / \rho_{hyd}}{m_w / \rho_w} = \frac{m_g + n \cdot m_w}{n \cdot m_w} \cdot \frac{\rho_w}{\rho_{hyd}} \quad (7.6)$$

where the density of water is $\rho_w=1000\text{kg/m}^3$, and molar masses are $m_w=18\text{g/mol}$, $m_{\text{CH}_4}=16\text{g/mol}$ and $m_{\text{CO}_2}=44\text{g/mol}$. As shown in Fig.7.7-a, an initial volume of water expands by $V_{hyd}/V_w=1.234$ to form CH_4 hydrate ($n=6$, $\rho_{\text{CH}_4\text{hyd}}=930\text{kg/m}^3$), and $V_{hyd}/V_w=1.279$ to form CO_2 hydrate ($n=6$, $\rho_{\text{CO}_2\text{hyd}}=1110\text{kg/m}^3$).

The volume change of the hydrate mass during 100% $\text{CH}_4\text{-CO}_2$ replacement can be analyzed following a similar formulation and using experimentally measured macroscale quantities n and ρ (Note: ρ is a function of n). Let's assume all CH_4 in hydrate exchanges with the injected liquid CO_2 . The change in hydrate volume is:

$$\frac{V_{CO2hyd}}{V_{CH4hyd}} = \frac{44 + 18 \cdot n_{CO2}}{16 + 18 \cdot n_{CH4}} \cdot \frac{\rho_{CH4hyd}}{\rho_{CO2hyd}} \quad (7.7)$$

The volume occupied by the hydrate mass expands about 1-to-6% after CH₄-CO₂ hydrate replacement ($n_{CH4}=6$, $n_{CO2}=6$, and pressure-dependent mass densities $\rho_{CH4hyd}=910$ - 940kg/m^3 , $\rho_{CO2hyd}=1090$ - 1110kg/m^3). The change in lattice size $\sim 2.9\%$ is in agreement with this macroscale analysis (refer to values in Table 7.1).

On the other hand, released CH₄ gas after replacement occupies a volume that is strongly dependent on pressure and initial hydrate saturation. The final volume occupied by the released methane V_g^{CH4} which did not dissolve into the liquid CO₂, relative to the volume occupied by the CO₂ that became trapped in hydrate V_l^{CO2} is,

$$\frac{V_g^{CH4}}{V_l^{CO2}} = \frac{\left[\frac{\rho_{CH4hyd}}{m_{CH4}} \frac{S_{hyd} \cdot m_{CH4}}{m_{CH4} + n \cdot m_{H2O}} - \frac{R_{BP}}{m_{CO2}} \left((1 - S_{hyd}) \rho_{CO2} - \frac{\rho_{CO2hyd} \cdot S_{hyd} \cdot m_{CO2}}{m_{CO2} + n \cdot m_{H2O}} \right) \right] m_{CH4}}{S_{hyd} \frac{\rho_{CO2hyd}}{\rho_{CO2}} \frac{m_{CO2}}{m_{CO2} + n \cdot m_{H2O}}} \cdot \frac{1}{\rho_{CH4}} \quad (7.8)$$

There is a very pronounced increase in pore fluid volume associated with CH₄-CO₂ replacement at constant pressure. The volumetric ratio V_g^{CH4}/V_l^{CO2} is plotted in Fig. 7.7-b as a function of S_{hyd} for reservoir conditions $P=7.25\text{MPa}$, $T=278.15\text{K}$, $R_{BP}=0.12$ (Donnelly and Katz 1954); for example $V_g^{CH4}/V_l^{CO2} \sim 390\%$ for $S_{hyd}=50\%$. Conversely, a marked increase in fluid pressure and decrease in effective stress will take place if constant

volume is imposed during CH₄-CO₂ replacement. Field conditions will be between these two extreme scenarios. If replacement conditions result in a CH₄/CO₂ mixture, the volume of the mixture fluid can be computed using cubic equations of state (Li and Yan 2009).

7.5.6 Sediment volume change during CH₄-CO₂ replacement

A soil subjected to an increase in effective stress $\Delta\sigma'$ from an initial effective stress σ_o' to a final stress $\sigma_o'+\Delta\sigma'$ experiences a volumetric strain $\varepsilon_{vol}=C_c^* \log[(\sigma_o'+\Delta\sigma')/\sigma_o']$ that is proportional to the compression index C_c^* . The presence of hydrates stiffens the soil skeleton so that lower values of the compression index are expected for hydrate bearing sediments than for the same sediment without hydrates (Lee et al. 2010). The stiffening effect of hydrate depends on the pore habit: pore-filling (smallest effect), load-bearing and cementing (largest effect) (Waite et al. 2009). While CH₄-CO₂ replacement involves transient “local” dissociation, preliminary experimental evidence we have gathered using cementing CH₄ hydrate-bearing sands with hydrate saturation $S_{hyd}=5\text{-to-}10\%$ shows no significant change in global stiffness when wave propagation velocity data are gathered during CH₄-CO₂ gas replacement. Thus, low volumetric strains should be expected during CH₄-CO₂ replacement under free-draining flow conditions. Fluid volume change may affect sediment stability if free-draining conditions are lost during replacement. The following sequence of events may take place (Santamarina and Jang 2009): fluid volume expansion during the CH₄-CO₂ replacement causes an increase in fluid pressure, a decrease in effective stress, and a loss in sediment strength leading to shear failure, gas driven fractures, and/or collapse of the sediment skeleton.

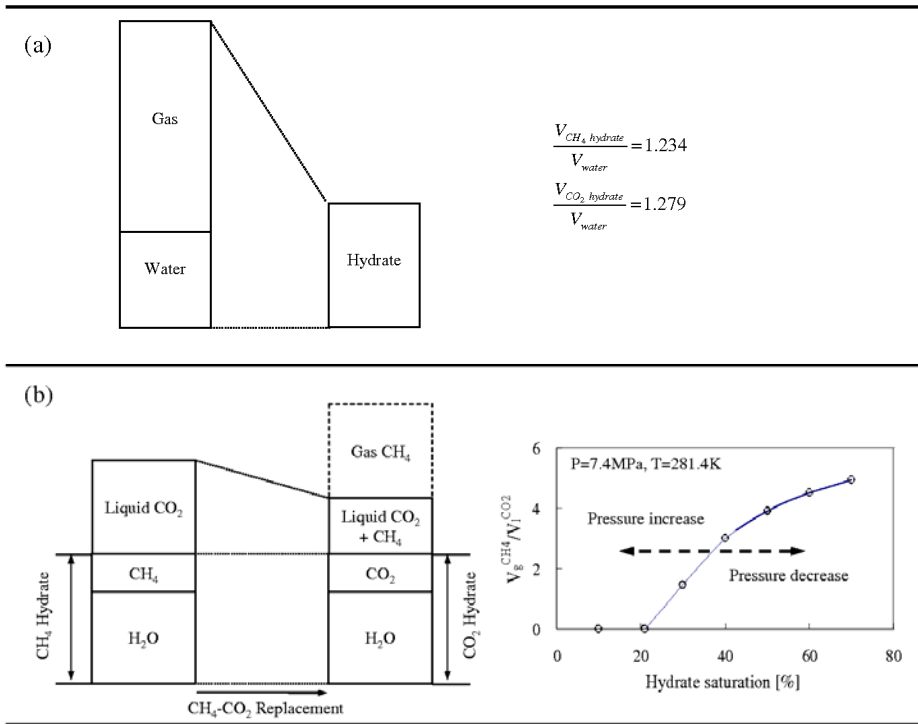


Figure 7.7. Volume change analysis. (a) During hydrate formation/dissociation, i.e. Eq. 7.7 (b) During CH₄-CO₂ replacement, i.e. Eq. 7.8 ($P=7.4\text{MPa}$, $T=281.4\text{K}$, $\rho_{CO_2}=906\text{kg/m}^3$, bubble point for CH₄/CO₂ mixture $R_{BP}=12\%$ mol CH₄ / mol CO₂).

7.5.7 Mixed fluid flow

CO₂ is considerably less viscous than water, and CO₂ will tend to produce viscous fingering in excess-water reservoirs. Some recent numerical simulations show finger-like patterns when CO₂ invades water-saturated formations (Kang et al. 2005; Qi et al. 2009), while other simulations show minimal CO₂ fingering (Chang et al. 1994). The analysis of pore scale capillary and viscous forces suggests a higher tendency to viscous fingering in the near field of the injection well where flow velocities are high (Lenormand et al. 1988).

7.5.8 Anticipated sediment-scale emergent phenomena

Four different injection scenarios are identified in Table 7.6 in terms of P-T conditions that control either liquid CO₂ or gas CO₂ injection (zones A and B in Fig. 7.2), and either excess-water (gas-limited) or excess-gas (water limited) hydrate-bearing sediments. Phenomena and properties listed above help us identify the following processes that may take place during injection:

- The release of CH₄ above the bubble point leads to gas formation $S_g > 0$ and lowers the relative permeability of the liquid phase (van Genuchten's equation as in Kleinberg et al. 2003).
- A low velocity of the invading CO₂ front, compared to the rate of CO₂ hydrate formation, will promote the growth of new CO₂ hydrate in excess-water reservoirs, occlude regions with CH₄ hydrate, prevent the direct contact of

CH₄ hydrate with CO₂, and hinder CH₄-CO₂ replacement (see numerical simulation of CO₂ hydrate clogging - data in Kang et al. 2005).

- The replacement rate in both excess-gas and excess-water reservoirs will be controlled by the spatial distribution of CO₂ during injection and the replacement reaction rate.

Clogging by CO₂ hydrate formation can be analyzed by comparing the velocity of the invading CO₂ advective front and the growth velocity of CO₂ hydrate at the water-CO₂ interface. The advection fluid velocity in pores v_A [m/s] = $q/(2\pi r H_r \phi)$ is determined by the injection flow rate q [m³/s], the distance from the well to the front r , the hydrate-bearing reservoir thickness H_r [m], and the sediment porosity ϕ . The velocity of diffusion-controlled growth of the hydrate plug in pores is approximately $v_D = D/\delta$, where D is the diffusion coefficient [m²/s] of CO₂ through hydrate and δ [m] the length of the hydrate plug. The ratio of these two velocities $v_D/v_A = 2\pi D r H_r \phi / (\delta q)$ determines whether hydrate clogging ($v_D/v_A \gg 1.0$) or unconstrained advection ($v_D/v_A \ll 1.0$) will take place. For example, clogging is not anticipated in sandy sediments and sandstones near the injection well during continuous injection, (assuming $\delta \sim 10^{-4}$ m, i.e., the plug length is similar to the pore size). However, a stagnant CO₂ fluid front will promote hydrate formation and a differential pressure $p_{CO_2} - p_w$ will be needed to break the CO₂ hydrate seal in order to continue injecting CO₂. Assuming cylindrical pore geometry, the additional CO₂ pressure is $p_{CO_2} - p_w = 4\beta\delta/d$ where β is the hydrate-mineral bonding strength, d is the pore diameter and δ the plug thickness. For plugs $d \cong \delta$ and a bonding strength $\beta \sim 250$ kPa, the differential pressure to re-initiate pumping is $p_{CO_2} - p_w \sim 1$ MPa.

The complex interaction among coexisting processes may give rise to emergent bifurcation phenomena such as viscous fingering and gas-driven fractures. On the other hand, self-homogenizing effects may also arise; for example, CH₄ gas production during CO₂ injection will reduce the local permeability and hinder the formation of CO₂ fingers.

Table 7.6. Anticipated sediment scale phenomena during CH₄-CO₂ gas replacement

		Reservoir Type	
		Gas-limited, excess-water	Water-limited, excess-gas
Injected fluid	Gas CO ₂	<ul style="list-style-type: none"> Gas buoyancy affects invasion^a Slow gas replacement rate due to low gas activity^b Expect viscous fingering of CO₂ gas^{c,d} 	<ul style="list-style-type: none"> CH₄ hydrate is found at contacts^e Low hydrate volume expansion (1-to-6%)^{*1} High CO₂ gas permeability CO₂ and CH₄ mix, and flow together^f
	Liquid CO ₂	<ul style="list-style-type: none"> Released CH₄ gas lowers the mixture bulk modulus (if above bubble point concentration)^g Large fluid volume expansion if released methane exceeds bubble point concentration^{*2} Expect viscous fingering of liquid CO₂^{c,d} 	<ul style="list-style-type: none"> Some of the water in CH₄ hydrate will dissolve into the liquid CO₂ and the final hydrate saturation will decrease; in fact, liquid CO₂ might “dry” hydrate near the injection well^{*3} Some CH₄ gas will remain trapped in the sediment
	Either gas or liquid CO ₂	<ul style="list-style-type: none"> Replacement rate is limited by spatial invasion of gas/liquid CO₂ At low injection rates or due to flow interruptions, CO₂ will react with the excess water to form hydrate during injection, plugging the formation and shielding CH₄ hydrate at reservoir and pore scales^{b,c} Hydrate saturation increases and hydraulic conductivity decreases^h Water acidifiesⁱ 	<ul style="list-style-type: none"> The sediment is water limited so it does not clog by forming new hydrate

a - (Lu et al. 2009); b - (McGrail et al. 2007); c - (Kang et al. 2005); d - (Lenormand et al. 1988); e - (Waite et al. 2009); f - (Donnelly and Katz 1954); g - (Span and Wagner 1996; Trusler and Zarari 1992); h - (Kleinberg et al. 2003); i - (Kneafsey and Pruess 2010); *1–this study, equation 7.7; *2 – this study, equation 7.8; *3 – this study, section 4, Fig. 7.4.

7.6 CONCLUSIONS

The replacement of CH₄ by CO₂ in hydrate bearing sediments involves multiple coexisting processes, such as mass and heat transport, heat liberation, dissolution, gas production, and fluid volume change.

The CH₄ hydrate cage must separate to release the CH₄ molecule and trap the CO₂ molecule. This transient and local solid-liquid-solid transition within the stability field is assisted by the excess heat liberated during CH₄-CO₂ replacement and can extend as far as ~10K inside the stability field. The presence of minerals, water, and excess gas can limit this self-sustaining reaction to within ~3K of the CH₄ hydrate boundary. While available data are limited, experimental and theoretical considerations suggest that replacement rates increase near the CH₄ hydrate phase boundary, with increasing pore fluid pressure until the CO₂ liquefies, and, when CH₄ hydrate masses are small so the surface available for CO₂ exchange is high.

New experimental results highlight the high solubility of water and CH₄ in liquid CO₂. Hydrate forming water dissolves into liquid CO₂, so that lower hydrate saturation is expected after CH₄-CO₂ replacement in water-limited reservoirs. The transient in hydrate stiffness that should accompany local solid-liquid-solid CH₄-CO₂ replacement has a very small effect on macro-scale skeleton stiffness and the sediment should experience low volumetric strains during CH₄-CO₂ replacement under drained conditions.

Processes and properties reviewed in this manuscript allow us to anticipate various reservoir scale phenomena during CH₄-CO₂ replacement, including: potential decrease in water saturation, decrease in the liquid relative permeability, pronounced increase in fluid volume when a CH₄ gas phase is formed, CO₂ hydrate clogging when the velocity of the invading front is low and there is enough water to supersaturate the CO₂, and the possibility of CO₂ fingering leading to CH₄ hydrate occlusion within the reservoir. Excess-gas methane hydrate reservoirs should be more amenable to CH₄-CO₂ replacement because of high permeability to CO₂, large interface between CH₄ hydrate and CO₂, and no early CO₂ hydrate clogging. Volume-pressure changes associated to CH₄-CO₂ replacement in excess-water reservoirs may cause increase in fluid pressure, decrease in effective stress and strength loss, volume expansion, and gas-driven fractures if a CH₄ gas phase develops and the permeability is low enough to prevent pressure dissipation.

CHAPTER VIII

CONCLUSIONS

This research addressed the fundamental understanding of hydrate-bearing sediments, including hydrate formation and growth in pores, hydrate tensile and bonding strengths, the mechanical response of hydrate bearing sediments using DEM numerical simulations, gas production from hydrate-bearing sediments, and CH₄-CO₂ replacement in hydrate-bearing sediments. Unique experimental studies were implemented using unprecedented high-pressure chambers that allowed for the observation of processes including the measurement of mechanical and electrical properties during hydrate formation, dissociation and exchange reactions. Experimental results were analyzed using physical, chemical and mechanical concepts and were complemented with analytical solutions and numerical simulations. The main conclusions follow.

Hydrate formation and growth in pores.

- Initial hydrate formation is fast and consumes gas dissolved in water during the induction time. Thereafter, diffusion at the tip of the hydrate mass causes hydrate dissolution. Such transient formation-dissolution cycles are readily seen during the early stages of hydrate formation.
- Hydrate growth is controlled by gas diffusion through the hydrate shell that separates water and gas. Faster than anticipated growth rates suggest the presence of discontinuities in the hydrate shell, probably due to liquid-to-

hydrate volume expansion.

- Hydrate growth in capillaries does not advance homogeneously as a planar front but in the form of lobes that invade the water phase; this topology increases surface area and favors growth in a diffusion-limited methane transport.
- Ion exclusion during hydrate formation leads to an increase in ionic concentration in trapped water and hindered hydrate growth. The resulting gas-hydrate-brine system can remain stable due to the low diffusion of ions out of the trapped water through the hydrate shell.

Hydrate adhesive and tensile strengths.

- A hydrate-mineral system fails in tension either through the tensile failure of the hydrate mass, or by hydrate debonding from the mineral substrate. Debonding failure prevails in mica. When calcite is involved, CH₄ and CO₂ hydrates fail in tension while THF hydrate and ice debond.
- The adhesive/tensile strengths of CH₄ and CO₂ hydrates range between 150- and-200 kPa.
- Numerical FEM simulation results show the possibility of local hydrate dissociation during tensile loading.
- Micromechanical analyses show that the tensile/debonding strength determines the Mohr-Coulomb cohesive intercept.

Stress-strain response of hydrate-bearing sediments.

- The strength properties of hydrate bearing sediments depend on the hydrate pore habit.
- Distributed hydrate-bearing sediments exhibit high dilation at low confinement. A cohesive intercept that is a function of hydrate saturation is obtained when the Coulomb failure envelope is extrapolated to the origin. Yet, hydrate saturation has almost no effect on the critical state friction ϕ_{cs} .
- Sediments with patchy hydrate saturation exhibit delayed dilation until a strain-level that is comparable to the strain at peak dilation in hydrate-free sediments. There is a significant increase in critical state friction angle and there is no cohesive intercept in the p' - q projection.
- Hydrate particles bonded onto the mineral surface contribute to increased shear resistance by contiguous particles being bonded together, and by promoting rotational frustration. The strong, hydrate-saturated patches force the development of tortuous rather than planar shear planes and higher energy is required to shear the specimen, i.e. higher friction angle.
- The stiffness of hydrate-bearing sediments can be expressed using the sum of a stress-dependent hydrate-free sediments stiffness and a hydrate dependent term which is a function of hydrate saturation S_h , initial porosity n and effective confining stress σ'_o .
- Hydrate dissociation under different reservoir boundary conditions leads to volume contraction and/or stress relaxation. Pronounced shear strains develop if the hydrate-bearing sediment is subjected to deviatoric loading during

dissociation.

Emergent phenomena during gas production from hydrate-bearing sediments.

- Water injection into water-limited sediments triggers hydrate nucleation. Conversely, gas-free water advection into water-saturated hydrate-bearing sediments dissolves hydrate.
- The presence of fines in otherwise clean sands can lead to fines migration and clogging. During dissociation, gas bubbles grow and displace fines. The fines content on the bubble surface gradually increases; eventually fines clog pore throats. Therefore, the expanding gas bubble may push away the skeletal particles, creating a vuggy structure. This is a precursor for gas-driven fracture formation.
- The evolution of the shear wave velocity provides insightful information related to the sediment stress-hydrate history. The hydrate saturation can be obtained with the measured S-wave velocities using semi-empirical relationships.

CH₄-CO₂ replacement

- A self-sustaining CH₄-CO₂ replacement reaction using the excess heat that is liberated is expected as far as ~3K inside the stability field when minerals, water, and excess gas are present.
- While CH₄-CO₂ replacement requires the opening of the hydrate cage (i.e. a solid-liquid-solid transformation), both electrical resistance and relative stiffness measurement suggest that CH₄-CO₂ replacement occurs locally and gradually so

that the overall hydrate mass remains solid. Therefore, no stiffness loss should be expected at the sediment scale.

- The newly formed CO₂ hydrate shell must be either fractured or porous in order to allow for the high exchange rates that are experimentally observed
- Replacement rates increase near the CH₄ hydrate phase boundary, with increasing pore fluid pressure until the CO₂ liquefies, and, when CH₄ hydrate masses are small so the surface available for CO₂ exchange is high.
- Lower hydrate saturation is expected after CH₄-CO₂ replacement in water-limited reservoirs because hydrate forming water dissolves into liquid CO₂.
- We anticipate various reservoir scale phenomena during CH₄-CO₂ replacement, including: potential decrease in water saturation, decrease in the liquid relative permeability, pronounced increase in fluid volume when a CH₄ gas phase is formed, CO₂ hydrate clogging when the velocity of the invading front is low and there is enough water to supersaturate the CO₂, and the possibility of CO₂ fingering leading to CH₄ hydrate occlusion within the reservoir.
- Excess-gas methane hydrate reservoirs should be more amenable to CH₄-CO₂ replacement because of high permeability to CO₂, large interface between CH₄ hydrate and CO₂, and no early CO₂ hydrate clogging.
- Volume-pressure changes associated to CH₄-CO₂ replacement in excess-water reservoirs may cause increase in fluid pressure, decrease in effective stress and strength loss, volume expansion, and gas-driven fractures if a CH₄ gas phase develops and the permeability is low enough to prevent pressure dissipation.

REFERENCES

- Adamson, A. W. (1997). "Physical Chemistry of Surface." *John Wiley & Sons, New York, 6th edition.*
- Adisasmito, S., Frank, R. J., and Sloan, E. D. (1991). "Hydrates of carbon-dioxide and methane mixtures." *Journal of Chemical and Engineering Data*, 36(1), 68-71.
- Ahmadi, G., Ji, C., and Smith, D. H. (2004). "Numerical solution for natural gas production from methane hydrate dissociation." *Journal of Petroleum Science and Engineering*, 41(4), 269-285.
- Anderson, G. K. (2003). "Enthalpy of dissociation and hydration number of carbon dioxide hydrate from the Clapeyron equation." *Journal of Chemical Thermodynamics*, 35(7), 1171-1183.
- Anderson, G. K. (2004). "Enthalpy of dissociation and hydration number of methane hydrate from the Clapeyron equation." *Journal of Chemical Thermodynamics*, 36(12), 1119-1127.
- Austegard, A., Solbraa, E., De Koeijer, G., and Møltnvik, M. J. (2006). "Thermodynamic models for calculating mutual solubilities in H₂O-CO₂-CH₄ mixtures." *Chemical Engineering Research and Design*, 84(9), 781-794.
- Aya, I., Yamane, K., and Nariai, H. (1997). "Solubility of CO₂ and density of CO₂ hydrate at 30 MPa." *Energy*, 22(2-3), 263-271.
- Baez, L. A., and Clancy, P. (1994). "Computer-simulation of the crystal-growth and dissolution of natural-gas hydrates." International Conference on Natural Gas Hydrates, E. D. Sloan, J. Happel, and M. A. Hnatow, eds., 177-186.
- Baez, L. A., and Clancy, P. (1995). "The kinetics of crystal-growth and dissolution from the melt in Lennard-Jones systems." *Journal of Chemical Physics*, 102(20), 8138-8148.
- Belogol'skii, V. A., Sekoyan, S. S., Samorukova, L. M., Levtsov, V. I., and Stefanov, S. R. (2002). "Temperature and pressure dependence of the speed of sound in seawater." *Measurement Techniques*, 45(8), 879-886.
- Bradshaw, A., and Schleicher, K. E. (1970). "Direct measurement of thermal expansion of sea water under pressure." *Deep Sea Research*, 17(4), 691-698.
- Braga, D., Grepioni, F., and Orpen, A. G. (1999). *Crystal engineering: From molecules and crystals to materials*, Kluwer Academic Publishers.
- Chang, Y. B., Lim, M. T., Pope, G. A., and Sepehrnoori, K. (1994). "CO₂ flow patterns under multiphase flow - heterogeneous field-scale conditions." *SPE Reservoir*

- Engineering*, 9(3), 208-216.
- Churaev, N. V. (2004). "Mass transfer in frozen porous bodies." *Colloid Journal*, Vol. 66(No. 6), pp. 751-755.
- Circone, S., Kirby, S. H., and Stern, L. A. (2005). "Direct measurement of methane hydrate composition along the hydrate equilibrium boundary." *Journal of Physical Chemistry B*, 109(19), 9468-9475.
- Circone, S., Stern, L. A., and Kirby, S. H. (2004). "The role of water in gas hydrate dissociation." *Journal of Physical Chemistry B*, 108(18), 5747-5755.
- Cochonat, P., Cadet, J. P., Lallemand, S. J., Mazzotii, S., Nouze, H., Fouchet, C., and Foucher, J. P. (2002). "Slope Instability and Gravity Processes in Fluid Migration and Tectonically Active Environment in the Eastern Nankai Accretionary Wedge (KAIKO-Tokai'96 cruise)." *Marine Geology*, 187, 1-2, 193-202.
- Collett, T. S. (2002). "Energy resource potential of natural gas hydrates." *A.A.P.G. Bulletin*, 86(11), 1971-1992.
- Currier, J. H., and Schulson, M. (1982). "The tensile strength of ice as a function of grain size." *Acta mecall*, 30, 1511.
- Davies, S. R., Lachance, J. W., Sloan, E. D., and Koh, C. A. "A novel approach to measuring methane diffusivity through a hydrate film using differential scanning calorimetry." *6th International conference on gas hydrates*, Vancouver, British Columbia, Canada.
- Demurov, A., Radhakrishnan, and Trout, B. L. (2002). "Computations of diffusivities in ice and CO₂ clathrate hydrate via molecular dynamics and Monte Carlo simulations." *Journal of Chemical Physics*, 116(2), 702-709.
- Donnelly, H. G., and Katz, D. L. (1954). "Phase Equilibria in the Carbon Dioxide–Methane System." *Industrial and Engineering Chemistry*, 46(3), 511-517.
- Duan, S., and Sun, R. (2006). "A model to predict phase equilibrium of CH₄ and CO₂ clathrate hydrate in aqueous electrolyte solutions." *American Mineralogist*, 91, 1346-1354.
- Duan, Z. H., and Sun, R. (2003). "An improved model calculating CO₂ solubility in pure water and aqueous NaCl solutions from 273 to 533 K and from 0 to 2000 bar." *Chemical Geology*, 193(3-4), 257-271.
- Dunk, R. M., Brewer, P. G., Peltzer, E. T., Walz, P. M., Hester, K. C., and Sloan, E. D. "The exchange reaction between methane hydrate and carbon dioxide: an oceanic feasibility test." *American Geophysical Union, Fall Meeting, Abstract #MR43A-1070*.

- Durham, W. B., Kirby, S. H., Stern, L. A., and Zhang, W. (2003a). "The strength and rheology of methane clathrate hydrate." *Journal of geophysical research*, 108(B4), 2182.
- Durham, W. B., Stern, L. A., and Kirby, S. H. (2003b). "Ductile flow of methane hydrate." *Canadian Journal of Physics*, 81, 373-380.
- Ebinuma, T., Kamata, Y., Minagawa, H., Ohmura, R., Nagao, J., and Narita, H. (2005). "Mechanical properties of sandy sediment containing methane hydrate." *Proceeding of the fifth international Conference on Gas-Hydrate, June 12-16, 2005. Trondheim, Norway*.
- Espinoza, D. N., and Santamarina, J. C. (2010). "Water-CO₂-mineral systems: interfacial tension, contact angle and diffusion – Implications to CO₂ geological storage." *Water Resources Research - In Press*, doi:10.1029/2009WR008634.
- Fan, X., Ten, P., Clarke, C., Bramley, A., and Zhang, Z. (2003). "Direct measurement of the adhesive force between ice particles by Micromanipulation." *Powder Technology* 131, 105-110.
- Fenghour, A., Wakeham, W. A., and Vesovic, V. (1998). "The viscosity of carbon dioxide." *Journal of Physical and Chemical Reference Data*, 27(1), 31-44.
- Fletcher, N. H. (1969). "Active sites and ice crystal nucleation." *Journal of the Atmospheric Sciences*, 26(6), 1266.
- Folas, G. K., Froyna, E. W., Lovland, J., Kontogeorgis, G. M., and Solbraa, E. (2007). "Data and prediction of water content of high pressure nitrogen, methane and natural gas." *Fluid Phase Equilibria*, 252(1-2), 162-174.
- Freer, E. M., Selim, M. S., and D., S. E. (2001). "Methane hydrate film growth kinetics." *Fluid Phase Equilibria* 185, 65-75.
- Galashev, A. E., Chukanov, V. N., Novruzov, A. N., and Novruzova, O. A. (2006). "Molecular-dynamic calculation of spectral characteristics of absorption of infrared radiation by (H₂O)(j) and (CH₄)(i)(H₂O)(n) clusters." *High Temperature*, 44(3), 364-372.
- Garg, S., J, P., Katoh, A., Baba, K., and Fujii, T. (2008). "A mathematical model for the formation/dissociation of methane hydrates in the marine environment." *Journal of Geophysical Research*; 113:B01201.
- Gayet, P., Dicharry, C., Marion, G., Graciaa, A., Lachaise, J., and Nesterov, A. (2005). "Experimental determination of methane hydrate dissociation curve up to 55MPa by using a small amount of surfactant as hydrate promoter." *Chemical engineering science*, 60, 5751-5758.
- Goldfarb, D. L., Fernandez, D. P., and Corti, H. R. (1999). "Dielectric and volumetric

- properties of supercritical carbon dioxide(1) plus methanol(2) mixtures at 323.15 K." *Fluid Phase Equilibria*, 158, 1011-1019.
- Guimaraes, M. S., Valdes, J. R., Palomino, A. M., and Santamarina, J. C. (2007). "Aggregate production: Fines generation during rock crushing." *International journal of mineral processing*, 81, 237-247.
- Handa, Y. P. (1986). "Compositions, enthalpies of dissociation, and heat-capacities in the range 85-K to 270-K for clathrate hydrates of methane, ethane, and propane, and enthalpy of dissociation of isobutane hydrate, as determined by a heat-flow calorimeter." *Journal of Chemical Thermodynamics*, 18(10), 915-921.
- Hashemi, S., Macchi, A., Bergeron, S., and Servio, P. (2006). "Prediction of methane and carbon dioxide solubility in water." *Fluid Phase Equilibria*, 246(1-2), 131-136.
- Helgerud, M. B., Waite, W. F., Kirby, S. H., and Nur, A. (2009). "Elastic wave speeds and moduli in polycrystalline ice Ih, sI methane hydrate, and sII methane-ethane hydrate." *Journal of Geophysical Research-Solid Earth*, 114.
- Hirohama, S., Shimoyama, Y., Wakabayashi, A., Tatsuta, S., and Nishida, N. (1996). "Conversion of CH₄-hydrate to CO₂-hydrate in liquid CO₂." *Journal of Chemical Engineering of Japan*, 29(6), 1014-1020.
- Hornbach, M. J., Saffer, D. M., and Holbrook, W. S. (2004). "Critically Pressure Free-Gas Reservoirs Below Gas-Hydrate Provinces." *Nature*, 427(6970), 142-144.
- Husebo, J., Graue, A., Kvamme, B., Stevens, J., Howard, J. J., and Baldwin, B. A. (2008). "Experimental investigation of methane release from hydrate formation in sandstone through both hydrate dissociation and CO₂ sequestration." *Proceedings of the 6th International Conference on Gas Hydrates, Vancouver, British Columbia, CANADA*.
- Hyodo, M., Hyde, A. F. L., Nakata, Y., Yoshimoto, N., Fukunaga, M., Kubo, K., Nanjo, Y., Matsuo, T., and Nakamura, K. (2002). "Triaxial compressive strength of methane hydrate." *Proceeding of the twelfth (2002) international offshore and polar engineering conference, Kitakyusu, Japan, May 26-31, 2002*.
- Hyodo, M., Nakata, Y., Yoshimoto, N., and Yoneda, J. (2008). "Shear strength of methane hydrate bearing sand and its deformation during dissociation of methane hydrate." *Proceedings of Deformation characteristics of Geomaterials, 2008 IS Atlanta*.
- Ikeda-Fukazawa, T., Kawamura, K., and Hondoh, T. (2004). "Mechanism of Molecular Diffusion in Ice Crystals." *Molecular Simulation*, Vol. 30(13-15), 973-979.
- Israelachvili, J. (1991). *Intermolecular and surface forces, 2nd ed.*, Academic Press, London.
- Javan, M. M., Volat, C., and Farzaneh, M. (2006). "A new method for measuring ice

- adhesion strength at an ice–substrate interface." *Hydrological processes*, 20, 645-655.
- Jellinek, H. H. G. (1959). "Adhesive properties of ice." *Journal of colloid Science*, Vol. 14, 268-280.
- Jung, J. W., Espinozam, D. N., and Santamarina, J. C. (2010). "Properties and Phenomena Relevant to CH₄-CO₂ Replacement in Hydrate Bearing Sediments." *Journal of Geophysical Research - Solid Earth*, In press.
- Jung, J. W., and Santamarina, J. C. (2010a). "CH₄-CO₂ replacement in Hydrate-bearing sediments: A pore-scale study." *Geochemistry Geophysics Geosystems*, In press.
- Jung, J. W., and Santamarina, J. C. (2010b). "Hydrate adhesive and tensile strengths."
- Kamath, V. A., Mutalik, P. N., Sira, J. H., and Patil, S. L. (1991). "Experimental study of brine injection and depressurization methods for dissociation of gas hydrates." *SPE Formation Evaluation*, 6(4), 477-484.
- Kampel, G., Goldsztein, G. H., and Santamarina, J. C. (2008). "Plugging of porous media and filters: maximum clogged porosity." *Applied physics letters*, 92, 084101:1-3.
- Kang, Q. J., Tsimpanogiannis, I. N., Zhang, D. X., and Lichtner, P. C. (2005). "Numerical modeling of pore-scale phenomena during CO₂ sequestration in oceanic sediments." *Fuel Processing Technology*, 86(14-15), 1647-1665.
- Kashchiev, D., and Firoozabadi, A. (2002). "Nucleation of gas hydrates." *Journal of Crystal Growth*, 243(3-4), 476-489.
- Kawamura, T., Ohtake, M., Sakamoto, Y., Yamamoto, Y., Haneda, H., Komai, T., and Higuchi, S. (2009). "Gas recovery from gas hydrate bearing sediments by inhibitor or steam injection combined with depressurization." *International offshore and polar engineering conference, Osaka, Japan, Jun. 21-26*.
- Kayen, R. E., and Lee, H. J. (1991). "Pleistocene Slope Instability of Gas Hydrate-Laden Sediment on the Beaufort Sea Margin." *Marine Geotechnology*, 10, 125-141.
- Kieft, H., Clouter, M. J., and Gagnon, R. E. (1985). "Determination of acoustic velocities of clathrate hydrates by brillouin spectroscopy." *Journal of Physical Chemistry*, 89(14), 3103-3108.
- Kim, H. C., Bishnoi, P. R., Heidemann, R. A., and Rizvi, S. S. H. (1987). "Kinetics of methane hydrate decomposition." *Chemical Engineering Science*, 42(7), 1645-1653.
- Klapp, S. A., Hemes, S., Klein, H., Bohrmann, G., MacDonald, I., and Kuhs, W. F. (2010). "Grain size measurements of natural gas hydrates." *Marine Geology*, 274(1-4), 85-94.

- Klapp, S. A., Klein, H., and Kuhs, W. F. (2007). "First determination of gas hydrate crystallite size distributions using high-energy synchrotron radiation." *Geophys. Res. Lett.*, 34(13), L13608.
- Klapproth, A., Goreschnik, E., Staykova, D., Klein, H., and Kuhs, W. F. (2003). "Structural studies of gas hydrates." *Canadian Journal of Physics*, 81(1-2), 503-518.
- Kleinberg, R. L., Flaum, C., Griffin, D. D., Brewer, P. G., Malby, G. E., Peltzer, E. T., and Yesinowski, J. P. (2003). "Deep sea NMR: Methane hydrate growth habit in porous media and its relationship to hydraulic permeability, deposit accumulation, and submarine slope stability." *Journal of Geophysical Research-Solid Earth*, 108(B10).
- Kneafsey, T. J., and Pruess, K. (2010). "Laboratory Flow Experiments for Visualizing Carbon Dioxide-Induced, Density-Driven Brine Convection." *Transport in Porous Media*, 82(1), 123-139.
- Kneafsey, T. J., Tomutsa, L., Taylor, C. E., Gupta, A., Moridis, G., Freifeld, B., and Seol, Y. (2005). "Methane hydrate formation and dissociation in a partially saturated sand." *American Chemical Society, Division of Petroleum Chemistry, Preprints*, 50(1), 33-35.
- Komai, T., Yamamo, Y., and Ohga, K. "Dynamics of reformation and replacement of CO₂ and CH₄ gas hydrates." *Gas Hydrate: Challenge for the future*, 272-280.
- Kono, H.O., Narasimhan, S., Song, F., and Smith, D. H. (2002). "Synthesis of methane gas hydrate in porous sediments and its dissociation by depressurizing." *Power technology*, 122, 239-246.
- Kvamme, B., Graue, A., Buanes, T., Kuznetsova, T., and Ersland, G. (2007). "Storage of CO₂ in natural gas hydrate reservoirs and the effect of hydrate as an extra sealing in cold aquifers." *International Journal of Greenhouse Gas Control*, 1(2), 236-246.
- Kvenvolden, K. A. (1988). "Methane hydrate -- A major reservoir of carbon in the shallow geosphere." *Chemical Geology*, 71(1-3), 41-51.
- Kvenvolden, K. A. (1999). "Potential Effects of Gas Hydrate on Human Welfare." *Proceedings of National Academy of Sciences*, Sciences, 96 (7), Irvine, CA, November 8-9, 3420-3426.
- Kwon, T. H., Cho, G. C., and Santamarina, J. C. (2008). "Gas hydrate dissociation in sediments: Pressure temperature evolution." *Geochem. Geophys. Geosyst.*, 9, Q03019, doi:10.1029/2007GC001920.
- Lee, J. Y., Santamarina, J. C., and Ruppel, C. (2010). "Volume change associated with formation and dissociation of hydrate in sediment." *Geochem. Geophys. Geosyst.*, 11(3), Q03007.

- Lenormand, R., Touboul, E., and Zarcone, C. (1988). "Numerical-models and experiments on immiscible displacements in porous-media." *Journal of Fluid Mechanics*, 189, 165-187. doi:10.1017/S0022112088000953.
- Li, H., and Yan, J. (2009). "Evaluating cubic equations of state for calculation of vapor-liquid equilibrium of CO₂ and CO₂-mixtures for CO₂ capture and storage processes." *Applied Energy*, 86(6), 826-836.
- Lin, W., Chen, G. J., Sun, C. Y., Guo, X. Q., Wu, Z. K., Liang, M. Y., T., C. L., and Yang, L. Y. (2004). "Effect of surfactant on the formation and dissociation kinetic behavior of methane hydrate." *Chemical engineering science*, 59, 4449-4455.
- Linga, P., Haligva, C., Nam, S. C., Ripmeester, J. A., and Englezon, P. (2009a). "Recovery of methane from hydrate formed in a variable volume bed of silica sand particles." *Energy & Fuels*, 23, 5508-5516.
- Linga, P., Haligva, C., Nam, S. C., Ripmeester, J. A., and Englezos, P. (2009b). "Gas hydrate formation in a variable volume bed of silica sand particles." *Energy & Fuels*, 23, 5496-5507.
- Link, D. D., Ladner, E. P., Elsen, H. A., and Taylor, C. E. (2003). "Formation and dissociation studies for optimizing the uptake of methane by methane hydrates." *Fluid Phase Equilibria*, 211, 1-10.
- Lu, C., Han, W. S., Lee, S. Y., McPherson, B. J., and Lichtner, P. C. (2009). "Effects of density and mutual solubility of a CO₂-brine system on CO₂ storage in geological formations: "Warm" vs. "cold" formations." *Advances in Water Resources*, 32(12), 1685-1702.
- Makogon, Y. (1997). *Hydrates of hydrocarbons*, PennWell Books, Tulsa, Okla.
- Marshall, S. J., Bayne, S. C., Baier, R., Tomsia, A. P., and Marshall, G. W. (2010). "A review of adhesion science." *Dental Materials*, 26(2), e11-e16.
- Maslin, M., Owen, M., Day, S., and Long, D. (2004). "Linking Continental-Slope Failures and Climate Change: Testing the Clathrate Gun Hypothesis." *Geology*, 32(1), 53-56.
- Maslova, M. V., Gerasimova, L. G., and Forsling, W. (2004). "Surface Properties of Cleaved Mica." *Colloid Journal*, 66(3), 322-328.
- Masoudi, R., Tohidi, B., Danesh, A., Todd, A. C., Anderson, R., Burgass, R. W., and Yang, J. (2005). "Measurement and prediction of gas hydrate and hydrated salt equilibria in aqueous ethylene glycol and electrolyte solutions." *Chemical Engineering Science*, 60(15), 4213-4224.
- Masui, A., Haneda, H., Ogata, Y., and Aoki, K. (2005a). "Effect of methane hydrate formation on shear strength of synthetic methane hydrate sediments." *Proceeding*

of the fifteenth (2005) international offshore and polar engineering conference, Seoul, Korea, June 19-24, 2005.

- Masui, A., Haneda, H., Ogata, Y., and Aoki, K. (2005b). "The effect of saturation degree of methane hydrates on the shear strength of synthetic methane hydrate sediments." *Proceeding of the fifth international Conference on Gas-Hydrate, June 12-16, 2005. Trondheim, Norway.*
- McGrail, B. P., Schaef, H. T., White, M. D., Zhu, T., Kulkarni, A. S., Hunter, R. B., Patil, S. L., Owen, A. T., and Martin, P. F. (2007). "Using Carbon Dioxide to Enhance Recovery of Methane from Gas Hydrate Reservoirs: Final Summary Report. ." *PNNL-17035., Pacific Northwest National Laboratory operated by Battelle Memorial Institute for the U.S. Department of Energy, Oak Ridge, TN.*
- Megaw, H. D. (1973). "Crystal structures: A working Approach." *Studies in physics and chemistry, W.B. Saunders Company.*
- Milkov, A. V. (2004). "Global estimates of hydrate-bound gas in marine sediments: how much is really out there?" *Earth-Science Reviews*, 66(3-4), 183-197.
- Millero, F. J., and Poisson, A. (1981). "International one-atmosphere equation of state of seawater " *Deep-Sea Reserach*, 28(6A), 625-629.
- Mochizuki, T., and Mori, T. H. (2006). "Clathrate hydrate film growth along water/hydrate former phase boundaries- numerical heat-transfer study." *Journal of crystal growth* 290, 642-652.
- Mohammadi, A. H., and Tohidi, B. (2005). "Prediction of hydrate phase equilibria in aqueous solutions of salt and organic inhibitor using combined equation of state and activity coefficient-based model." *The canadian journal of chemical engineering*, 83, 865-871.
- Mori, Y. H., and Mochizuki, T. (2000). "Modeling of simultaneous heat and mass transfer to/from and across a hydrate film." *Gas Hydrates: Challenges for the Future*, G. D. Holder and P. R. Bishnoi, eds., 633-641.
- Moridis, G. J., and Reagan, M. T. (2007). "Gas production from oceanic class 2 hydrate accumulations." *Offshore Technology Conference, Houston, TX., Apr. 30-May 3., OTC 18866.*
- Moridis, G. J., and Sloan, E. D. (2007). "Gas production potential of disperse low-saturation hydrate accumulations in oceanic sediments." *Energy Conversion and Management*, 48(6), 1834-1849.
- Mraw, S. C., Hwang, S. C., and Kobayashi, R. (1978). "Vapor-liquid-equilibrium of CH₄-CO₂ system at low-temperatures." *Journal of Chemical and Engineering Data*, 23(2), 135-139.

- Mullin, J. W. (2001). "Crystallization, Butterworth-Heinemann." *London*.
- Nabeshima, Y., and Takai, Y. (2005). "Compressive strength and density of methane hydrate." *Proceedings of the Sixth (2005) ISOPE Ocean Mining Symposium, Changsha, Hunan, China, October 9-13, 2005*.
- Netherton, R., Piwinski, A. J., and Chan, M. (1977). "Viscosity of brine from Salton sea geothermal field, California, from 25-degrees-C to 90-degrees-C at 100 kPa." *Transactions-American Geophysical Union*, 58(12), 1248-1248.
- Nicholas, J. W., Dieker, L. E., Sloan, E. D., and Koh, C. A. (2009). "Assessing the feasibility of hydrate deposition on pipeline walls--Adhesion force measurements of clathrate hydrate particles on carbon steel." *Journal of Colloid and Interface Science*, 331(2), 322-328.
- Nixon, M. F., and Grozi, J. L. H. (2007). "Submarine slope failure due to gas hydrate dissociation: a preliminary quantification." *Canadian Geotechnical Journal*, 44, 314-325.
- Obriot, J., Ge, J., Bose, T. K., and Starnaud, J. M. (1993). "Determination of the density from simultaneous measurements of the refractive-index and the dielectric-constant of gaseous CH₄, SF₆ and CO₂." *Fluid Phase Equilibria*, 86, 315-350.
- Ohmura, R., Kashiwazaki, S., and Mori, Y. H. (2000). "Measurement of clathrate hydrate film thickness using laser interferometry." *Journal of crystal growth*, 218, 372-380.
- Ohmura, R., Shigetomi, T., and Mori, Y. H. (1999). "Formation, growth and dissociation of clathrate hydrate crystals in liquid water in contact with a hydrophobic hydrate-forming liquid." *Journal of Crystal growth*, 196, 164-173.
- Ohmura, R., Shigetomi, T., and Mori, Y. H. (2002). "Bending tests on clathrate hydrate single crystals." *Philosophical magazine A*, 82(9), 1725-1740.
- Ohmura, R., Shimada, W., Uchida, T., Moriz, Y. H., Takeyay, S., Nagaoy, J., Minagaway, H., Ebinumay, T., and Naritay, H. (2004). "Clathrate hydrate crystal growth in liquid water saturated with a hydrate-forming substance: variations in crystal morphology." *Philosophical Magazine*, 84(1), 1-16.
- Osawa, M., Tsushima, M., Mogami, H., Samjeske, G., and Yamakata, A. (2008). "Structure of Water at the Electrified Platinum-Water Interface: A Study by Surface-Enhanced Infrared Absorption Spectroscopy." *The Journal of Physical Chemistry C*, 112(11), 4248-4256.
- Østergaard, K. K., Masoudi, R., Tohidi, B., Danesh, A., and Todd, A. C. (2005). "A general correlation for predicting the suppression of hydrate dissociation temperature in the presence of thermodynamic inhibitors." *Journal of Petroleum Science and Engineering*, 48(1-2), 70-80.

- Ota, M., Abe, Y., Watanabe, M., Smith, R. L. J., and Inomata, H. (2005a). "Methane recovery from methane hydrate using pressurized CO₂." *Fluid Phase Equilibria*, 228-229.
- Ota, M., Morohashi, K., Abe, Y., Watanabe, M., Smith, R. L., and Inomata, H. (2005b). "Replacement of CH₄ in the hydrate by use of liquid CO₂." *Energy Conversion and Management*, 46(11-12), 1680-1691.
- Ota, M., Saito, T., Aida, T., Watanabe, M., Sato, Y., Smith, R. L. J., and Inomata, H. (2007). "Macro and microscopic CH₄-CO₂ replacement in CH₄ hydrate under pressurized CO₂." *Aiche Journal*, 53, 2715-2721.
- Oyama, H., Konno, Y., Masuda, Y., and Narita, H. (2009). "Dependence of depressurization-induced dissociation of methane hydrate bearing laboratory cores on heat transfer." *Energy & Fuels*, 23, 4995-5002.
- Papamichos, E., Vardoulakis, I., Tronvoll, J., and Skjærstein, A. (2001). "Volumetric sand production model and experiment." *International journal for numerical and analytical methods in geomechanics*, 25, 789-808.
- Park, Y., Kim, D. Y., Lee, J. W., Huh, D. G., Park, K. P., Lee, J., and Lee, H. (2006). "Sequestering carbon dioxide into complex structures of naturally occurring gas hydrates." *Proceedings of the National Academy of Sciences of the United States of America*, 103(34), 12690-12694.
- Petrie, E. M. (2007). "Handbook of adhesives and sealants." *Seond Edition, McGraw-Hill*.
- Petrovic, J. J. (2003). "Mechanical properties of ice and snow." *Journal of materials science*, 38, 1-6.
- Phelps, T. J., Peters, D. J., Marshall, S. L., West, O. R., Liang, L., Blencoe, J. G., Alexiades, V., Jacobs, G. K., Naney, M. T., and Heck Jr., J. L. (2001). "A new experimental facility for investigating the formation and properties of gas hydrates under simulated seafloor conditions." *Review of scientific instruments*, 72(2), 1514-1521.
- Qi, R., LaForce, T. C., and Blunt, M. J. (2009). "A three-phase four-component streamline-based simulator to study carbon dioxide storage." *Computational Geosciences*, 13(4), 493-509.
- Qin, J. F., Rosenbauer, R. J., and Duan, Z. (2008). "Experimental measurements of vapor-liquid equilibria of the H₂O+CO₂+CH₄ ternary system." *Journal of Chemical and Engineering Data*, 53(6), 1246-1249.
- Rehder, G., Kirby, S. H., Durham, W. B., Stern, L. A., Peltzer, E. T., Pinkston, J., and Brewer, P. G. (2004). "Dissolution rates of pure methane hydrate and carbon dioxide hydrate in undersaturated seawater at 1000-m depth." *Geochimica et Cosmochimica Acta*, 68, 285-292.

- Ruppel, C., and Pohlman, J. W. (2008). "Climate change and the global carbon cycle: perspectives and opportunities." in *Fire in the Ice*, edited, p. 5.
- Rutqvist, J., and Moridis, G. J. (2007). "Numerical studies of geomechanical stability of hydrate-bearing sediments." *Offshore Technological Conference, Houston, U.S.A.; 30/04–3/05 2007. OTC 18860*.
- Rutqvist, J., Moridis, G. J., Grover, T., and Collett, T. (2009). "Geomechanical response of permafrost-associated hydrate deposits to depressurization-induced gas production." *Journal of Petroleum Science and Engineering*, doi:10.1016/j.petro.2009.02.013.
- Santamarina, J. C., and Cho, G. C. (2001). "Determination of Critical State Parameters in Sandy Soils—Simple Procedure." *Geotechnical Testing Journal, GTJODJ*, Vol. 24, No. 2(2), 185–192.
- Santamarina, J. C., and Jang, J. (2009). "Gas production from hydrate bearing sediments: geomechanical implications." *NETL methane hydrate newsletter: Fire in the ice*, 9(4), 18-22.
- Santamarina, J. C., Klein, K. A., and Fam, M. A. (2001). "Soils and Waves, J. Wiley & Sons, New York, 488 pp."
- Santamarina, J. C., and Ruppel, C. (2008). "The impact of hydrate saturation on the mechanical, electrical, and thermal properties of hydrate-bearing sand, silts, and clay." *Proc. 6th Int. Conf. Gas Hydrates, Vancouver, Canada, 6-10 July, 2008, 12 pp*.
- Seddon, K. R., and Zaworotko, M. (1999). *Crystal engineering: The design and Application of functional solids*, Kluwer Academic Publishers.
- Seo, Y. T., and Lee, H. (2001). "Multiple-phase hydrate equilibria of the ternary carbon dioxide, methane, and water mixtures." *Journal of Physical Chemistry B*, 105(41), 10084-10090.
- Servio, P., and Englezos, P. (2003). "Morphology of methane and carbon dioxide hydrates formed from water droplets." *Aiche Journal*, 49(1), 269-276.
- Shin, H., and Santamarina, J. C. (2010). "Hydraulic fractures in unconsolidated sediments." *Earth And Planetary Science Letters (under review)*.
- Sloan, E. D. (2003). "Fundamental Principles and Applications of Natural Gas Hydrates." *Nature*, 426(6964), 353-359.
- Sloan, E. D., and Koh, C. H. (2008). "Clathrate hydrates of Natural gases." *Taylor & Francis Group, LLC, Third edition*.
- Span, R., and Wagner, W. (1996). "A new equation of state for carbon dioxide covering

- the fluid region from the triple-point temperature to 1100 K at pressures up to 800 MPa." *Journal of Physical and Chemical Reference Data*, 25(6), 1509-1596.
- Spangenberg, E., and Kulenkampff, J. (2005). "Physical properties of gas hydrate bearing sediments." *Fifth International Conference on Gas Hydrates, Trondheim, Norway*.
- Spycher, N., Pruess, K., and Ennis-King, J. (2003). "CO₂-H₂O mixtures in the geological sequestration of CO₂. I. Assessment and calculation of mutual solubilities from 12 to 100 degrees C and up to 600 bar." *Geochimica Et Cosmochimica Acta*, 67(16), 3015-3031.
- Stern, L. A., Kirby, S. H., and Durham, W. B. (1996). "Peculiarities of methane clathrate hydrate formation and solid-state deformation, including possible superheating of water ice." *Science*, 273(5283), 1843-1848.
- Stern, L. A., Kirby, S. H., and Durham, W. B. (1998). "Polycrystalline Methane Hydrate: Synthesis from Superheated Ice, and Low-Temperature Mechanical Properties." *Energy & Fuels*, 12(2), 201-211.
- Stern, L. A., Kirby, S. H., Durham, W. B., Circone, S., and Waite, W. F. (2000). "Natural Gas Hydrate in Oceanic and Permafrost Environments." *edited by M. D. Max (Dordrecht: Kluwer), chapter 25, 323-348*.
- Stevens, C. J., Howard, J. J., Baldwin, B. A., Ersland, G., Husebo, J., and Graue, A. (2008). "Experimental hydrate formation and gas production scenarios based on CO₂ sequestration." *Proceedings of the 6th International Conference on Gas Hydrates, Vancouver, British Columbia, CANADA*.
- Subramanian, S., and Sloan, E. D. (2002). "Solubility effects on growth and dissolution of methane hydrate needles." *Proceedings of the Fourth International Conference on Gas Hydrates, Yokohama, pp. 856-861*.
- Sugaya, M., and Mori, Y. H. (1996). "Behavior of clathrate hydrate formation at the boundary of liquid water and a fluorocarbon in liquid or vapor state." *Chemical engineering science*, 51(13), 3505-3517.
- Sultan, N., Cochonat, P., Cayocca, F., Bourillet, J.-F., and Colliat, J.-L. (2004a). "Analysis of submarine slumping in the Gabon continental slope." *American Association of Petroleum Geologists Bulletin*, 88(6), 781-799.
- Sultan, N., Foucher, J. P., Cochonat, P., Tonnerre, T., Bourillet, J. F., Ondreas, H., Cauquil, E., and Grauls, D. (2004b). "Dynamics of gas hydrates: case of the Congo continental slope." *Marine Geology*, 206, 1-18.
- Sun, R., and Duan, Z. H. (2005). "Prediction of CH₄ and CO₂ hydrate phase equilibrium and cage occupancy from ab initio intermolecular potentials." *Geochimica Et Cosmochimica Acta*, 69(18), 4411-4424.

- Sun, R., and Duan, Z. H. (2007). "An accurate model to predict the thermodynamic stability of methane hydrate and methane solubility in marine environments." *Chemical Geology*, 244(1-2), 248-262.
- Svandal, A., Kvamme, B., Grønåsy, L., Pusztai, T., Buanes, T., and Hove, J. (2006). "The phase-field theory applied to CO₂ and CH₄ hydrate." *Journal of Crystal Growth*, 287(2), 486-490.
- Szozzkiewicz, R., Bhushan, B., Huey, B. D., Kulik, A. J., and Gremaud, G. (2005). "Correlations between adhesion hysteresis and friction at molecular scales." *The Journal of Chemical Physics*, 122(14), 144708-6.
- Tabe, Y., Hirai, S., and Okazaki, K. (2000). "Massive CO₂ clathrate hydrate growth at a high-polar-energy surface." *Journal of Crystal Growth*, 220, 180-184.
- Tanaka, Y., Yamachi, N., Matsumoto, S., Kaneko, S., Okabe, S., and Shibuya, M. (2008). "Thermodynamic and transport properties of CO₂, CO₂-O₂, and CO₂-H₂ mixtures at temperatures of 300 to 30,000 K and pressures of 0.1 to 10 MPa." *Electrical Engineering in Japan*, 163(4), 18-29.
- Tang, L. G., Xiao, R., Huang, C., Feng, Z. P., and Fan, S. S. (2005). "Experimental investigation of production behavior of gas hydrate under thermal stimulation in unconsolidated sediment." *Energy & Fuels*, 19, 2402-2407.
- Taylor, C. J., Dieker, L. E., Miller, K. T., Koh, C. A., and D., S. E. (2007a). "Micromechanical adhesion force measurements between tetrahydrofuran hydrate particles." *Journal of colloid and surface science*, 306, 255-261.
- Taylor, C. J., Miller, K. T., Koh, C. A., and Sloan, E. D. (2007b). "Macroscopic investigation of hydrate film growth at the hydrocarbon/water interface." *Chemical Engineering Science* 62, 6524-6533.
- Thomas, W. J., and Adams, M. J. (1965). "Measurement of the diffusion coefficient of carbon dioxide and nitrous oxide in water and aqueous solutions of glycerol." *Transactions of the Faraday Society*, 61, 668-673.
- Trusler, J. P. M., and Zarari, M. (1992). "The speed of sound and derived thermodynamic properties of methane at temperatures between 275-K and 375-K and pressures up to 10-MPa." *Journal of Chemical Thermodynamics*, 24(9), 973-991.
- Tsionsky, V., Alengoz, E., Daikhin, L., Kaverin, A., Zagidulin, D., and Gileadi, E. (2005). "The liquid-like layer between metal and frozen aqueous electrolytes: An electrochemical approach employing the quartz crystal microbalance." *Electrochimica Acta*, Vol 50, pp. 4212-4221.
- Uchida, T., Ebinuma, T., Kawabata, J., and Narita, H. (1999). "Microscopic observations of formation processes of clathrate-hydrate films at an interface between water and carbon dioxide." *Journal of Crystal Growth* 204, 348-356.

- Uchida, T., Takeya, S., Kamata, Y., Ikeda, I. Y., Nagao, J., Ebinuma, T., Narita, H., Zatsepina, O., and Buffett, B. A. (2002). "Spectroscopic observations and thermodynamic calculations on clathrate hydrates of mixed gas containing methane and ethane: Determination of structure, composition and cage occupancy." *Journal of Physical Chemistry B*, 106(48), 12426-12431.
- Ullerich, J. W., Selim, M. S., and Sloan, E. D. (1987). "Theory and measurement of hydrate dissociation." *AIChE Journal*, 33(5), 747-752.
- Valdes, J. R., and Santamarina, J. C. (2008). "Clogging: bridge formation and vibration-based destabilization." *Canadian Geotechnical Journal*, 45, 177-184.
- Vesovic, V., Wakeham, W. A., Olchoway, G. A., Sengers, J. V., Watson, J. T. R., and Millat, J. (1990). "The transport-properties of carbon-dioxide." *Journal of Physical and Chemical Reference Data*, 19(3), 763-808.
- Waite, W. F., deMartin, B. J., Kirby, S. H., Pinkston, J., and Ruppel, C. D. (2002). "Thermal conductivity measurements in porous mixtures of methane hydrate and quartz sand." *Geophysical Research Letters*, 9(24).
- Waite, W. F., Santamarina, J. C., Cortes, D. D., Dugan, B., Espinoza, D. N., Germaine, J., Jang, J., Jung, J. W., Kneafsey, T. J., Shin, H., Soga, K., Winters, W. J., and Yun, T.-S. (2009). "Physical properties of hydrate-bearing sediment." *Reviews of geophysics*, 47, RG4003.
- Waite, W. F., Stern, L. A., Kirby, S. H., Winters, W. J., and Mason, D. H. (2007). "Simultaneous determination of thermal conductivity, thermal diffusivity and specific heat in sl methane hydrate." *Geophysical Journal International*, 169(2), 767-774.
- Waite, W. F., Winters, W. J., and Mason, D. H. (2004). "Methane hydrate formation in partially water-saturated Ottawa sand." *American Mineralogist*, 89(8-9), 1202-1207.
- Walsh, M. R., Koh, C. A., Sloan, E. D., Sum, A. K., and Wu, D. T. (2009). "Microsecond simulation of spontaneous methane hydrate nucleation and growth." *Science*, 326(5956), 1095-1098.
- Wang, Y.-H., and Leung, S.-C. (2008). "A particulate-scale investigation of cemented sand behavior." *Canadian Geotechnical Journal*, Vol. 45.
- West, O., Tsouris, C., Liang, L., Lee, S., and McCallum, S. (2003). "Negatively Buoyant CO₂-Hydrate Composite for Ocean Carbon Sequestration." *AIChE Journal*, 49, 283-285
- Wilder, J. W., Moridis, G. J., Wilson, S. J., Kurihara, M., White, M. D., Masuda, Y., Anderson, B. J., Collett, T. S., Hunter, R. B., Narita, H., Pooladi-Darvish, M., Rose, K., and Boswell, R. (2008). "international effort to compare gas hydrate

- reservoir simulators." *6th International conference on gas hydrate, Vancouver, Canada, July 6-10.*
- Witherspoon, P. A. a. B., L. (1969). "Correlation of diffusion coefficients for Aaraffin, Aromatic, and Cycloparaffin Hydrocarbons in Water." *Industrial&Engineering Chemistry Fundamentals*, 8(3), 589-591.
- Yang, S. O., Kleehammer, D. M., Huo, Z., Sloan, E. D., and Miller, K. T. (2004). "Temperature dependence of particle-particle adherence forces in ice and clathrate hydrates." *Journal of Colloid and Interface Science*, 277(2), 335-341.
- Yoon, J.-H., Kawamura, T., Yamamoto, Y., and Komai, T. (2004). "Transformation of Methane Hydrate to Carbon Dioxide Hydrate: In Situ Raman Spectroscopic Observations." *The Journal of Physical Chemistry A*, 108(23), 5057-5059.
- Yoon, J. H., Yamamoto, Y., Komai, T., Haneda, H., and Kawamura, T. (2003). "Rigorous approach to the prediction of the heat of dissociation of gas hydrates." *Industrial & Engineering Chemistry Research*, 42(5), 1111-1114.
- Yun, T. S., Santamarina, J. C., and Ruppel, C. (2007). "Mechanical properties of sand, silt, and clay containing tetrahydrofuran hydrate." *J. Geophys. Res.*, 112.
- Zatsepina, O. Y., and Buffet, B. A. (2001). "Experimental study of stability of CO2 hydrate in a porous medium." *Fluid Phase Equilibria*, 200(2), 263-275.
- Zhang, Y., and Xu, Z. (2003). "Kinetics of convective crystal dissolution and melting with applications to methane hydrate dissolution and dissociation in seawater." *Earth and Planetary Science Letters*, 213, 133-148.
- Zhong, D. L., Liu, D. P., Wu, Z. M., and Zhang, L. (2008). "Natural gas hydrate formation and growth on suspended water droplet." *Proceedings of the 6th International Conference on Gas Hydrates (ICGH 2008), Vancouver, British Columbia, CANADA, July 6-10, 2008.*
- Zhong, Y., and Rogers, R. E. (2000). "Surfactant effects on gas hydrate formation." *Chemical Engineering Science*, 55(19), 4175-4187.
- Zhou, X. T., Fan, S. S., Liang, D. Q., and Du, J. W. (2008a). "Determination of appropriate condition on replacing methane from hydrate with carbon dioxide." *Energy Conversion and Management*, 49(8), 2124-2129.
- Zhou, X. T., Fan, S. S., Liang, D. Q., and Du, J. W. (2008b). "Replacement of methane from quartz sand-bearing hydrate with carbon dioxide-in-water emulsion." *Energy & Fuels*, 22(3), 1759-1764.